SETCOR
Conferences & Events

Nanotech Tunisia 2015
International Conference
Proceeding

http://www.setcor.org/conferences/Nanotech-Tunisia-2015

Analytical Efficient Model of the Tunneling Current in Ambipolar Schottky Barrier Carbon nanotube Field Effect Transistor

M. Najari[1,2], W. Ben Ayed[1], H. Samet[1]
1 University of Sfax, Laboratory of Electronics and Information Technology LETI, Sfax, Tunisia
2 University of Gabes, Faculty of Sciences of Gabes, Department of Physics, Gabes, Tunisia

Abstract: Carbon nanotubes are becoming more and more popular thanks to their mechanical and electrical properties. Recently, the conventional carbon nanotube transistor (C- CNTFETs) modeling is widely studied. However, the literature describing the model of Schottky barrier carbon nanotube transistor (SB-CNTFET) is limited. Since no analytical solution is carried out for the tunneling current in SB-CNTFET with ambipolar character, a new approach is proposed to find an analytical approximation of the tunneling current. The ambipolar behavior is treated. The proposed compact analytical model for SB-CNTFET can be implemented with a hardware description language (HDL). The simulation results, obtained using this model, are in close agreement with numerical calculation results.

Keywords: SB-CNTFET, ambipolar behavior, compact model

1. INTRODUCTION

Thanks to their excellent electrical, optical and mechanical properties, a lot of research studies have focused on the carbon nanotubes (CNTs) as candidates to overcome the present challenges related to the physical technology limits of silicon MOSFET (Appenzeller *et al*., 2002).

Semiconducting carbon nanotube can be used as the channel in Carbon Nanotube Field Effect Transistor (CNTFET). The Schottky barrier source and drain contact between metal and CNT are always present in the fabricated devices, the tunneling current is the dominant mechanism across the contacts. If we neglect the SB effect, this overestimates the drain current. Moreover, the ambipolar behavior of Schottky barrier CNTFETs limits the performance of these devices in both 'On' and 'Off' regimes (Pourfath *et al*., 2004) and consequently the ION/IOFF ratio is limited.

These limitations result from the decrease of the On current caused by barrier height between metal and CNT. However, the increase of the off current is due to the ambipolar characteristics resulting from the parasitic hole current injection at the drain contact through the valence band for n-type devices, or, from the parasitic electron current at the drain contact through the conduction band for p-type devices.

Two types of current tunneling or thermionic current can be present in SB-CNTFET. Carriers with energies above the Schottky barrier height reach the channel by thermionic emission. On the contrary, carriers with energies below the Schottky barrier height reach the channel by tunneling emission featuring a transmission function

Some research works have been carried out to obtain a numerical (Jiménez *et al*., 2007) (Guo *et al*., 2004), and analytical model in order to calculate the tunneling current in SB-CNTFET (Najari *et al*., 2009 2010).

The main issue of this paper is to provide an accurate analytical model for the tunneling current of the n- type SB-CNTFET with ambipolar characteristics. The proposed model will be compared with numerical simulation results. A close agreement is obtained.

This paper is organized as follows: Section 2 describes the physical equations of the tunneling current through the Schottky barrier CNTFET and poses the mathematical problems. Section 3 gives an analytical solution for the tunneling electron current in SB-CNTFET. The obtained solution is validated by a comparison with numerical calculation. Section 4 presents an analytical model for the tunneling holes current in SB-CNTFET. This model is also validated by a comparison with numerical results. Section 5 presents the total tunneling current in SB-CNTFET; the agreement between the numerical calculation and the proposed model is satisfactory.

2. TUNNELING CURRENT IN THE SB-CNTFET

Assuming the ballistic transport, the ambipolar tunneling drain current is given by Landauder-Büttiker formula. It is composed of both carriers' electrons and holes, the electrons are transported from source to drain contact through conduction band. Whereas, the holes are transported from drain to source contact through the valence band as shown in figure 1.

$$I_{DS} = \frac{2e}{h} M \int_0^{\infty} [f_S(E) - (1 - f_D(E))] T_T(E) dE \quad (1)$$

Where f_S, f_D are Fermi Dirac distributions at the source and drain contacts respectively, and T_T is the total transmission function.

$$f_S = \frac{1}{1+\exp\left(\frac{E-qV_{CNT}}{K_BT}\right)} \quad (2)$$

$$f_D = \frac{1}{1+\exp\left(\frac{E-q(V_{CNT}+V_{DS})}{K_BT}\right)} \quad (3)$$

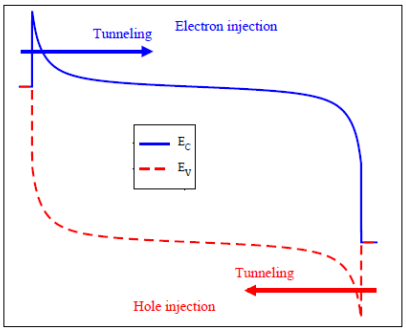

Figure.1 Band energy profile for ambipolar SB-CNTFET

There are two interfaces Schottky barrier contacts source/CNT interface and CNT /drain interface. The total transmission function $T_T(E)$ is expressed using the transmission function of source $T_S(E)$ and drain $T_D(E)$. By using the Wentzel- Kramers- Brillouin (WKB) approximation (Messiah, 1991) and assuming a triangular potential profile: $T_S(E)$ and $T_D(E)$ can be depicted as follows:

$$T_S(E) = \exp\left(-A(\Phi_{SB} - E - qV_S)^{3/2}\right) \quad (4)$$

$$T_D(E) = \exp\left(-A(\Phi_{SB} - E - qV_{DS})^{\frac{3}{2}}\right) \quad (5)$$

Where

$$A = 4\frac{\sqrt{2m^*}}{3hqE_{elec}} \quad (6)$$

$m^*$is the carrier effective mass,$\Phi_{SB}$is the SB height, $E_{elec}$is the electrical field$E_{elec} = \frac{V_{cnt}}{\lambda}$,$\lambda$ is the is the screening length, $\lambda = 3\text{nm}$ and h is the Planck constant. Like in Fabry-Perot cavity, the total transmission function $T_T(E)$ over the whole structure is predicted to be (Datta, 1997):

$$T_T = \frac{T_S(E).T_D(E)}{T_S(E)+T_D(E)-T_S(E).T_D(E)} \quad (7)$$

The total tunneling current given in equation (8) cannot be directly calculated since it has no analytical solution. So, it cannot be implemented in compact model.

3. Analytical Solution of Electrons Contribution

To overcome the complexity of implementing the tunneling current in equation (8) in compact model, an approximation method has to be used to extract an analytical solution.

Partial solutions have to be considered depending on the relative variation of the Fermi-Dirac distribution and the total transmission function.

Hence, the electrons and holes contribution are calculated by means of partial solutions over a large variation of the gate potential and for low, middle and high carrier energies. Figure 2 and figure 3 shows a comparison between these analytical solutions and the numerical calculation for the electrons current and the holes current respectively. A very good agreement is shown in both cases. The mean absolute percentage (MAP) error is equal to 0.05% and 3.46% for the electrons current and the holes current respectively.

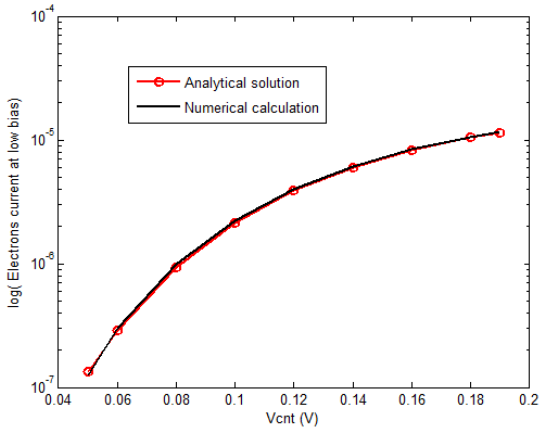

(a)

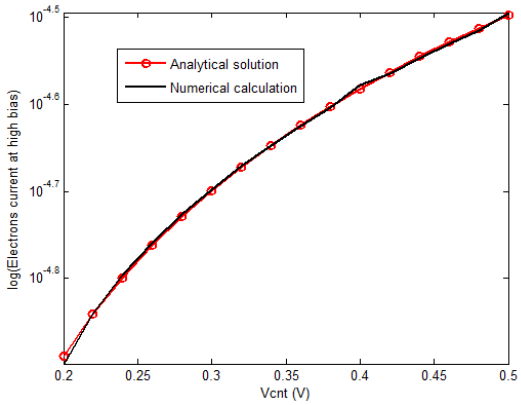

(b)

Figure 2. Comparison between numerical (solid line with circle) and analytical solutions (solid black line) for electrons contribution at low (a) and high (b) gate biases.

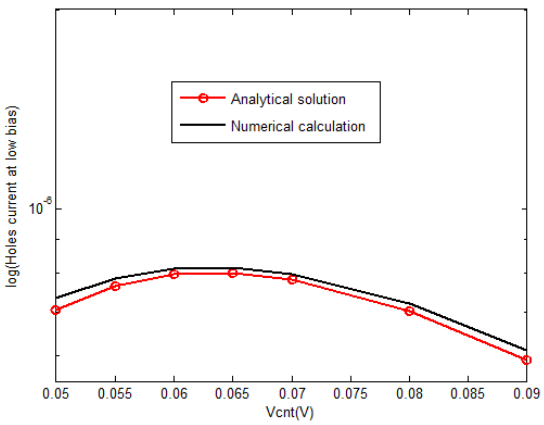

(a)

$$I_{DS} = \frac{4e}{h}\sum_{p=1}^{nb}\left[\int_{\Phi_{SB-V_{cnt-sbbd}}}^{\Phi_{SB-qV_D}} T_T(E).f_S(E)\ dE - \int_{\Phi_{SB-V_{cnt-sbbd}}}^{\Phi_{SB-qV_D}} T_T(E).(1-f_D(E))dE\right] \quad (8)$$

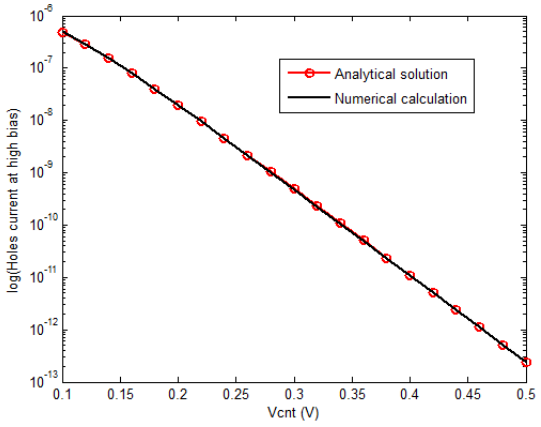

(b)

Figure 2. Comparison between numerical (solid line with circle) and analytical solutions (solid black line) for holes contribution at low (a) and high (b) gate biases.

4. TOTAL ANALYTICAL SOLUTION

Two smoothing functions F_{SMO_e} and F_{SMO_h} are used to obtain a complete analytical solution. These functions are introduced here to ensure both the accuracy and the numerical convergence of the model, which is a very common technique in compact modeling.

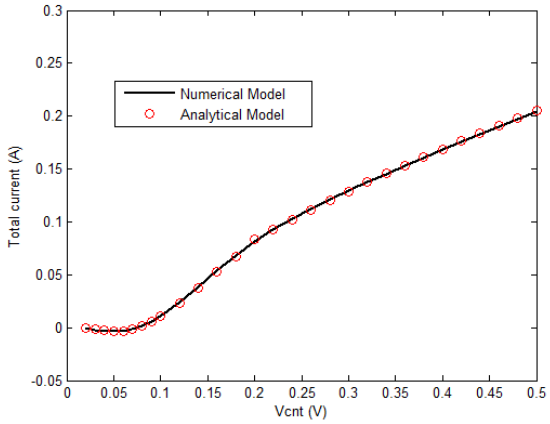

Figure 3. Comparison of numerical and analytical solutions for the total tunneling current in linear scale. The analytical solution (solid line with circle) agrees with the numerically calculated total tunneling current (solid line).

$$I_e = I_{L\_e} * f_{SMO\_e} + I_{H\_e}(1 - f_{SMO\_e}) \quad (9)$$

$$I_h = I_{L\_h} * f_{SMO\_h} + I_{H\_h}(1 - f_{SMO\_h}) \quad (10)$$

$$I_{analytical} = I_e - I_h \quad (11)$$

5. CONCLUSION

In this paper, an analytical model of tunneling current for ambipolar Schottky barrier CNTFET has been developed based on the approximation of the transmission function and the Fermi Dirac distribution of the electrons and holes in different gate bias.

To ensure the proposed analytical model accuracy, a comparison with the numerical calculation has been performed. A close agreement is obtained. Our proposed model presents the error in the total tunneling current less than 0.25%.

REFERENCES

J.Appenzeller and al. "Carbon Nanotube Electronics" *IEEE Transaction On Nanotechnology*, Vol. 1, No. 4, December 2002

M. Pourfath, E. Ungersboeck, A. Gehring, B.H. Cheongy, W. Park, H. Kosina, and S. Selberherr " Improving the Ambipolar Behavior of Schottky Barrier Carbon Nanotube Field Effect Transistors. "Solid-State Device Research conference, 2004.

D. Jiménez, X. Cartoixà, E. Miranda, J. Suñé, F. A. Chaves and S. Roche "A simple drain current model for Schottky-barrier carbon nanotube field effect transistors" IOP science Nanotechnology, Issue. 41, 2007

J. Guo, S. Datta and M. Lundstrom "A numerical study of scaling issues for Schottky-barrier carbon nanotube transistors" Electron Devices, IEEE Transactions on Vol. 51 , Issue. 2, 2004

M. Najari, S. Frégonèse, C. Maneux, H. Mnif, T. Zimmer and N. Masmoudi "Efficient physics-based compact model for the Schottky barrier carbon nanotube FET" solid state physics,Vol.7, Issue. 11–12, 2010

M. Najari, S. Frégonèse, C. Maneux, T. Zimmer, H. Mnif, and N. Masmoudi "Analytical modeling of the tunneling current in Schottky barrier carbon nanotube field effect transistor using the Verilog-A language" Systems, Signals and Devices, 2009.

A. Messiah, Quantenmechanik 1 DeGruyter 1991

S. Datta **"**Electronic Transport in Mesoscopic systems**"** Cambridge University Press-1997

3-D Design, Electro-Thermal Simulations of Metal Oxide Gas Sensor Based on a High Temperature and Low Power Consumption Micro- Heater Structure and Geometrical Optimization of Spiral Platinum Micro-heaters using COMSOL

Amer Abdeslam Aimer* [1], Dr. Fouad Kerrour [1], Pr. Khalifa Aguir [2]

[1] Modeling of Renewable Energy Devices and Nanoscale laboratory,
University. of Constantine 1,
University Mentouri brothers Constantine, 25000 Constantine,ALgéria,

[2] Faculty of Science St-Jérôme, case142,
Aix Marseille University, CNRS, IM2NP UMR 7334,
Av. E.N. Neimen 13397 Marseille, France,

E-mail *[1]: amer20ans @hotmail.fr
E-mail [1]: f_kerrour@yahoo.fr
E-mail [2]: khalifa.aguir@im2np.fr
*Corresponding author

Abstract. Metal oxide gas sensors have many qualities that make this kind of sensor one of the most studied in laboratories and used in companies. They have a simple structure and their operating principle is based on the fact that their electrical conductivity (or resistance) can be modulated by the presence or absence of some chemical species that comes in contact with the device. In this paper we have presented the MEMS micro-heaters for gas sensing applications. A thermal electric finite element method (FEM) analysis was used to investigate the thermal properties of individual electrically driven platinum micro-heaters. The geometric optimization for the micro-heater was performed by simulating a wide range of possible geometries using COMSOL 4.3. The simulated results of micro-heaters having an improved temperature distribution over the sensing area of gas sensor are demonstrated. These micro-heaters are designed to ensure low power consumption, low thermal mass and better temperature uniformity. For this purpose, the Joule Heating physics interface has been used and a stationary study has been executed in order to: check the temperature distribution on the surface. Three different patterns of micro-heaters which are spiral, meander and ring are simulated; it was found that the spiral shape is the most suitable, in temperature uniformity and power consumption. The spiral form was used after introducing the SnO2 tin oxide as a sensitive layer and the tungsten oxide WO3 thereafter and results are compared, and observe the influence of a sensitive layer with different thickness on the maximum temperature for different power consumptions.

1. Introduction

Metal oxide gas sensors have many qualities, allowing their use in many areas. Their operation depends on several parameters, including the temperature of the heating element (resistance), which plays a crucial role, especially in terms of their stability and their sensitivity.

In this work, we simulated several sharps of micro-heater (spiral, meander and ring) under COMSOL multiphysics software.

In order to optimize sensor performances, simulation of two devices provided with a micro-heater spiral shape, with different sensitive layers (WO3 and SnO2) has been performed.

2. Mathematical modeling of Micro-heater

The Joule Heating Model node in COMSOL uses the following version of the heat equation as the mathematical model for heat transfer in solids:

$$Q = \rho C_p \frac{dT}{dt} - \Delta(k.\Delta T) \quad (1)$$

With the following material properties:

Q: Heat source (W/m3),
Cp: Heat capacity (J/kg .K),
T: Temperature (K),
ρ: Density (kg/m3),
K: Thermal conductivity (W/m. K),

In Joule heating, the temperature increases due to the resistive heating from the electric current. The electric potential V is the variable solution in the Conductive Media DC application mode. The generated resistive heat Q is:

$$Q = \rho|J^2| \quad (2)$$

Where σ Electric conductivity and *J:* is the current density, which is also the reciprocal of the temperature-dependent electric conductivity $\sigma = \sigma(T)$.

Combining these facts gives the fully coupled relation.

$$Q = \frac{1}{\sigma}|J^2| = \frac{1}{\sigma}|\sigma E|^2 = \sigma|\Delta V|^2 \quad (3)$$

Over a range of temperatures the electric conductivity σ is a function of temperature T, According to:

$$\sigma = \frac{\sigma_0}{1+\alpha(T-T_0)} \quad (4)$$

Where σ_0: the conductivity at the reference temperature T_0, α is the temperature coefficient of resistivity, which describes how the resistivity varies with temperature. Also the power consumption is described as:

$$P = \frac{V^2}{R} \quad (5)$$

Where V is voltage and R stands for resistance of heating electrode. Here power consumption is directly proportional to the applied voltage and inversely proportional to the resistance of the material.

The equations have been solved numerically under and mixed boundary conditions (Dirichlet and Neumann), using the Finite Element Method (FEM) in COMSOL 4.3. Fixed temperature and potentials are assumed at ends of the heater. Several materials properties are required to solve the mathematical equations mentioned above. In Table1 material properties of platinum are shown.

Table 1 Material properties of Platinum

Parameter	Value
Heat capacity at constant pressure (C)	133[(J/ (Kg*K)]
Young's modulus (E)	168 e9 [Pa]
Thermal expansion coefficient (α)	8.80 e-6[1/K]
Poisson's ratio (μ)	0.38
Density (ρ)	21450[kg/m^3]
Thermal conductivity (k)	71.6 [W/ (m*K)]
Electric conductivity(σ)	8.9 e6[S/m]

3. Simulation and analysis of Micro- heaters

The power consumption must be as low as possible. A compromise should be found between these two parameters. That's why a metal oxide gas sensor, based on a micro-heater structure on a membrane able to work until 600 °C (with a power consumption equal to 60 mW at this temperature), has been developed. The technological process is the following: the bi-layer SiO2/SiNx membrane is grown on a silicon substrate; the heater and sensible electrodes metallization in platinum are deposited by evaporation; a SiO2 passivation layer is grown; the contact open is realized by a wet etching; the membrane is released by a dry etching; the sensitive layer is deposited by inkjet. The electro-thermal simulation of this structure with COMSOL 4.3 has been realized. For this purpose, the Joule Heating physics interface has been used and a stationary study has been executed in order to: check the temperature distribution on the surface (Figure 1).

Figure 1 Micro-hotplate 3D design (Spiral form) with COMSOL4.3

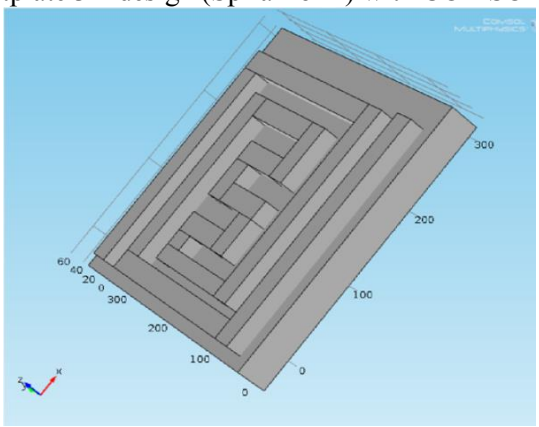

Figure 2 3D temperature distribution in the micro-hotplate for V =2V

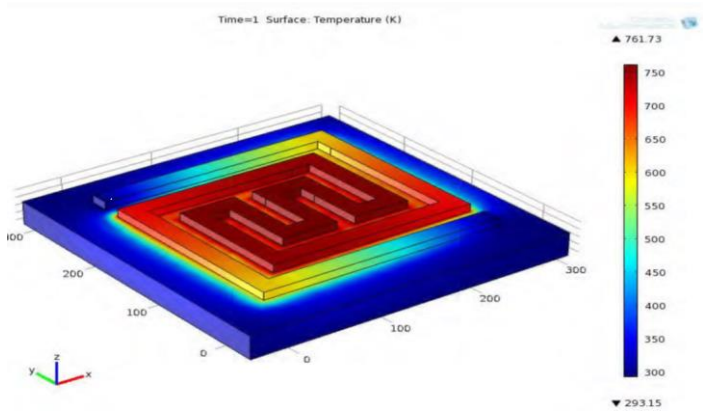

Figure 3 Temperature distributions in the micro-hotplate for several shape (a-Spiral, b-ring, and c-meander)

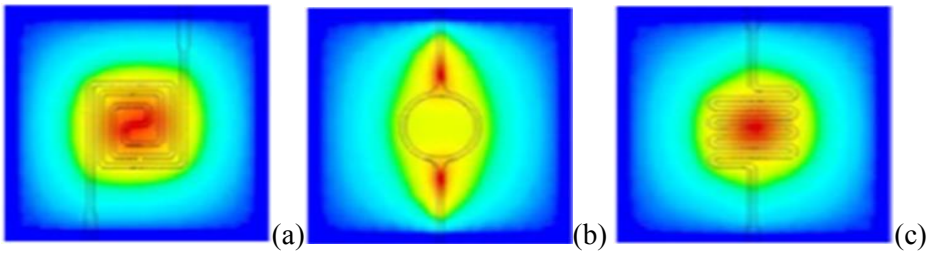

Figure 4 Superficial temperature distributions vs. Supply voltage for sevral shapes microhotplates

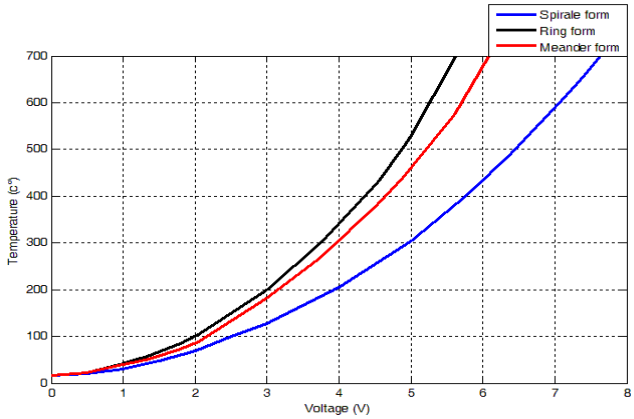

Figure 5 Superficial temperature distributions vs. x axis for sevral shapes micro-hotplates

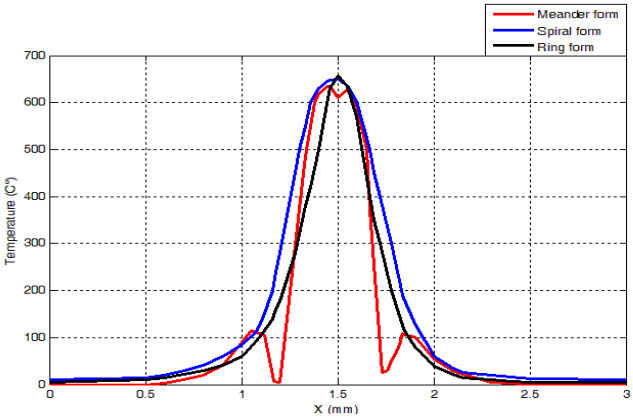

Figure 6 Temperature variation vs. Power consumption for sevral shapes micro-hotplates

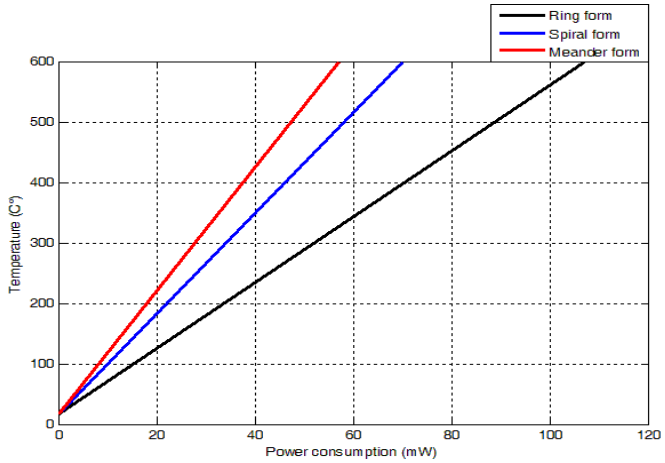

Figure 7 3DSensor design

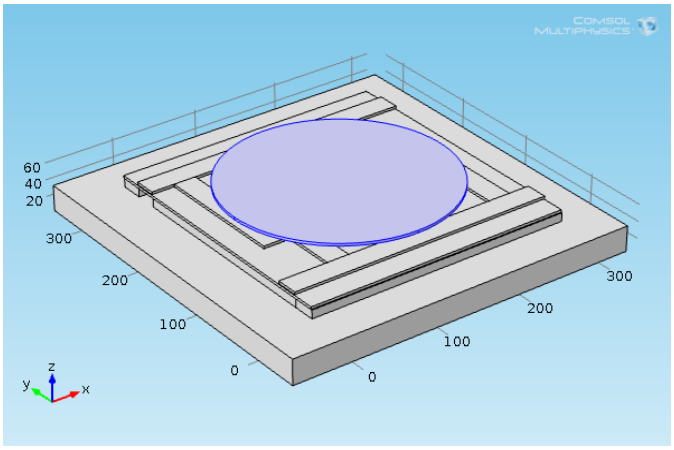

Figure 8 3D temperature distribution in the sensitive layer for V = 2 V

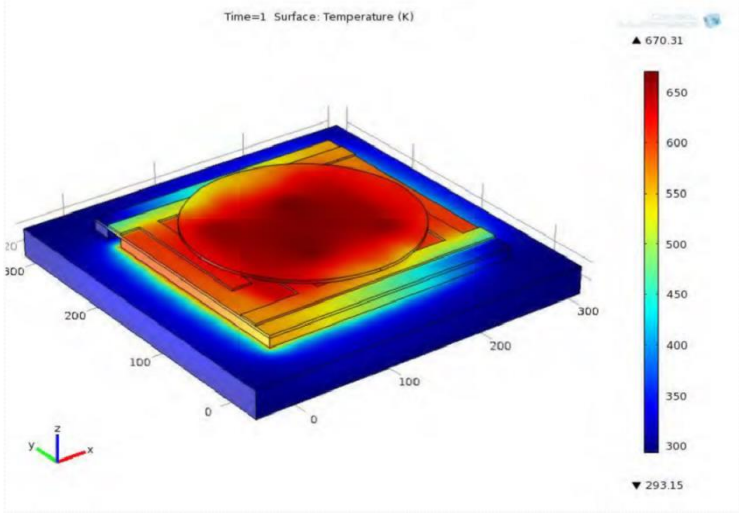

In the above figure we represent the distribution of heat on the simulated model (using SnO2 as sensitive layer); the temperature reaches 660 ° C on the sensitive layer.
Three different patterns of micro-heaters which are spiral, meander and ring are simulated; it was found that the spiral shape is the most suitable, in temperature uniformity and power consumption (Figures 4-5-6).

The spiral form was used after introducing the SnO2 tin oxide as a sensitive layer, and the tungsten oxide WO3 thereafter and results are compared (Figure 9).

Figure 9 Comparing the thermal profile of SnO2 and WO3.

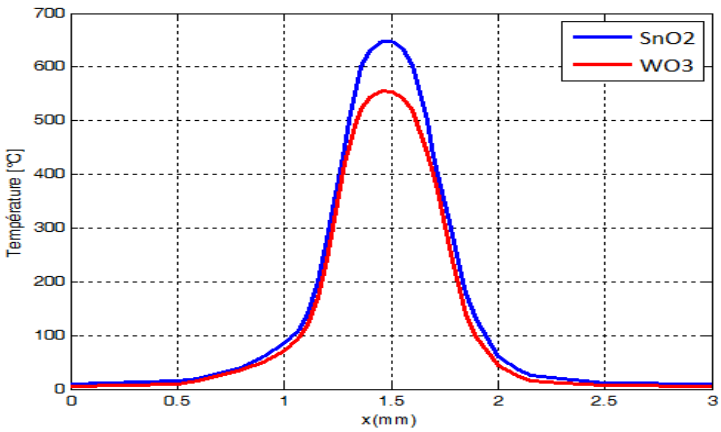

The figure above shows a comparison between the use of SnO2 and WO3 as sensitive layer, we find that the temperature distribution is more interesting (640°C) in the case of the SnO2 when we reached 560 ° C when using WO3.
We observe also the influence of a sensitive layer with different thickness on the maximum temperature for different power consumptions (Figure 11).

Figure 10 Voltage in function of temperature of SnO2 and WO3.

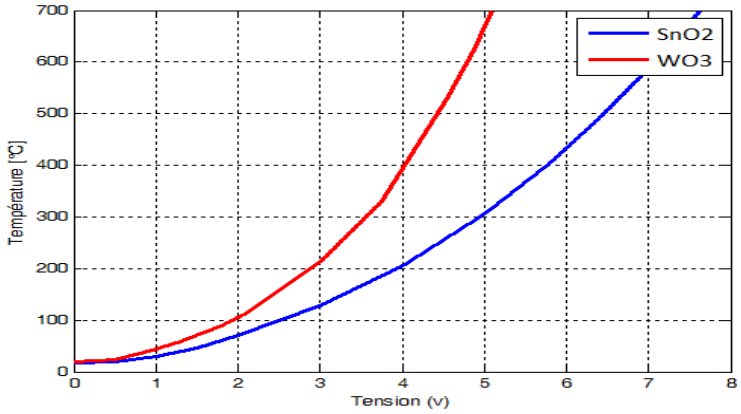

In this figure it is observed that the temperature increases in a nonlinear manner as a function of the voltage applied to all cases.
According to the literature that the WO3 operating temperature is between 250 and 400C °, whereas the SnO2 is between 500C ° 350et .So for WO3 tension will be between 3 and 4 V. While for the SnO2 tension will be between 5 and 6V.

Figure 11 Power consumption in function of the temperature of SnO2 and WO3.

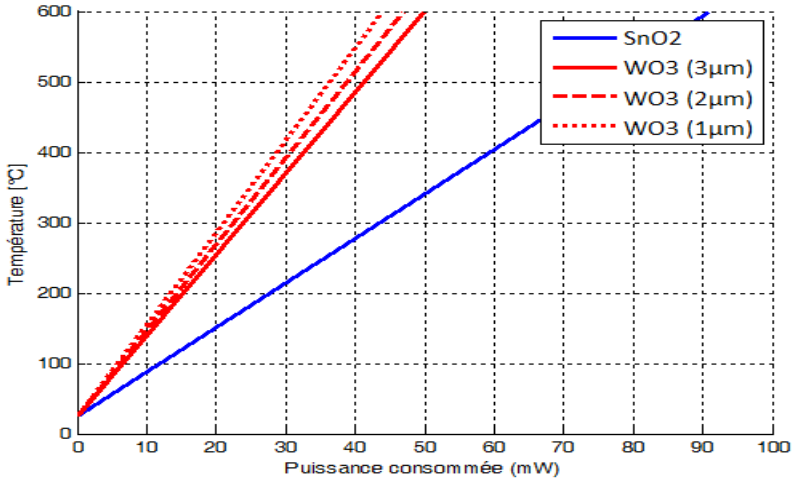

In the figure above **we** see that for WO3, the power consumption of operation is between 17 and 30 mW, while for the SnO2 power consumption is between 40 and 65mW
Reducing the thickness of the sensitive layer leads to a minimization of the power consumption.

4. Conclusion

In this work, a comparative study of the different forms of micro-heater has been developed. The results show that the spiral shape leads to excellent temperature uniformity and low power consumption.

The simulation of the sensor with different sensitive layers (SnO_2 and WO_3) was performed; it shows that the use of WO_3 as the material of the sensitive layer allows the production of low power consumption compared to that obtained for the material SnO_2.

In order to determine the influence of the sensitive layer thickness, a study based on thickness effect has been performed. The results show that the power consumption is inversely proportional to the sensitive layer thickness. These results are similar to those obtained in the literature.

References

[1] J. Courbat & al, (2012) ‘ Drop-coated metal-oxide gas sensor on polyimide foil with reduced power consumption for wireless applications’, Sensors and Actuators B, 161, 862– 868.

[2] Monika, Dr. Arti Arora, (2013) ‘Design and Simulation of MEMS based Microhotplate as Gas Sensor’, (IJARCET) Volume 2 Issue 8.

[3] F. Bíró, C. Dücső, (2013) ’Optimisation of Low Dissipation Micro-hotplates – Thermo-mechanical Design and Characterisation’, IEEE, Therminic, September Berlin, Germany.

[4] N. Dufour, K.Aguir, P. Menini, (2014) ‘Increasing the Sensitivity and Selectivity of Metal Oxide Gas Sensors by Controlling the Sensitive Layer Polarization’, IEEE, Toulouse France.

[5] L.Sujatha, V.S.Selvakumar, S.Aravind, R.Padamapriya, B.Preethi, (2012) ‘Design and Analysis of Micro-Heaters using COMSOL Multiphysics for MEMS Based Gas Sensor, Proceedings COMSOL conference.

[6] M. Camara, F. Molina-Lopez, (2013) ’PRINTED MICRO-HOTPLATES ON FLEXIBLE SUBSTRATES FOR GAS SENSORS’.

Tantalum nanotube arrays *via* porous-alumina-assisted electrodeposition from ionic liquid: Electrical characterization

H. Simunkova[1], L. Kalina[2], J. Bousek[1,3], A. Mozalev[3]
[1]Department of Microelectronics, Brno University of Technology (BUT), Czech Republic
[2]Materials Research Centre, Faculty of Chemistry, BUT, Czech Republic
[3]Central European Institute of Technology (CEITEC), BUT, Czech Republic
simunkova@feec.vutbr.cz

Abstract. Tantalum nanotube arrays were prepared *via* porous anodic alumina (PAA) assisted electrodeposited (ED) on substrates. The ED was performed following the electrochemical/chemical preparation of PAA template on a layer of refractory metals sputtered onto a Si-wafer, without any additional steps needed usually for making the "bottom" side of the PAA template conductive. Mechanically stable, free-standing and spatially-separated tantalum nanotubes were electrodeposited potentiostatically at -1.4V vs. Pt with a high uniformity and population density across the sample surface. The films were characterized by scanning electron microscopy (SEM) and electrochemical impedance spectroscopy (EIS) in solution and after making top metal electrodes *via* a magnetron sputtering method. The electrical charge resistance of the ED Ta nanostructures was estimated to be about 50 $\Omega \cdot cm^2$. Potential applications of films developed here are as nanostructured electrodes for capacitors, chemical sensors, switching and memristic microdevices.

Introduction

Development of three-dimensional (3-D) tantalum and tantalum oxide nanostructures is of particular interest for potential applications in microelectronic devices with an enlarged surface-to-volume ratios, e.g., metal-insulator-metal (MIM) capacitors, electrochemical sensors, resistive switchers or emerging random access memories (RAMs) including resistive RAMs (RRAMs).

Electrochemical deposition or electrodeposition (ED) is an advantageous technique because it gives access to a low-temperature, inexpensive, scalable process that allows growth of a wide variety of metals and semiconductors. Template-assisted electrodeposition is, furthermore, an elegant and economical approach for the large-scale synthesis of 3D nanostructured materials, such as highly ordered porous films and free-standing nanorods/nanowires [1].

To the best of our knowledge, there have been few reports on templated ED of the only valve metal – aluminium - from non-aqueous media on a metal layer sputtered on the back side of thick porous anodic alumina (PAA) or polycarbonate membranes with open pores, i.e. without the alumina barrier layer [2,3,4,5].

Herein, we have developed a technique for electrodeposition of tantalum nanotube arrays *via* a thin PAA template in the ionic liquid 1-butyl-1-methyl-pyrrolidinium bis(tri-fluoromethylsulphonyl)imide ([BMP]Tf_2N). A metal conductive layer on the bottom of the PAA template which is necessary for ED was made by an original technique employing anodizing of aluminium on a different valve metal, both sputtered onto a microelecronic substrate. Free-standing, vertically aligned tantalum nanotube arrays were obtained after the chemical dissolution of the PAA template. A schematic diagram of the tantalum electrodeposition upon an underlaying metal, including the process for alumina barrier layer dissolution, is shown in Fig. 1.

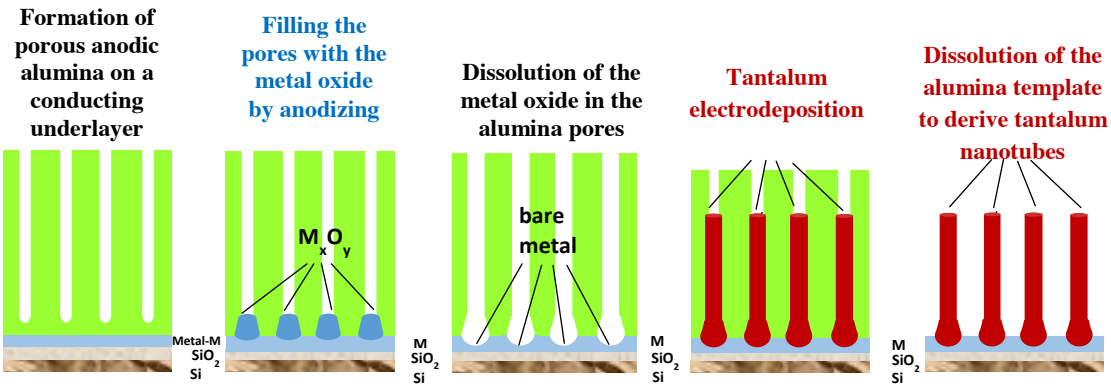

Figure 1. Schematic of tantalum electrodeposition upon a layer of metal involving the barrier layer dissolution step

Experimental

The porous anodic alumina template, having ~100-nm wide and 1-µm long pores of ~10^9 cm^{-2} population density, was prepared by anodization of a layer of Al over a valve metal layer sputter-deposited onto an oxide-coated Si wafer. ED of Ta was carried out using IL 1-butyl-1-methylpyrrolidinium bis(trifluoro-methylsulfonyl) imide, ([BMP]Tf_2N) (Solvionic, 99.9 %), containing 0.25 M TaF_5 (Alfa Aesar, 99.9 %) and 0.25 M LiF (Alfa Aesar, 99.99%) under inert gas conditions (H_2O, O_2 < 15 ppm). Tantalum was electrodeposited potentiostatically at -1.4 V vs. platinum wire at 200 °C.

Electrochemical impedance spectroscopy (EIS) was performed in H_3BO_3 (0.5M) + $Na_2B_4O_7$ (0.05M) solution with a 3-electrode arrangement. Electrochemical measurements were performed using µAutolabIII potentiostate/FR analyzer (Metrohm). A high-resolution scanning electron microscopy was utilised to investigate the surface morphology of the deposited films in a MIRA TESCAN device.

Results

The cyclic voltammogram of a gold sputter-deposited upon glass-ceramic Sitall substrate with a Ni/Cr adhesion layer in the ionic liquid ([BMP]Tf_2N) with 0.25 M TaF_5 and 0.25 M LiF is depicted in Fig. 2. The electroreduction of tantalum ions occurs at a potential of about -1.4 V versus Pt. In the reverse scan, the anodic branch of the cyclic voltammogram crosses the cathodic one to produce a current loop that is usually due to nucleation [1]. Two anodic peaks were observed on the anodic branch of the cyclic voltammogram in the range -0.5 to 0.2 V vs. Pt as a result of oxidation of the electroreduced tantalum species. At a potential of about 1.3V and above, a further oxidation of the electrodeposited layer took place as well as the electrochemical gold dissolution. The electrochemical reduction of tantalum *via* the PAA template happened at a similar electrical potential as on the planar gold surface in the same ionic liquid.

To investigate the growth of Ta nanotubes inside the PAA template, chronoamperometry measurements were performed. Fig. 3 shows the chronoamperogram obtained during the growth of Ta nanotubes from the bottom of the PAA template to the top. A similar result was obtained by El Abedin and Endres [1] during the ED of Al *via* the gold-sputtered polycarbonate membrane. Once a potential was applied, a charged double layer forms at the electrode/ionic-liquid interface and the reduction of the electroactive species directly located at the interface causes a concentration gradient and a thickening of the diffusion zone, leading to the rapid decrease of the cathodic current after a short time [1]. Subsequently, the current slowly increases due to the growth of Ta inside the pores followed by a more significant increase in the cathodic current due to a faster diffusion near to thepore uotlwts. When about 0.075 coulombs/cm^2 have been reduced on the cathode (in the case of 1-µm long pores), a limiting current plateau was observed as more tantalum ions were required for the electrodeposition of the top layer due to an increase in the effective area of the electrode.

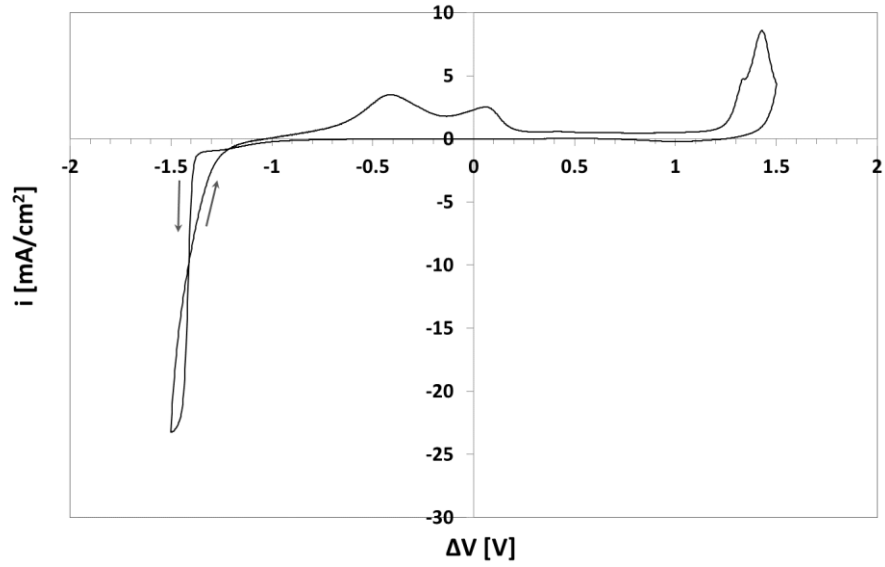

Figure 2. Cyclic voltammogram for tantalum electrodepostion on a gold layer sputter-deposited upon a glass-ceramic Sitall substrate in ([BMP]Tf_2N) with 0.25 M TaF_2 and 0.25 M LiF at a scan rate of 100 mVs^{-1}. Electrical potential was measured vs. Pt wire.

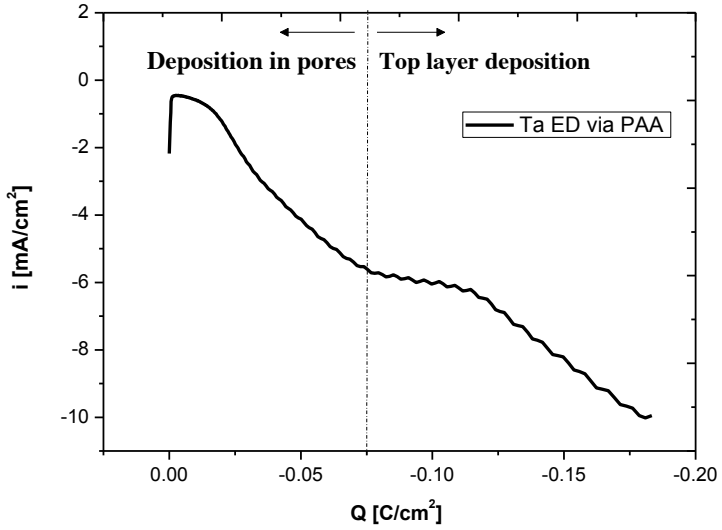

Figure 3. Chronoamperometry of tantalum elecrodeposition at a constant potential of -1.4 V vs. Pt *via* aporous anodic alumina template having 1 µm long and 100 nm wide pores at 200˚C.

Up to 1 µm long and 50-300 nm wide tantalum nanotubes were prepared by using different PAA templates. Each single nanotube was free-standing without any hint of flocking with adjacent tubes. Furthermore, the nanotubes were mechanically tough and well anchored to the bottom layer. The tops were formed either as caps or just sealed as the result of the growing top layer. In the first case, caps were observed soon after the tubes came out from the pores while in the second case a web-like spreading of the deposit was made over the PAA top, sealing finally also the pore outlets.

Figure 4 shows SEM micrographs of Ta nanotube arrays obtained by potentiostatic ED at -1.4 vs. Pt *via* a PAA template. Before SEM imaging the PAA template was selectively dissolved. The empty interiors of the nanotubes are revealed as well as a cracked Ta layer with the top caps being chopped off, as shown in the SEM images of Fig. 4c.

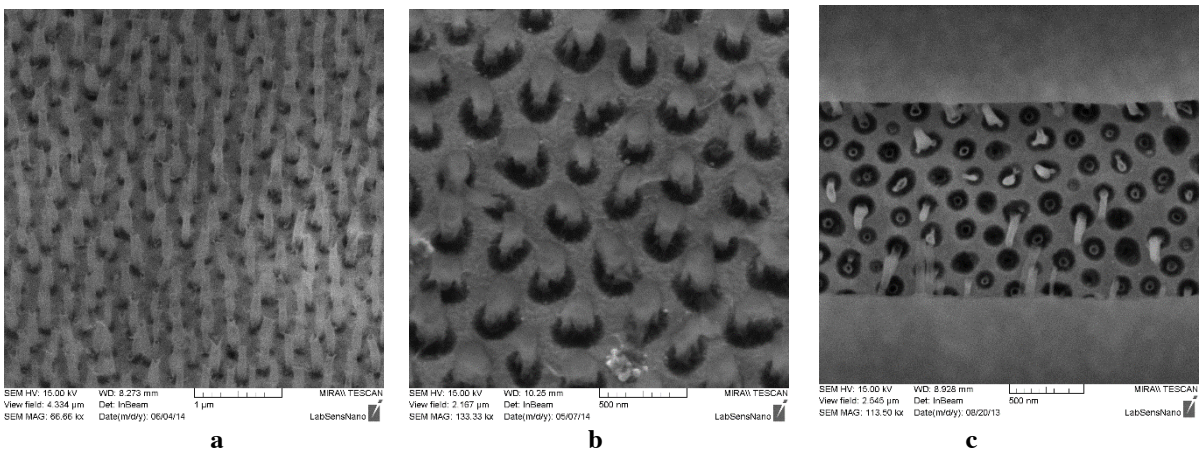

Figure 4. SEM images of Ta nanotube arrays prepared via PAA template electrodeposition at constant potential of -1.4V and 200°C. The PAA template was dissolved before SEM imaging. The picture on the right is a detail of a cracked Ta layer revealing the inner part the nanotubes with the top caps being chopped off.

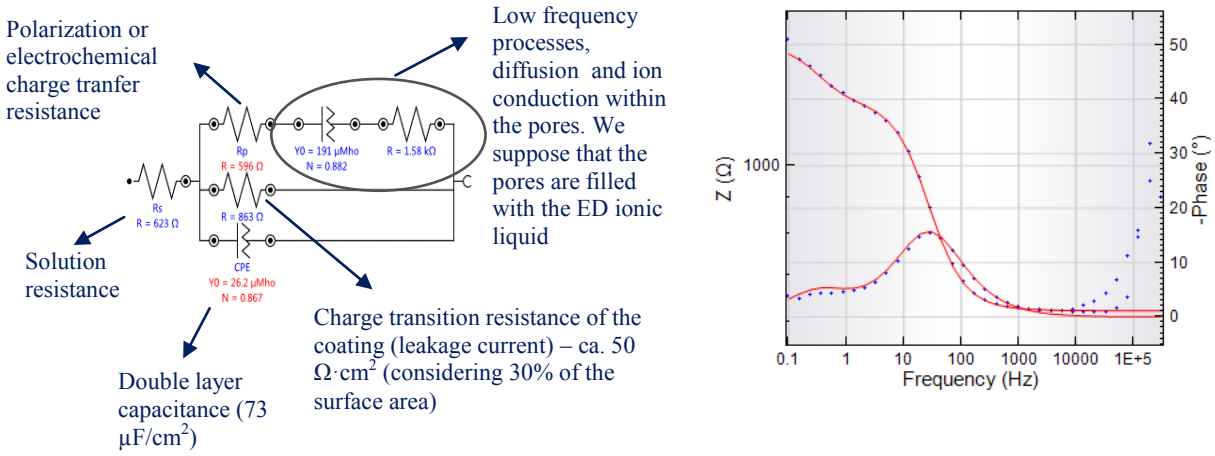

a **b**

Figure 5. Characterization of electrical parameters of the Ta ED nanoarrays supported by a 3-D PAA template by means of the electrochemical impedance spectroscopy (EIS): (a) an equivalent circuit with a good fit to the measured data, (b) relevant bode diagrams

Furthermore, EIS examination was performed on the ED Ta nanostructured samples supported with the PAA template. An equivalent circuit with a good fit to the measured data was suggested and is shown in Fig. 5. The electrical charge resistance of the ED Ta was evaluated to be about 50 $\Omega \cdot cm^2$.

Conclusions

The present findings revealed that electrodeposition of tantalum from the ionic liquid through nanopores in a PAA template grown on a metal layer onto a microelectronic substrate was practically possible and occurred in the form of tubes, which have an empty interior and grow due to the reduction of charged tantalum species along the pore walls only. A completely electrochemistry based technique, including anodization of aluminium to grow a thin film PAA template followed by refractory metal electrodeposition *via* the alumina pores was demonstrated in the ionic liquid. The estimation of the pore filling duration was shown by means of the chronoamperometry measurement. Mechanically stable Ta nanotube arrays wave been successfully synthesized. The electrical charge resistance was evaluated by electrochemical impedance spectroscopy and was found to be about 50 $\Omega \cdot cm^2$. The success of this work allows for further development of electrochemistry-based technology for nanostructured electronic devices, such capacitors with superior characteristics, chemical sensors and switching or memristic elements.

Acknowledgements

Parts of research leading to these results were supported in part by project CZ.1.07/2.3.00/30.0039 of BUT, by The Czech Science Foundation (GAČR) grant no.14-29531S and by project CZ.1.05/2.1.00/01.0012.

References

[1] El Abedin S. Z. and Endres F. 2012 *ChemPhysChem* 13, 250
[2] Pomfret M. B., Brown D. J., Epshteyn A., Purdy A. W., Owrutsky J. C. 2008 *Chem. Mater.* 20, 5945
[3] Perre E., Nyholm L., Gustafsson T., Taberna P.-L., Simon P., Edstrom K. 2008 *Electrochem. Commun.* 10, 1467
[4] Cheah S. K., Perre E., Rooth M., Fondell M., Harsta A., Nyholm L., Boman M., Gustafsson T., Lu J., Simon P., Edstrom K. 2009 *Nano Lett.* 9, 3230
[5] Oltean G., Nyholm L., Edstrom K. 2011 *Electrochim. Acta* 56, 3203

Anodic growth and use of highly-aligned refractory metal oxide nanostructures

A. Mozalev
Central European Institute of Technology (CEITEC), Brno University of Technology (BUT), Brno, Czech Republic
alexander.mozalev@ceitec.vutbr.cz

Abstract Nanostructured refractory oxides possess various useful properties, such as superconductivity, magneto-resistance, catalytic activity, electrochromism, gas sensitivity, etc. Alignment of nanostructures is a prerequisite to use their collective properties in gas sensors, energy conversion, distribution and storage microdevices. Here we describe an approach to achieve electrochemical fabrication of self-organized high aspect ratio refractory metal oxide nanostructured layers via electrochemical anodizing of valve metal bilayers. Up to date, the nanostructured metal oxide films have been successfully derived from Al/Ta, Al/Nb, Al/Ti, Al/Zr and Al/Zr-W bilayers. The films' formation-structure-properties have been studied in pursuit of new functionalities and more potential applications in microelectronics, self-cleaning surfaces, proton conducting membranes, gas sensors, photoelectrochemical water splitting and most recently developed 3-D MIM nanofilms employing anisotropic electron transport for advanced nanotechnological applications.

Introduction and motivation

Refractory metal (including valve metal) oxides possess various useful properties, such as superconductivity, magneto-resistance, catalytic activity, electrochromism, gas sensitivity and many more. Nanostructuring of metal oxides is an active and competitive area of research as it offers unprecedented opportunities for the development of advanced materials and microsystem components at the nanoscale with improved performances or substantially enhanced properties. Alignment of nanostructures over a large area of substrates is a prerequisite to use their collective properties, e.g., in gas sensors, energy conversion, distribution and storage microdevices.

In this work we describe an approach to achieve electrochemical fabrication of self-organized high aspect ratio metal oxide layers with meso-scale feature sizes *via* electrochemical anodizing of valve metal bilayers comprising a thin layer of Al superimposed on a layer of different metal [1]. In the approach, the Al layer is first converted into its nanoporous oxide, this being sequentially followed by anodizing the underlying metal through the alumina nanopores. The alumina layer is used not just as a porous mask but as part of the complex electrochemical system, included in a series of electrochemical and solid-state reactions.

Results and perspectives

A schematic diagram that outlines the main formation steps involved in the formation procedure is shown in Fig. 1. Several highly promising geometries - nanodots, nanocolumns, nanocapsules and nanotubes - can be produced under controlled electrochemical conditions, shown in Fig. 2. The most recently synthesized WO_3 nanocolumns and nanotubes are shown in SEM images of Fig. 3.

The detailed morphological features, such as the shape, size and mutual arrangement of nanostructures can be precisely controlled by a variation of the anodization parameters. Moreover, a high temperature annealing can be used to crystallize the as-anodized amorphous nanostructures to achieve a variety of crystalline modifications. Different doping and band-gap engineering approaches are feasible and will be elaborated in future works.

Up to date, nanostructured metal oxide films have been successfully synthesized from the Al/Ta, Al/Nb, Al/W, Al/Zr and Al/Zr-W [1-5] bilayers. The experimental findings have helped better understand the ion and proton transport processes determining the growth and post-formed behavior of these metal oxide nanostructures in pursuit of new functionalities and more potential applications in microelectronics, optics, optoelectronics, functional coating including self-cleaning surfaces, proton conducting membranes, chemiresistive gas sensors, including the most recently developed 3-D metal-oxide-metal nanostructures that merge the benefits of advanced nanocomposite inorganic materials with the flexibility of non-lithographic electrochemical technologies based on anodization of aluminium and on the porous-anodic-alumina-assisted anodizing of a variety of refractory (valve) metals.

To demonstrate the capability of the 3-D film formation approach, several types of nanofilms were synthesized on substrates *via* anodizing sputtered Al/Nb metal layers and additionally tailoring film parameters by combining post-anodizing chemical treatments and high temperature annealing.

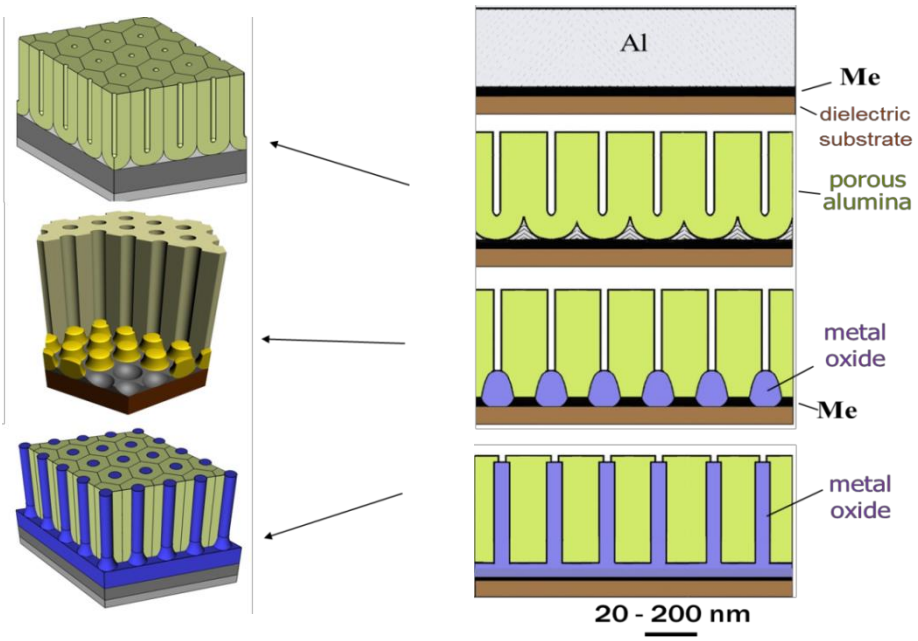

Figure 1. Schematic diagram showing the main steps of forming self-aligned refractory metal oxide nanostructures *via* the porous-alumina-assisted anodizing of Al/Me bilayers on substrates

The 3-D films are composed of an array of well-defined, size-tailored, long-aspect-ratio columnlike metal-oxide protrusions, 20-200 nm in diameter, self-directed in the alumina nanopores, up to 1 μm long, in some cases being also anchored to a lower solid portion of corresponding oxide, having graded oxygen composition, as shown in Fig. 5. A patterned noble-metal layer is formed on the column tops via the original point electrodeposition technique; the non-anodized metal layer serves as the bottom electrode. For purpose-built applications, the alumina may be selectively dissolved away, and a patterned network of vertically aligned, bottom- and top-interconnected metal-oxide nanocolumns is derived (Fig. 5). SEM, TEM, XRD, XPS, EDX, electrical/dielectric measurements have been employed to reveal the films' formation-structure-property relationship and define the areas of potential applications (to be reported in due course).

In comparison with the Nb_2O_5 columnlike film tested in the in-plane configuration in our previous works [1,2], the 3-D Nb_2O_5 nanofilm revealed the extraordinary thermistor properties, the higher sensor response to H_2 and the greatly improved performance in ethanol detection (collaborative work with MINOS group of Universitat Rovira I Virgili, Tarragona, Spain) [6].

The results of testing applicability of the films as the photoanode for electrochemical water oxidation and hydrogen generation show that the photoelectroactivity of the tungsten oxide nano-arrays was about 5 times better than that of a flat WO_3 sample used as reference while the 2–4 orders of magnitude current increase was registered in the nanostructured sample under the illumination vs. the dark current (collaborative work with the Christian Doppler Laboratory for Combinatorial Oxide Chemistry at the ICTAS, JKU Linz, Austria).

Additionally to the above applications, the films have a high potential for utilization in optoelectronics, integral optics, field-emission displays, dye-sensitized solar cells and photocatalytic devices.

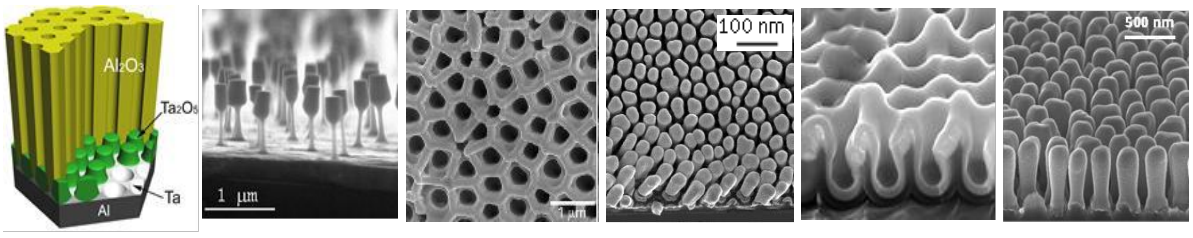

a **b** **c** **d**

Figure 2. Schematic view and SEM images of the variety of metal oxide nanostructures fabricated *via* the porous-anodic-alumina-assisted anodization of refractory metals sputtered on substrates

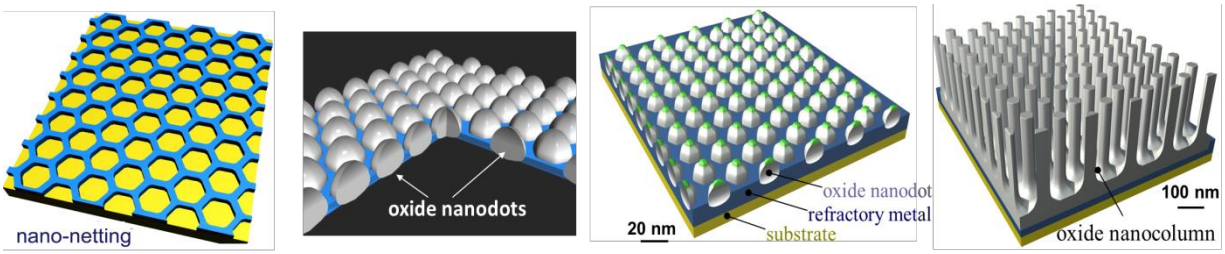

Figure 3. Computer-modeled metal and metal-oxide nanostructures fabricated via self-organized anodization of Al/Me layers (Me-Ta, Nb, Ti, W, etc.): metallic nano-grid (a), metal-oxide nano-dots (b, c) and metal-oxide nano-columns (d)

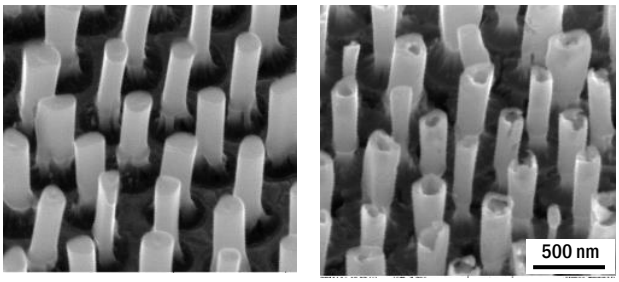

a **b**

Figure 4. SEM images of tungsten oxide nanocapsule (a) and nanotube (b) arrays derived from anodically oxidized Al/W metal layers sputter-deposited onto a Si wafer

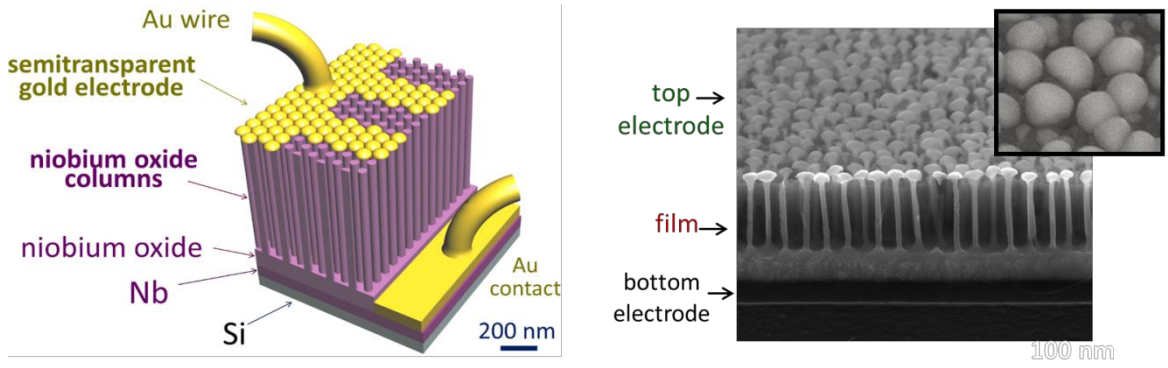

a **b**

Figure 5. Schematic view (a) and SEM images (b) of a novel 3-D nanofilm derived from the anodized Al/Nb bilayer on a Si wafer.

Acknowledgement

Parts of research leading to these results were supported by Czech Science Foundation (GAČR) grant no. 14-29531S, by NATO SPS project ISEG.MD.SFP 984511 and by project CZ.1.07/2.3.00/30.0005 of BUT.

References

[1] Mozalev A., Vazquez R.M., Bittencourt C. et al., 2014 *J. Mater. Chem. C* 2, 4847
[2] Vazquez R.M., Mozalev A., Llobet E. 2014 *Procedia Engineering* 87, 811
[3] Mozalev A., Khatko V., Bittencourt C. et al., 2008 *Chem. Mater.* 20, 6482
[4] Vazquez R.M., Mozalev A., Calavia R., et al., 2014 *Sens. Actuat.* B 204, 588
[5] Mozalev A., Gorokh G., Sakairi M., Takahashi H. 2005 *J. Mater. Sci.* 40, 6399
[6] Mozalev A., Vazquez R.M., Bendova M. et al., unpublished work

Structural, microstructural and thermal stability of FeSiB nanopowders alloys prepared by mechanical

Miloud Ibrir[1], Said Lakel[2], Saadi Berri[1], Joan Joseph Suñol[3]

[1]Laboratoire de Physique des Matériaux et ses Applications
Department of Physics
University Med BOUDIAF Msila
B. P. 166, 28000 M'Sila, Algeria

[2]Laboratory of Metallic and Semiconducting Materials
Department of Physics
University of Biskra
B.P. 145, RP 07000 Biskra, Algeria

[3]Dep. de Fisica,
Universitat de Girona,
Campus Montilivi, Girona 17071, Spain

E-mail: ibrirmiloud@yahoo.fr

Abstract. Fe–Si alloys are of significant commercial and academic interests due to the large diversity of their physical properties. Fe–Si alloys can be used as starting materials for many multicomponent technical alloys. The addition of B to the Fe–Si alloys hinders coarsening of the bcc grains, increases the possibility of forming an amorphous phase and, thereby, pro-vides good magnetic properties, and gives a better thermal stability of the residual amorphous phase Structural, microstructural and thermal stability of Fe75Si15B10 (at. %) nanopowders alloys prepared by mechanical alloying from elemental powder mixture using a planetary high energy ball mill were studied as function of milling times. X-ray diffraction results show the formation of Fe2B after 5 h of milling, and Silicon diffraction peaks disappeared after 50 h of milling. Rietveld refinement of XDR patterns reveals the presence of 74 % Fe(Si, B) solid solution and 26 % Fe2B boride with cristallite size about 13 nm and 6 nm, respectively. Differential scanning calorimetry (DSC) measurements on FeSiB alloy present tow exothermic peaks. The first peak at 516 °C corresponds to the formation of the α-Fe(Si-B), the second peak at 610 °C may be associated to the crystallization of the reaming amorphous phase.

1. Introduction

Mechanical alloying (MA) has been used as a powerful nonequilibrium processing method that can produce a variety of nanocrystalline (NC) [1–7] and other non-equilibrium structures in large quantities [8–10]. MA uses severe plastic deformation to introduce defects (dislocations, grain boundaries, vacancies and interstitials) into the material which can then "self assemble" into nanoscale grains. NC materials are one class of metastable materials that are characterized by grain size of the order of a few nanometers (typically 1–100 nm), and more than 50% of atoms are associated with grain boundaries or interfacial boundaries when the grain is small enough. Consequently, a significant amount of interfacial component between neighbouring atoms located at grain boundaries contributes to the improved mechanical, physical and magnetic properties [11].

Fe–Si alloys are of significant commercial and academic interests due to the large diversity of their physical properties. Fe–Si alloys can be used as starting materials for many multicomponent technical alloys. The addition of B to the Fe–Si alloys hinders coarsening of the bcc grains, increases the possibility of forming an amorphous phase and, thereby, provides good magnetic properties, and gives a better thermal stability of the residual amorphous phase [12]. Therefore, Fe–Si–B amorphous alloys have been widely used as magnetic core materials [13–15]. Some efforts were made to synthesize Fe–B–Si alloys from elemental powders using MA [16–20]. It has been reported that ball milling produced NC solid solution [18] or only partial transformation to the amorphous state [19,20]. The outstanding magnetic properties may be obtained in NC Fe–Si–B based alloys through the amorphous phase annealing [21]. Consequently, determination of the extent to which B and Si are incorporated in the Fe crystallites during ball milling is of great interest. It has been observed that the steady state concentration of B and Si in solution during the milling process of the Fe–13B–7Si (at.%) powder mixture, in a spex mill, required 128 h. In the ball-milled Fe78Si9B13 powders, the dissolution of B and Si in the Fe lattice occurred simultaneously with crystallite size reduction.

A mixture of α-Fe, α-Fe(Si), α-Fe3(Si,B) and Fe2B phases was obtained after 300 h of milling [16]. An amorphous ferromagnetic phase was obtained in the mechanically alloyed Fe75Si15B10 powder mixture after 19 h of milling [22]. The aim of this work is to produce nanostructured Fe75Si15B10 feedstock powders for coating synthesis. Nanostructured coatings with improved mechanical, physical and magnetic properties have been synthesized from NC feedstock powders [15,23,24]. Therefore, it is important to be able to identify feedstock powder characteristics such as particle size, powder morphology, grain size, phase transformation and magnetic properties as a function of milling time. For example, the particle size which is an important parameter for thermal spraying considerably affects particle temperature and speed during flight that subsequently influences coating properties.

2. Materials and methods

Nanostructured Fe75Si15B10 (at. %) powders were prepared from pure elemental Fe (99.9%, <10_m), Si (99.9%, <45_m) and amorphous B (>99%) powders using a planetary high energy ball mill Retsch PM400/2. The milling process was performed at room temperature using hardened steel vials and balls (2 balls diameter 30 mm). The powder weight was 400 g and the powder-to-ball-weight ratio was about 2/1. The rotation speed was 250 rpm. The hardened steel vials and balls were sealed under argon atmosphere in a glove box to prevent from oxidation. In order to avoid the local temperature rise inside the vials, milling was interrupted each 1/2 h for 1/4 h. Powder morphology and particle size evolution during the milling process were followed by scanning electron microscopy (SEM) in DSM960A Zeiss equipment. The MA powders were thermally characterized by differential scanning calorimetry (DSC) in a DSC30 Mettler-Toledo equipment. Structural and microstructural changes in the milled powders were characterized by X-ray diffraction (XRD) measurements on Brucker D8 Advance diffractometer in a (θ –2θ) geometry using Cu-Kα radiation (λ = 0.154056 nm). Phase transformation and microstructural parameters (lattice parameters, crystallite size, microstrains and

phase percentage) were obtained from the full pattern XRD Rietveld fitting procedure using the MAUD program which is based on the Rietveld method [25].

The broadening of the diffraction peaks due to the strain and crystallite size effects after subtracting the instrumental broadening is given by:

$$B_s = \frac{0.9\lambda}{L\cos\theta} + 2(\sigma)\tan\theta \quad (1)$$

where Bs is the full width at half-maximum of the XRD peaks, L the crystallite size, λ the wavelength of X-ray, σ the internal microstrain and θ is the Bragg angle. Bs can be calculated as:

$$B_s^2 = B_m^2 - B_c^2 \quad (2)$$

where Bc is the width at half-maximum of the calibration peaks and Bm is the evaluated width.

3. Results and discussion

Fig. 1 shows the morphology of the powder particles before and after several milling times. For the as-received powder (0 h), a small amount of particles exhibit a spherical shape while the reminder shows an irregular morphology. Significant changes occur up to 25 h of milling as evidenced by the growing in size of the powder particles through agglomeration. On prolonged milling 150 h), cold welding and fracturing are the dominant processes as indicated by the wide distribution of particles size. This can be related partly to the nature of the starting particles since the presence of Si increases the hardness and brittleness of powders. The relatively hard particles tend to resist attrition and compressive forces and therefore, may remain less deformed. The bigger particle size of the powders milled for 150 h is more favorable for coating process which requires a powder particle size in the range of 10–50 μm.

The average particle size of the powders, obtained from a statistical set of ~100 particle son each SEM micrograph, is shown in Fig. 2 as a function of milling time. The average particle size increases with increasing milling time, reaches a maximum value of about 19 μm after 25 h (stage 1) then decreases slightly on further milling time (stage 2). Above 50 h of milling, the narrow average particle size can be related to tendency of small particles to weld together and large particles to fracture under steady-state conditions.

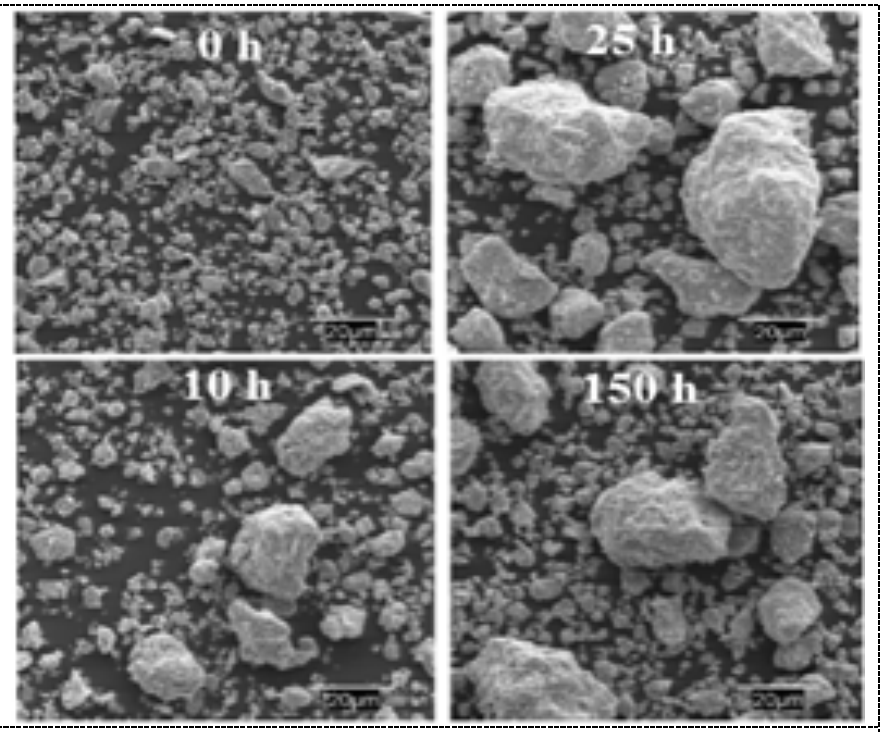

Figure 1. SEM micrographs of the as-received (0 h) and Fe75Si15B10 powders milled for 10, 25 and 150 h

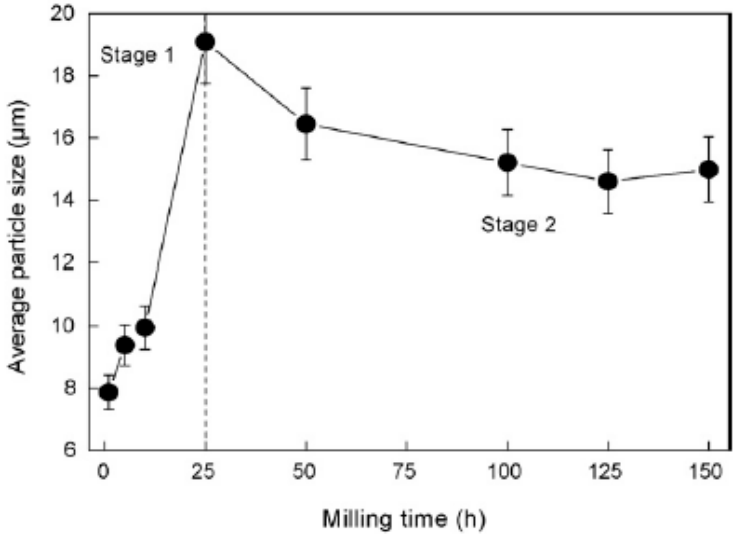

Figure 2. Average particle size variation during the milling process.

XRD analysis can provide information on the structural characteristics of materials since the width and the intensity of the diffraction peaks depend on lattice strain, crystallite size, and other imperfections in the powders such as stacking faults. The accuracy of the XRD measurements is

crucial to the quantitative analysis for grain size and microstrains which are an essential requirement for quantitative studies of NC materials.

Initial crystalline structures of reactants and products are: bcc α-Fe with lattice parameter a0 = 0.2866nm and space group Im3m; cubic Si with unit cell a0 = 5.4309 *Å* and space group Fd-3m: 1; tetragonal Fe2B boride with space group I4/mcm and unit cells a0 = 5.110 *Å* and c0 = 4.249 *Å*. Structural evolution of the ball-milled Fe75Si15B10 powders is shown in Fig. 3. The XRD pattern of the raw mixture (0 h) displays the Bragg diffraction peaks of the α-Fe and Si. B peaks are not detected owing to its low atomic scattering factor and amorphous state. The induced heavy plastic deformation into the powder particles during the milling process gives rise to the increase of crystal defects such as dislocations, vacancies and grain boundaries. Hence, the crystallite size refinement down to the nanometer scale and the increase in atomic level strain are evidenced by the broadening of the diffraction peaks and the decrease in their intensities as the milling process progresses.After 1 h of milling, it is observed inaddition to α-Fe and Si phases, the formation of α-Fe(Si, B) or α-Fe(B) solid solution (Fig. 4). According to the reduction of the Si peaks intensity, it seems that there is only a crystallite size refinement. Thereby, one can suppose that only the reaction between Fe and B proceeds at this stage of milling because of the negative enthalpy of mixing (ΔH=−38 kJ/mol), their great affinity and similar diffusion coefficient. Consequently, the formed solid solution might be α-Fe(B). The XRD patterns of the powders milled between 5 and 25 h of milling exhibit the same phases. Accordingly, the Rietveld refinement has been performed by the introduction of three phases: cubic Si, tetragonal Fe2B boride and bcc α-Fe(Si,B) solid solution (Fig. 5).

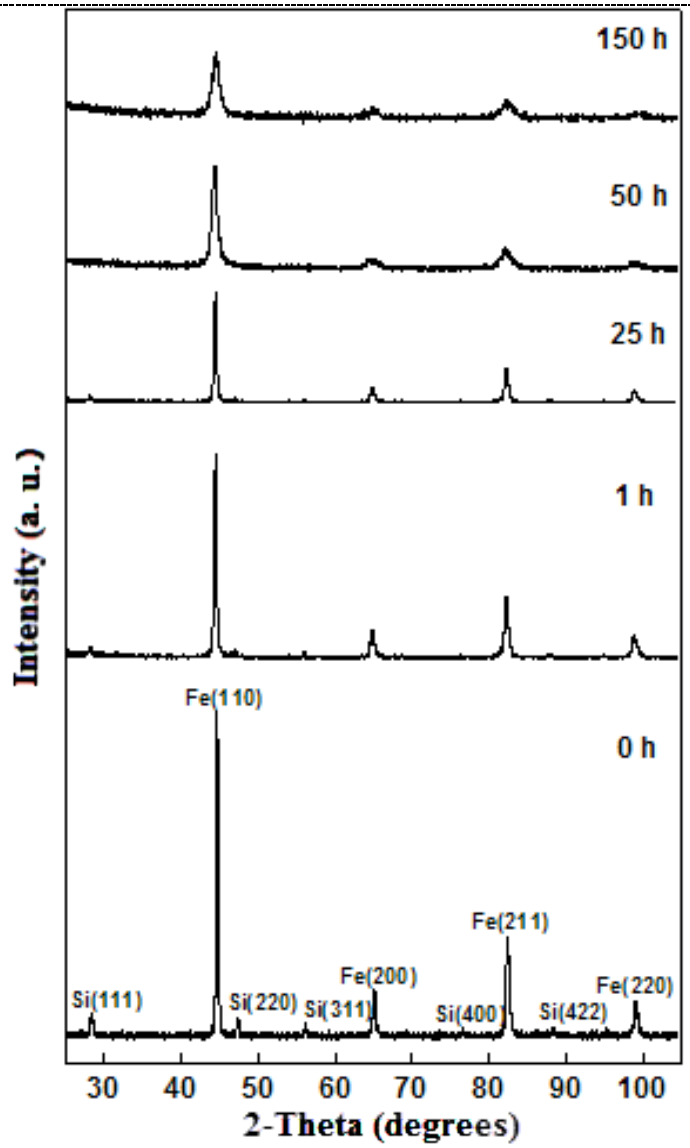

Figure 3. XRD patterns of Fe75Si15B10 powders at different milling times.

The obtained product on prolonged milling time consists of a highlydisordered α-Fe(Si,B) solid solution and Fe2B boride phase with relative proportions of about 74% and 26%, respectively (Fig. 5). The discrepancies between this result and those reported on the ball-milled Fe–Si–B powder mixtures [16–20,22] can be ascribed to the milling conditions (ball-mill type, initial elemental powders, ball-to-powder-weight ratio, milling intensity, etc.). In fact, for the ball-milled Fe75Si15B10 (at.%) powder mixture in a vibratory spex 8000 mill with a ball-to-powder weight ratio of 8:1, a fully ferromagnetic amorphous phase was obtained after 19 h of milling [22]. It appears that the energy and frequency of ball-powder-ball collisions determine the final structures such as amorphization or disordering.

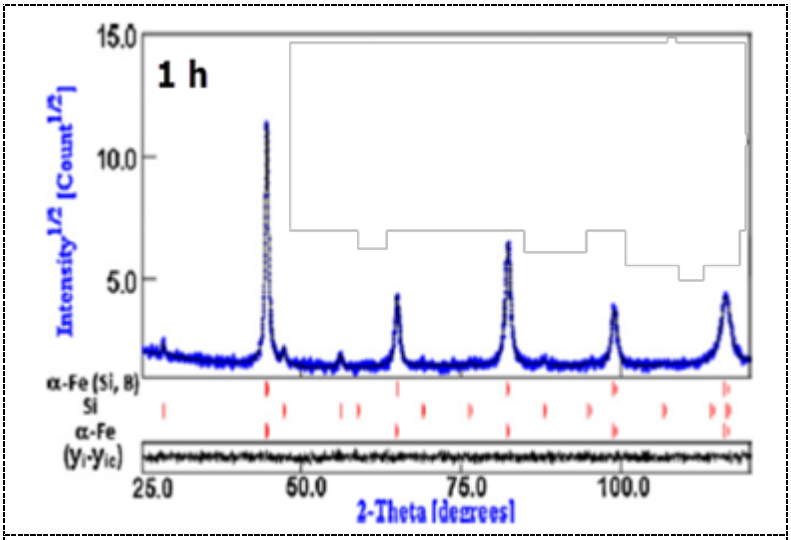

Figure 4. Rietveld refinement of the XRD pattern of the Fe75Si15B10 powder milled for 1 h.

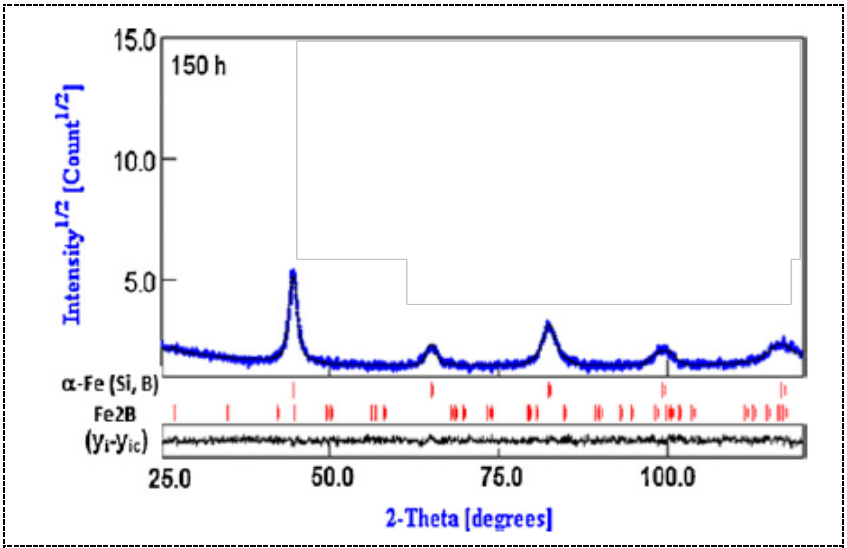

Figure 5. Rietveld refinement of the XRD pattern of the Fe75Si15B10 powder milled for 150 h.

To determine temperatures Ti for exothermic phase transformation and calculate the corresponding enthalpy change ΔHi, DSC temperature scans were performed at the heating rate 10 °C/min. Fig. 6. shows two exothermic peaks which are detected revealing a two-step crystallization process before the final stable states are reached. The first peak at 516 °C corresponds to the formation of the α-Fe(Si-B), the second peak at 610 °C may be associated to the crystallization of the reaming amorphous phase. The crystallization enthalpy ΔHi decreases rapidly with milling time until the 10 h (Fig. 7), after this time it remains constant. It is known that Ti can be associated with the final crystallization temperature for iron silicides and also for borides. Decrease of ΔHi with milling time, even against constant Ti, can be interpreted in terms of easier penetration of Si and B into the grains.

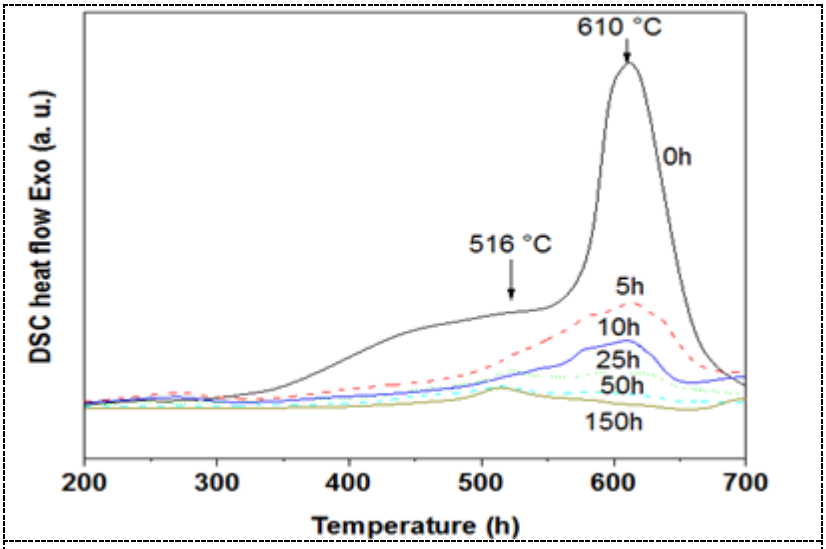

Figure 6. The linear heating DSC traces of crystallization of Fe75Si15B10 powders at different milling times.

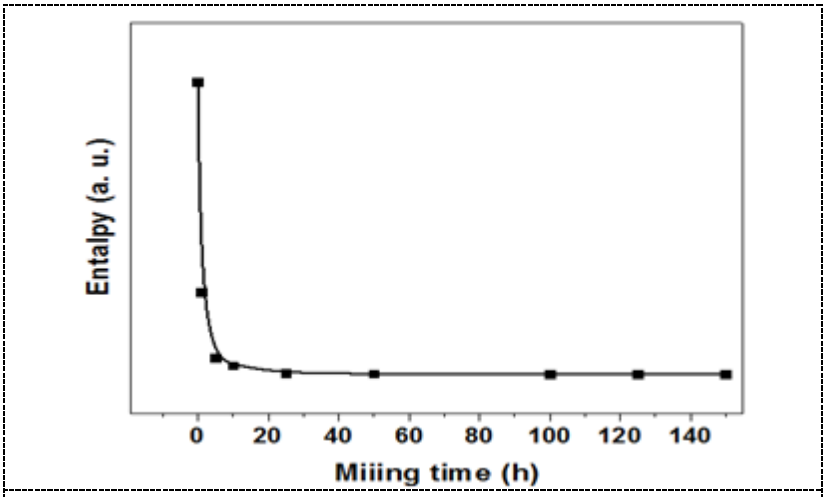

Figure 7. Enthalpie variation during the milling process of Fe75Si15B10 powders at 600 °C peak.

4. Conclusion

NC Fe75Si15B10 powder mixture was obtained by MA in a planetary ball mill. The crystallite size decreases down to the nanometer scale (6–13 nm). The reaction between Fe and B leads to the formation of bcc α-Fe(B) solid solution and Fe_2B boride after 1 h and 5 h of milling, respectively. The Si peaks disappear completely above 25 h of milling leading to its dissolution in Fe. A mixture of α-Fe (Si, B) solid solution and Fe_2B nanophase is obtained on prolonged milling time. Thermal measurements (DSC) indicated the presence two exothermic peaks at 516 °C and at 610 °C are detected revealing a two-step crystallization process before the final stable states are reached.

References

[1] Gleiter, H., (1989) 'Nanocrystalline Materials', Prog. Mater. Sci., vol 33, pp 223-315.

[2] Suryanarayana, C., (2001) 'Mechanical alloying and milling', Prog. Mater. Sci., Vol 46, Issues 1–2, pp 1–184.

[3] Alleg, S., Ibrir, M., Fenineche, N.E., Azzaza, S., Bensalem, R., Suñol, J.J., (2010) 'Magnetic and structural characterization of the mechanically alloyed Fe75Si15B10 powders', J. Alloys and Comp., Vol 494, Issues 1–2, pp 109-115.

[4] Alleg, S., Ibrir, M., Fenineche, N.E., Bensalem, R., Suñol, J.J., (2010) 'Microstructure and magnetic properties of HVOF thermally sprayed Fe75Si15B10 coatings', Surf. and Coat. Techn., Vol 205, Issue 2, pp 281-286.

[5] Alleg, S., Kartout, S., Ibrir, M., Azzaza, S., Fenineche, N.E., Suñol, J.J., (2013) 'Magnetic, structural and thermal properties of the Finemet-type powders prepared by mechanical alloying', J. of Phy. and Chem. of Sol., Vol 74, Issue 4, pp 550-557.

[6] Suñol, J.J., Escoda, L., Fort, J., Pérez, J., Pujol, T., (2008) 'Structural and magnetic properties of a nanocrystalline Fe75Nb10Si5B10 alloy produced by mechanical alloying', Mat. Lett., Vol 62, Issues 10–11, pp 1673-1676.

[7] Suñol, J.J., González, A., Saurina, J., Escoda, L., Fernández Barquín L., (2007) 'Thermal and magnetic behavior of a nanocrystalline Fe(Ni, Co) based alloy', J. Non- Cryst. Solids, Vol 353, Issues 8–10, pp 865–868.

[8] He, J., Ice, M., Lavernia, E. J., and Dallek, S., 2000, "Synthesis of Nanostructured WC-12 pct Co Coating Using Mechanical Milling and High Velocity Oxygen Fuel Thermal Spraying," Metall. Mater. Trans. A, Vol 31, pp. 541–553.

[9] Koch, C.C., (1997) 'Synthesis of nanostructured materials by mechanical milling: problems and opportunities', Nanostruct. Mater. Vol 9, Issues 1–8, pp. 13–22.

[10] Murty, B.S., Ranganathan, S., (1998) 'Novel materials synthesis by mechanical alloying/milling', Int. Mater. Rev., Vol 43, pp 101–141.

[11] Suryanarayana, C., Koch C.C., (1999) 'Chapter 12 Nanostructured materials', Perg. Mat. Series, Vol 2, pp 313-344.

[12] Ono, Y., Ichirku, T., Ohnaka, I., Yamauchi, I., (1999) 'Spinning phenomena, structure and magnetic properties of Fe–6.5 mass% Si alloy fiber produced by the in-rotating-liquid-spinning process', J. Alloys Compd. Vol 289, Issues 1–2, pp 220–227.

[13] Swartz, J.C., Kossowsky, R., Hahgh, J.J., Krause, R.F., (1981) 'Crystallization of amorphous Fe81B13.5Si3.5C2', J. Appl. Phys. 52, pp 3324–3330.

[14] Yamasaki, T., Zheng, Y. J., Ogino, Y., Terasawa, M., Mitamura, T., and Fukami, T., (2003) 'Formation of Metal-TiN/TiC Nanocomposite Powders by Mechanical Alloying and Their Consolidation', Mater. Sci. Eng. A, Vol 350, pp 168–172.

[15] Cherigui, M., Fenineche, N.E., Coddet, C., (2005) 'Structural study of iron-based microstructured and nanostructured powders sprayed by HVOF thermal spraying', Surf. Coat. Technol. Vol 192, Issue 1, pp 19–26.

[16] Pękała, M., Jachimowicz, M., Fadeeva, V.I., Matyja, H., Grabias A., (2001) 'Magnetic and structural studies of ball milled Fe78B13Si9', J. Non-Cryst. Solids, Vol 287, Issues 1–3, pp 380–384.

[17] Perez, R.J., Huang, B., Crawford, P.J., Sharif, A.A., Lavernia, E.J., (1995) 'Synthesis of nanocrystalline Fe13at.%B7at.%Si by mechanical alloying', Mater. Sci. Eng. A, Vol 204, Issues 1–2, pp 217–221.

[18] Sunol, J.J., Gonzalez, A., Saurina, J., Escoda, L.I., Bruna, P., (2004) 'Thermal and structural characterization of Fe-Nb-B alloys prepared by mechanical alloying' , Materials Science and Engineering A, Vol 375-377, pp 874-880.

[19] Suriñach, S., Baró, M.D., Segura, J., Clavaguera-Mora, M.T., Clavaguera N., (1991) 'Amorphization of soft magnetic alloys by the mechanical alloying technique', Mater. Sci. Eng. A, Vol 134, pp 1368–1371.

[20] Sakamoto, H., Yamada, T., Okumura, N., Sato T., (1996) 'Improvement in brittleness of amorphous Fe-Si-B-C alloy ribbons by controlling casting conditions', Mater. Sci. Eng. A, Vol 206, Issue 1, pp 150-153.

[21] Yoshizawa, Y., Yamauchi, K., (1991) 'Magnetic properties of FeCuMSiB (M = Cr, V, Mo, Nb, Ta, W) alloys', Mater. Sci. Eng. A, Vol 133, pp 176–179.

[22] Quispe Marcatoma, J., Peña Rodriguez, V.A., Baggio-Saitovich, E.M., (2001) 'Magnetic Properties and Crystallization of the Fe75Si15B10 Amorphous Alloy Prepared by Mechanical Alloying', Hyp. Int., Volume 148-149, Issue 1-4, pp 97-102.

[23] He, J., Schoenung, J.M., (2002) 'Nanostructured coatings', Mater. Sci. Eng. A, Vol 336, Issues 1–2, pp 274-319.

[24] Cherigui, M., Fenineche, N.E., Gupta, A., Zhang, G., Coddet, C., (2006) 'Magnetic properties of HVOF thermally sprayed coatings obtained from nanostructured powders', Surf. Coat. Technol. Vol 201, Issues 3–4, pp 1805-1813.

[25] Lutterotti, L., (2000) 'MAUD', CPD Newsletter (IUCr) 24.

Thermodynamic modeling and design of a solar lithium bromide-water absorption chiller

CH. Hamdi[1], A. Farhat[2]
[1]National Engineering School of Tunis, Tunisia,
[2]The Energy Technologies Research center of Borj Cedria,
B.P. 95, 2050. Hammam-lif, borj cedria, Tunis. Tunisia

Abstract: The solar lithium bromide-water, absorption chillers have been the subject of intensive research in the past few years, due to a number of attractive properties. Minimizing waste energy is one of its advantages which are thermally driven by low grade energy such as waste heat coming from industrial plants, solar energy that is available in most areas and representing a good source of thermal and renewable energy resources, geothermal energy. The absorption chillers also contribute to ozone depletion and greenhouse warming. by replacements for the traditionally refrigerants (CFCs and HCFCs)Which affects the ozone layer.[1-4]. This paper presents the modeling and design of the solar lithium bromide-water, absorption chillers of 8 to 20 Kw.

Keywords: Absorption chiller, Lithium bromide-water, Thermodynamic modeling, design, Heat Exchangers…

1. Introduction

The solar lithium bromide-water absorption chiller shown in figure1 is mainly composed of two systems: the solar system wich is composed of collector and tank and the absorption refrigeration system wich is essentially composed of heat exchangers that all have the same principles such as: condenser, evaporator, absorber,

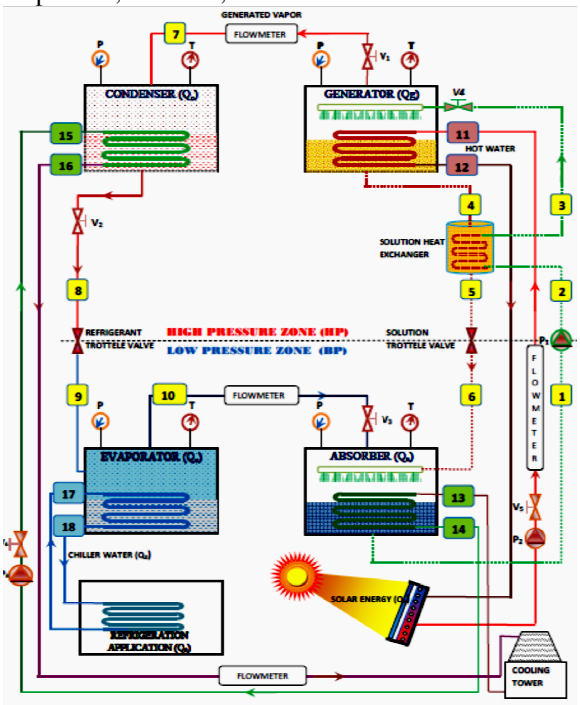

Figure1: Schematic diagram of a solar lithium bromide water absorption chiller.

solution heat exchanger and generator[5-8]. Each system has its own loop and characteristics.

2. Thermodynamic modeling:

The parameters of each component are calculated by using the basic concepts of thermodynamic principles, mass and energy balance and the correlations provided in the literature for evaporation, condensation and liquid to liquid heat transfer:

Mass balance

The mass balance of LiBr–H2O solution and lithium bromide in the solution for the main components is:

$$\sum_i \dot{m}_{in} - \sum_i \dot{m}_{out} = 0 \qquad 1$$

Concentration balance

$$\sum_i (\dot{m}X)_{in} - \sum_i (\dot{m}X)_{out} = 0 \qquad 2$$

Energy balance

Energy conservation equations could also be written for all components of the cycle:

$$\sum_i (\dot{m}h)_{in} - \sum_i (\dot{m}h)_{out} = \dot{W} - \dot{Q} \qquad 3$$

The correlations provided in the literature[9-11] for evaporation, condensation and liquid to liquid heat transfer are used in this study:

$$h_i = h(T_i, P_i, X_i) \qquad 4$$

3. Analysis and design

The algorithm displayed in Figure 2 describes the steps of design solar lithium bromide-water, absorption chillers. Q_e is equal to 10KW, first we fix inputs parameters which are generator Temperature, absorber temperatures, condenser temperature, evaporator temperature, Cooling Power Φ_0 and Heat exchanger efficacity ε; then we calculate the mean logarithmique temperature $(\Delta TLM)_i$, next we calculate: H_i, X_i, m_i, Q_i and we estimate Ui after that we calculate heat exchangers area A_i which gives the number of tubes NTb_i and the total length of the tube LT_i.

Using MATLAB, the most parameters of the machine are simulated and plotted. To fix inputs parameters we have simulate the COP versus generator temperature for different temperatures of the evaporater , the absorber and the condenser.

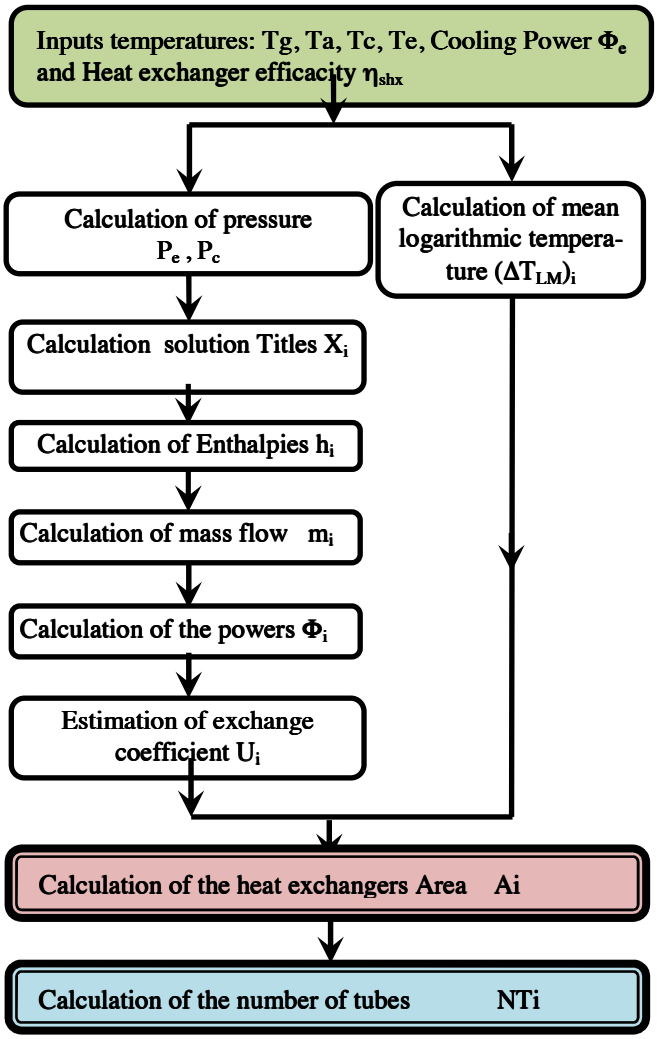

Figure2: the steps of design solar lithium bromide-water, absorption chillers

4. Results and discussion

Figure 3 present the variation of the COP with generator temperature for different evaporator temperature (6°C, 7°C, 8°C, 9°C, 10°C) at Tabsorber= 30°C and Tcondenser=35°C, this figure schow that the COP increase with increasing the evaporator temperatures.

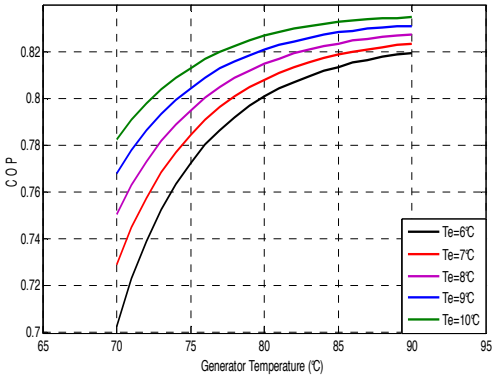

Figure3: Variation of COP with generator temperature for different evaporator temperature at Tabs= 30°C and Tcond=35°C.

The refregerarion application used in this paper oblige that the evaporator temperature does not excides 7°C, the others parameters are determinated using the variation of the COP versus generator temperature with evaporator temperature is equal to 7°C.

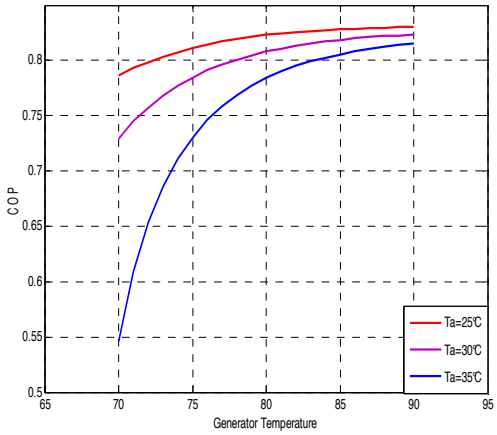

Figure4: Variation of COP with generator temperature for different absorber temperature at Tcond = 35°C and Tevap = 7°C.

Figure 4 present the variation of the COP with generator temperature for different absorber temperature (25°C, 30°C, 35°C) at Teva=7°C and Tcondenser=35°C, In figure 4 it is clearly shown that the COP increase by decreasing the absorber temperatures, then we choose the temperature of the absorber equal to 30°C.

For evaporator temperature Tevap=7°C and absorber temperature Tab=30°C, the variation of COP with generator temperature for different condenser temperature (Tc=25°C, 30°C, 35°C, 40°C) are plotted in figure5.

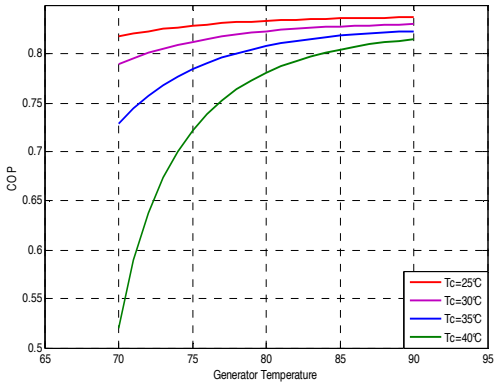

Figure5: Variation of COP with generator temperature for different condenser temperature at Tabs = 25°C and Tevap =7°C.

In figure 5 it is clearly shown that the COP increases with decreasing condenser temperatures.

Enthalpies, temperatures, mass flow rate and the heat exchangers area in each component, are calculated, using Te=7°C, Ta=30°C and Tc=35°C the numerical results are tabulated (Table1&2).

Table 1: Thermodynamic data of state points

State	H (Kj/kg)	m (Kg/s)	P (Kpa)	T (°C)	% LiBr
1	61.74	0.0219	0.994	30	50.95
2	61.74	0.0219	5.625	30	50.95
3	118.67	0.0219	5.625	56.24	50.95
4	215.14	0.0178	5.625	85	62.80
5	143.94	0.0178	5.625	46.5	62.80
6	141.16	0.0178	0.994	45	62.80
7	2652.9	0.0041	5.625	85	0
8	147.31	0.0041	5.625	35	0
9	147.31	0.0041	0.994	7	0
10	2566.7	0.0041	0.994	7	0

Qe=10kW, COP=0.82, Te=7°C, Ta=30°C, Tc=35°C, Tg=85°C, η_{shx}=0.7.

Table 2: Component design

Element	Qi (kW)	Ui (Kw/m^2k)	Ai (m^2)	NTbi	LTi (m)
Generator	12.188	1.7	0.451	10	6.02
Condenser	10.356	2.54	1.021	22	13.62
Evaporator	10.000	1.2	1.634	35	21.80
Absorber	11.764	1.75	0.596	13	7.96
Solution Heat exchanger	1.250	0.2	0.282	6	3.77

5. conclusion

The water lithium bromide absorption machine was studied theoretically in this paper, based on the basic concepts of thermodynamic principles, mass and energy balance and the correlations provided in the literature the performance of the machine was calculated. To evaluate the heat exchangers Area A_i and calculate the number of tubes a detailed solution algorithm was presented and validated.

References:

[1] Tawatchai Jaruwongwittaya, Guangming Chen "A review: Renewable energy with absorption chillers in Thailand"

[2] Arun Bangotra, Anshul Mahajan "Design Analysis Of 3 TR Aqua Ammoniavapour Absorption Refrigeration System" Mechanical Engineering Department, Government Polytechnic College, Jammu, J&K, India, 180004.

[3] Horuz, T.M.S Callander, "Experimental investigation of a vapour absorption refrigeration system" Department of Mechanicalengineering,

[4] Bakhtiari, B., Fradette, L, Legros, R., Paris, J., 2011. « A model for nalysis and design of H2OeLiBr absorption heat pumps" Energy Convers. Manage. 52, 1439e1448.

[5] K. E. N'Tsoukpoe, H. Liu, N. Le Pierrès, L. Luo, "A review on long-term sorption solar energy storage" *Ren. and Sus. Energy Rev.*, 13 (2009), 2385–2396.

[6] Bulgan AT. Optimization of the thermodynamic model of aqua-ammonia absorption refrigeration systems. Energy Convers Manag 1995;36(2):135e43.

[7] Ben Ezzine N, Barhoumi M, Mejbri Kh, Chemkhi S, Bellagi A. Solar cooling with the absorption principle: first and second law analysis of an ammonia-water double-generator absorption chiller. Desalination 2004;168:137e44.

[8] Florides GA, Kalogirou SA, Tassou SA, Wrobel LC. Modelling and simulation of an absorption solar cooling system for Cyprus. Sol Energy 2002: 43–51.

[9] ASHRAE. Handbook of fundamentals ASHRAE 1997

[10] Jason Wonchala, Maxwell Hazledine, Kiari Goni Boulama "Solution procedure and performance evaluation for a watereLiBr absorption refrigeration machine" Department of Mechanical and Aerospace Engineering, Royal Military College of Canada.

[11] Tiago Mateus a,b, Armando C. Oliveira a"Energy and economic analysis of an integrated solar absorption cooling and heating system in different building types and climates"

Nomenclature

Variable		Désignation
A	m^2	area
C	$Kj.Kg^{-1}.°C^{-1}$	specific heat capacity
h	$Kj.Kg^{-1}$	enthalpy
m	$Kg.s^{-1}$	mass flow rate
P	Pa	pressure
Q	kW	heat flux
T	°C	temperature
UA	$kW\ K^{-1}$	heat transfer coefficient
X	$Kg_{salt}/\ kg_{Sol}$	solution mass fraction
η	%	Solution heat exchanger efficiency
Indice		
i=(a,e,c,g,shx)		Element
in		input
out		output
shx		Solution Heat exchanger
a		Absorber
c		Condenser
e		Evaporator
g		Generator

Acute hepatotoxicity of zinc oxide nanoparticles in Wistar rats

H.Ben Miled, Z.Ben Barka, Y.Baratli, M. Tlili, H.Abdelmelek, M. Sakly, K. Ben Rhouma , Olfa Tebourbi
Laboratory of Integrated Physiology Science Faculty of Bizerte,7021 Jarzouna, Tunisia
tebourbi.olfa@gmail.com

Abstract: Various engineered nanomaterials have already been introduced into a number of industrial processes and innovative products. However, their potential hazards on mammalian and humans remain largely unknown (Aschberger et al., 2011). As a result of their unique physicochemical properties, nanoparticles are becoming present in sunscreens, toothpastes, sanitary ware coatings and even food products. Currently, researchers are focusing on many areas such as applied physics and chemistry, mechanical and electrical engineering, nanotoxicology, nanobiology, and nanomedecine, industrial applications and environmental investigations (Ferreira et al., 2013).

Zinc oxide nanoparticles (ZnO NPs) are used in a wide range of products including cosmetics, food packaging, imaging, etc. The present study was conducted on Wistar male rats and aimed to investigate the acute oral toxicity of ZnO NPs (0.5 and 1g/kg of body weight). The rats were sacrificed after 24h, 48h, 7, 15 and 30 days of ZnO NPs administration and blood samples were collected for assaying serum biochemical parameters. Liver histopathological examination was also performed.

Our results showed a significant accumulation of nanoparticles in the liver of treated animals leading to cellular injury including steatosis, inflammation, hepatocyte ballooning and later necrosis. Such damage was confirmed by the increase of serum activities of alanine aminotransferase (ALAT) and aspartate aminotransferase (ASAT) as well as creatinine, uric acid and total proteins levels.

These findings showed that acute oral exposure to 15nm- sized ZnO NPs in Wistar rat leads to hepatic accumulation of nanoparticles and induces liver dysfunction. These results also suggest the need for a complete risk assessment of any new engineered nanoparticles before its arrival into the consumer market.

Key words: ZnO nanoparticles, rats, liver, toxicity

1.Introduction:

A nanoparticle is the most fundamental component in the fabrication of a nanostructure, and may be defined as a particle that has a characteristic dimension from 1 to 100 nm. The term “nanoparticles” applies only to engineered particles (such as metal oxides, carbon nanotubes, fullerenes etc.) and does not apply to particles under 100 nm that occur naturally or are by products of other processes such as welding fumes, fire smoke, or carbon black (Hoyt and Mason, 2008). Zinc oxide nanoparticles (ZnO NPs) have been used for decomposition of some organic compounds under the ultraviolet illumination (Wang et al., 2007; Xu et al., 2007).

Many studies have reported that ZnO NPs could induce apoptosis in human dermal fibroblasts via p53 and p38 pathways (Meyer et al., 2011). In addition , ZnO NPs may produce cytotoxicity on the liver and kidney cells in mice via induction of oxidative stress, DNA damage and apoptosis (Li et al., 2011, Sharma et al., 2011; Sharma et al., 2012), both broncho-alveolar lavage cells and white blood cells in rats via interfering with zinc ion homeostasis (Kao et al., 2012), human bronchial epithelial cells (Heng et al., 2010) and Escherichia coli via oxidative stress (Brayner et al., 2006; Kumar et al., 2011). Therefore, in this study we propose to investigate the acute oral toxicity of ZnO NPs (0.5 and 1g/kg of body weight) on male Wistar rats liver.

2.Material and methods:

2.1. Animals:

Wistar albino male rats (3–4 weeks old and weighing 100-120g) purchased from Pasteur institute, Tunisia, were used in this study. They were housed in polypropylene cages with 12h light and dark cycle. Animals were fed standard pellet feed and water.

2.2. Experimental design:

Wistar male rats were treated with two acute oral dose of ZnO NPs (0.5 and 1g/kg of body weight).The rats were sacrificed after 24h, 48h, 7, 15 and 30 days of ZnO NPs administration and blood samples were collected for assaying serum biochemical parameters. Liver histopathological examination was also performed.

2.3 Biochemical determinations

The biochemical parameters like serum enzymes: aspartate aminotransferase (ASAT), alanine aminotransferase (ALAT), creatinine, uric acid and total proteins were assayed using assay kits (*BIOMAGHREB* , Tunisia).

2.4. Histopathological studies:

The liver tissue was dissected out and fixed in 10% formalin. Sections were prepared and then stained with hematoxylin and eosin (H–E) dye for photomicroscopic observation, including cell necrosis, fatty change, hyaline regeneration, ballooning degeneration.

2.5 Statistical analysis

The data are expressed as mean ± SD. The difference among means has been analyzed by one-way ANOVA. A value of $P < 0.05$ was considered as statistically significant.

3.Results and discussion:

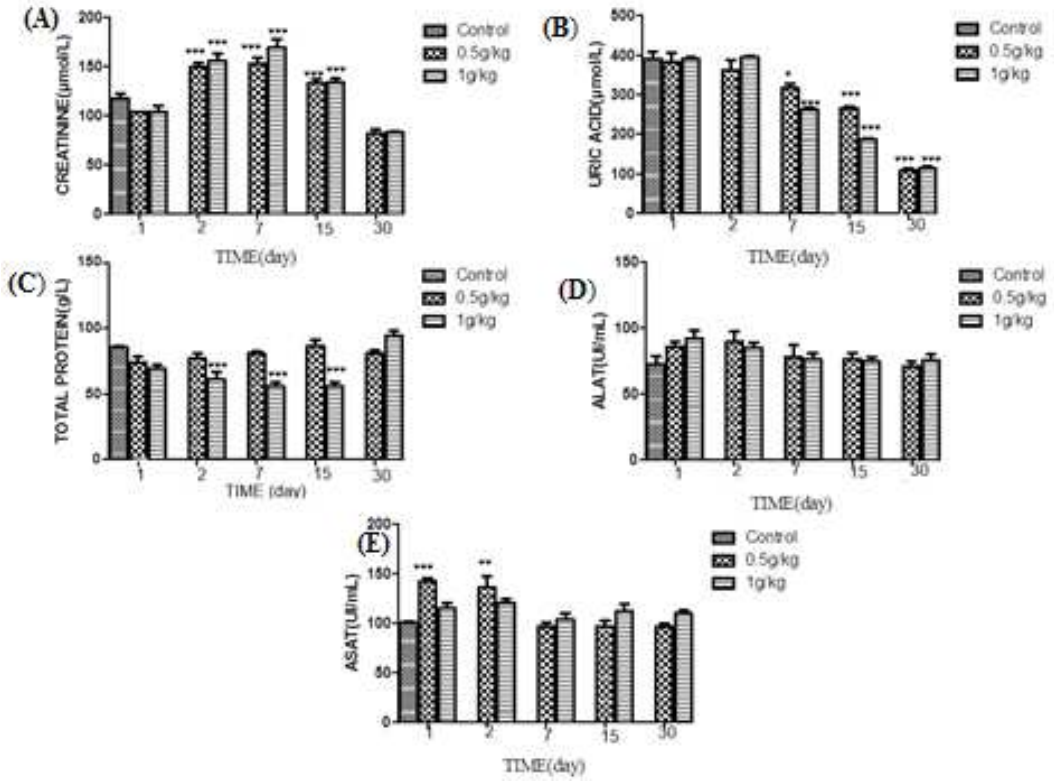

Figure 1*.Effect of a single injection ZnO NPs on serum biomarkers levels. (A) creatinine, (B) uric acid, (C) total proteins, (D) serum glutamate pyruvate transaminase (ALAT), (E) aspartate aminotransferase (ASAT).*

** p<0,05 ; ** p<0,01 ; *** p<0,001 vs control (Test one-way ANOVA followed by Tukey test).*

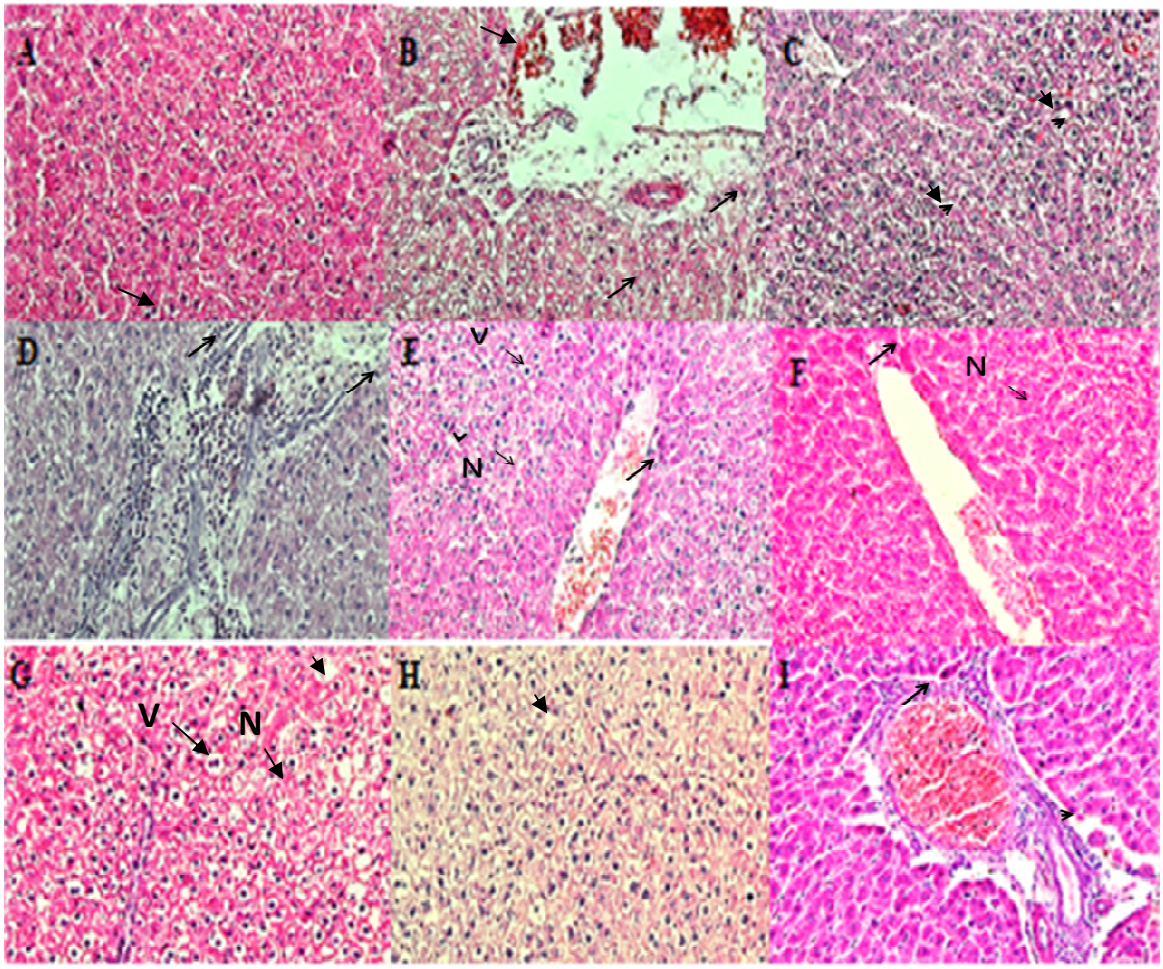

Figure 2. *Histopathology of rat liver after ZnO NPs exposure: (A) Section of liver of control rat showing hepatic cells with nuclei, cytoplasm, central vein and portal triad (HE×25). (B)Liver section of rats killed 24h after oral administration of 0.5 g/kg of ZnO NPs with: significant vascular congestion (arrows) (HE×40). (C) Liver section of rats killed 48h after oral administration of 0.5 g/kg of ZnO NPs showing edematous rearrangements (HE×40) (arrowheads). (D) Liver section of rats killed 72h after oral administration of 0.5 g/kg of ZnO NPs showing inflammatory infiltrate intra-portal polymorphic and rich in eosinophils (HE×40) (Arrows). (E) Liver section of rats killed 15 days after oral administration of 0.5 g/kg of ZnO NPs showing vascular congestion (arrows), cell vacuolization (v), necrosis (N) features and edema (arrowheads) (HE×40). (F). Liver section of rats killed 24h after oral administration of 1 g/kg of ZnO NPs showing vascular congestion (arrow) and focal necrosis (N)(HE×40). (G) Liver section of rats killed 24h after oral administration of 1g/kg of ZnO NPs showing edematous rearrangements and similar features to E (HE×40). (H) Liver section of rats killed 24h after oral administration of 1g/kg of ZnO NPs showing edematous rearrangements (arrowhead) (HE×40). (I) Liver section of rats killed 24h after oral administration of 1g/kg of ZnO NPs showing vascular congestion (arrowhead) and inflammatory infiltration (arrow) (HE×40).*

ZnO NPs are used in consumer products such as sunscreen, additives and packing agents due to their antimicrobial properties, and in fungicides, anticancer drugs and clinical imaging reagents can lead to ingestion exposure (Rasmussen et al., 2010, He et al., 2011;). Absorbed ZnO NPs from the gastrointestinal tract enter the liver through the portal vein and may impact the liver since it is the primary organ of metabolism. Therefore, hepatotoxicity is one of the major emerging issues concerning potential hazards of ZnO NPs (Yang et al., 2015).

Liver damage induced by ZnO NPs, was investigated by serum biomarkers such as ASAT, ALAT, creatinine, uric acid and total protein levels. Blood creatinine (Fig. 2A) and ASAT (Fig. 2E) activities were higher in rats administered with 0.5 and 1g /kg of ZnO NPs compared to untreated group. Whereas uric acid (Fig. 2B) and total proteins concentrations (Fig. 2C) were lower.

Thus, the increased serum levels of ASAT activity constitutes a sign of hepatocyte damage, while raised blood creatinine and decreased total proteins concentrations are biomarkers of possible kidney injury. The decrease of blood uric acid content could be a biomarker of an oxidative stress status.

In our study, oral administration of ZnO NPs to rats leads to liver injury that was reflected by increased ASAT in the serum starting 24h after ZnO NPs injection and returns to normal by the 7^{th} day post treatment. In the contrary, there were no significant changes in ALAT activity (Fig. 2D) compared to sham group.

Previous data of Wang et al., (2006) on the acute toxicity of nano- and micro-scale zinc powder in healthy adult mice indicated more liver pathological lesions in nano group than micro group. Moreover, Wang et al., (2007) in a study on the acute toxicity and biodistribution of different sized titanium dioxide (TiO2) particles in mice after oral administration, have noticed that hepatic damage is more pronounced with smaller particles.

ZnO NPs-induced liver injury was further confirmed by histopathological examination, which showed edematous rearrangements and intra-portal inflammatory infiltrations and congestive dilation of central veins. These early histopathological changes induced later (after 15 days of ZnO NPs exposure) necrosis cell death.

4.Conclusion:

Based on the results of histopathological and biochemical findings, a preliminary conclusion could be drawn that oral administration of ZnO NPs induced liver damage in a dose-dependent manner and this effect varied also with treatment duration.

References:

Aschberger ,K., Micheletti,C., Sokull-Klüttgen,B., Frans M. Christensen,F.M. (2011) Analysis of currently available data for characterising the risk of engineered nanomaterials to the environment and human health — Lessons learned from four case studies, *Environ. Int*, 37, 1143–1156.

Brayner, R., Ferrari-Iliou, R., Brivois, N., Djediat, S., Benedetti, M.F., Fiévet, F., 2006. Toxicological impact studies based on Escherichia coli bacteria in ultrafine ZnO nanoparticles colloidal medium. Nano Lett. 6 (4), 866–870.

Ferreira, A.J., Celyn-Jones, J., Robalo-Cordeiro, C. (2013) Nanoparticles, nanotechnology and pulmonary nanotoxicology . *Rev. Port. Pneumol*, 19, 27-38.

Hasabo, G., Elbasiouny, M., AbdelSalam, M. , Ghaleb, S. , Eldessouky, N.,2015. Acute Hepatotoxicity of Nano- and Micro-sized Iron Particles in Adult Albino Rats; Histopathological changes. Journal of PharmaSciTech .4(2).

He, L., Liu, Y., Mustapha, A., Lin, M., 2011. Antifungal activity of zinc oxide 565 nanoparticles against Botrytis cinerea and Penicillium expansum. Microbiol. 566 Res. 166, 207–215

Heng, B.C., Zhao, X., Xiong, S., Ng, K.W., Boey, F.Y., Loo, J.S., 2010. Toxicity of zinc oxide (ZnO) nanoparticles on human bronchial epithelial cells (BEAS-2B) is accentuated by oxidative stress. Food Chem. Toxicol. 48 (6), 1762–1766.

Hoyt, V.W., Mason, E., 2008. Nanotechnology: emerging health issues. J. Chem. Health Saf. 15, 10–15

Kao, Y.Y., Chen, Y.C., Cheng, T.J., Chiung, Y.M., Liu, P.S., 2012. Zinc oxide nanoparticles interfere with zinc ion homeostasis to cause cytotoxicity. Toxicol. Sci. 125 (2), 462–472.

Kumar, A., Pandey, A.K., Singh, S.S., Shanker, R., Dhawan, A., 2011. Engineered ZnO and TiO(2) nanoparticles induce oxidative stress and DNA damage leading to reduced viability of Escherichia coli. Free Radic. Biol. Med. 51 (10), 1872–1881.

Li, C.H., Shen, C.C., Cheng, Y.W., Huang, S.H., Wu, C.C., Kao, C.C., Liao, J.W., Kang, J.J., 2011. Organ biodistribution, clearance, and genotoxicity of orally administered zinc oxide nanoparticles in mice. Nanotoxicology.

Meyer, K., Rajanahalli, P., Ahamed, M., Rowe, J.J., Hong, Y., 2011. ZnO nanoparticles induce apoptosis in human dermal fibroblasts via p53 and p38 pathways. Toxicol. in Vitro 25 (8), 1721–1726.

oxide nanoparticles. Mutat. Res. 745 (1–2), 84–91.

Rasmussen, J.W., Martinez, E., Louka, P., Wingett, D.G., 2010. Zinc oxide 612 nanoparticles for selective destruction of tumor cells and potential for drug 613 delivery applications. Expert Opin. Drug Deliv. 7, 1063–1077.

Sharma, V., Anderson, D., Dhawan, A., 2011. Zinc oxide nanoparticles induce oxidative stress and genotoxicity in human liver cells (HepG2). J. Biomed. Nanotechnol. 7 (1), 98–99.

Sharma, V., Singh, P., Pandey, A.K., Dhawan, A., 2012. Induction of oxidative stress, DNA damage and apoptosis in mouse liver after sub-acute oral exposure to zinc

Wang, B., Feng, W., Wang, M., Wang, T., Gu, Y., Zhu, M., M., Ouyang, H., Shi, J., Zhang, F., Zhao, Y., Chai, Z., Wang, H., Jing Wang,J.,2008. Acute toxicological impact of nano- and submicro-scaled zinc oxide powder on healthy adult mice. J Nanopart Res.10:263–276.

Wang, B., Feng, W.Y., 2007.particles in mice after oral administration. Toxicology Letters 2007; 168:176–185.

Wang, B., Feng, W.Y., Wang, T.C., Jia, G., Wang, M., Shi, J.W., Zhang, F., Zhao, Y.L., Chai, Z.F., (2006). Acute toxicity of nano- and micro-scale zinc powder in healthy adult mice. Toxicol Lett.161(2):115–123.

Wang, H., Xie, C., Zhang, W., Cai, S., Yang, Z., Gui, Y., 2007. Comparison of dye degradation efficiency using ZnO powders with various size scales. J. Hazard. Mater. 141 (3), 645–652.

Xu, F., Zhang, P., Navrotsky, A., Yuan, Z.Y., Ren, T.Z., Halasa, M., Su, B.L., 2007. Hierarchically assembled porous ZnO nanoparticles: synthesis, surface energy, and photocatalytic activity. Chem. Mater. 19 (23), 5680–5686.

Yang, X. , Shao, H., Weirong Liu, W., Weizhong Gu, W., Xiaoli Shu, X., Yiqun Mo, Y, Chen, X., Zhang, Q., Mizu Jiang, M., 2015. Endoplasmic reticulum stress and oxidative stress are involved in ZnO 2 nanoparticle-induced hepatotoxicity. Toxicology Letters.

Laser-assisted photocatalysed degradation of pollutants using solid oxide in electronic contact with gold nanoparticles

Z. Chehadi [1,2], J. Toufaily [2], J-S. Girardon [3], M. Capron [3], F. Dumeignil [3], T. Hamieh [2], R. Bachelot [1], S. Jradi [1].

[1]Laboratoire de Nanotechnologie et d'Instrumentation Optique, Institut Charles Delaunay, STMR-UMR 6281 CNRS, Université de Technologie de Troyes, 12 rue Marie Curie - CS 42060, 10004 Troyes Cedex - France. 2 Laboratory of Materials, Catalysis, Environment and Analytical Methods, Faculty of Sciences I, Doctorate School of Science and Technology, Lebanese University, Beirut, Lebanon.
[3] Université Lille Nord de France, F-59000, Lille, France; CNRS UMR8181, Unité de Catalyse et Chimie du Solide, UCCS, F-59655 Villeneuve d'Ascq, France.

Abstract: In this work we investigate the coupling between Plasmonic gold nanostructures and catalyst supports such as TiO_2, ZnO and Al_2O_3 in order to study the photocatalytic degradation of Bisphenol A (BPA) under visible laser excitation. The experimental investigations have shown extremely fast and complete photodegradation of organic pollutants in water. The influence of photocatalyst band gap on the catalytic activity was investigated as well. Au/TiO_2 catalyst showed the fastest degradation of BPA due to efficient electron transfer from excited noble metal Gold nanoparticles to the semiconductor.

Introduction:

Bisphenol A (BPA) is used as a monomer and additive in the production of polycarbonate plastics such as baby bottles and as epoxy resin. It causes a strong estrogenic endocrine disrupting effect and cancer and has an acute toxicity in the range of ~1-10 mg L^{-1} for a number of fresh water and marine species [(3)]. Thus development of methods for the removal of BPA is still a big challenge. In this context, advanced oxidation processes (AOPs) have been proposed for the elimination of many toxic organic compounds in waste water, air and soil; such as (O_3/H_2O_2, UV/O_3, UV/H_2O_2, H_2O_2/Fe^{2+}, and UV/TiO_2). More particularly, the photocatalytic process using a semiconductor as PhotoCatalyst (PC) under UV irradiation is currently applied for the oxidation of various organic compounds [(5)]. However, the fast recombination of the photogenerated electron hole (e^-/h^+) and the wide band gap of semiconductors which limit absorption to the UV range, reduce their efficiency as PC[(1)]. Various solutions have been reported and shown the possibility to increase the efficiency of semiconductor photocatalysis such as coupling them with noble metals or doping them with nitrogen [(5)]. In that context, Gold Nanoparticles (GNPs) in electronic contact with TiO_2 have shown the possibility to use this later as efficient PC in the visible range [(2)]. In this study, the efficient photodegradation of BPA under visible light was demonstrated. The influence of various parameters such as irradiation time, laser power, and catalyst type has been investigated. Four materials (Au/TiO_2, Au/Al_2O_3, Au/ZnO and TiO_2) were investigated as PCs for the degradation of BPA under 2.2 W of 532-nm laser.

Experimental:

Gold nanoparticles on TiO_2, ZnO an Al_2O_3 extrudates (wt GNPS/wt TiO_2=1%) were purchased from strem chemical. The photocatalytic activity of Au/TiO_2, Au/ZnO and Au/Al_2O_3 was investigated using 2.5 ml of BPA 0.1mM in a quartz cuvette under visible irradiation. A laser emitting at 532 nm was used as a visible source. During the irradiation, the solution of BPA was magnetically stirred. The absorbance of BPA was measured by UV-visible spectrometry before and after irradiation for studying the reaction kinetics.

Results and discussion:

The experimental results shown in Figure 1-A revealed that there is no conversion of BPA in the presence of TiO_2. Additionally, the conversion rate is almost negligible with Au/Al_2O_3 (less than 5% after 30 min). In the opposite, 92% of BPA was eliminated after 12 min in the presence of Au/TiO_2. Au/ZnO shows also catalytic activity (~ 50% of conversion after 30 min) but seems to be less efficient than Au/TiO_2 (100% of conversion after 20 min). It appears from this first result that the photodegradation reaction is related to the presence of GNPs at the surface of both TiO_2 and Au/ZnO which are semiconductors with band gaps of 3.2 and 3.37 eV respectively. The catalytic activity under visible light could be attributed to electrons generated during excitation of the Localized Surface Plasmon Resonance (LSPR) which could be transferred to the Conduction Band (CB) of the semiconductor. Indeed, during laser excitation of GNPs, electrons are very dynamic in a high energy level that is higher than the CB of TiO_2 and this of ZnO. The electrons transferred in this way are used for the generation of $OH^{\bullet}$ radicals from water and dissolved oxygen at the surface of TiO_2. $OH^{\bullet}$ are highly reactive species and responsible for the degradation of pollutants.

The absence of catalytic activity of TiO_2 under 532 nm laser is simply related to fact that is not absorbing visible light. However, even though GNPs absorb visible photons, Au/Al_2O_3 does not show any photocatalytic activity, which could be explained by its high energy gap (> 6.5 eV) making it difficult the electron transfer from GNPs.

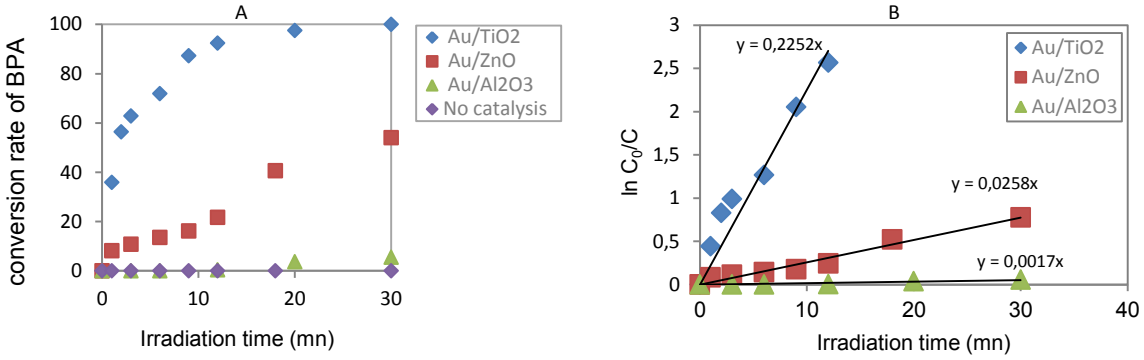

Figure 1: A: the conversion rate of BPA as a function of irradiation time. B: Kinetics of the degradation reaction of BPA.

The kinetic of photocatalytic degradation of BPA in the presence of Au/TiO_2, Au/ZnO and Au/Al_2O_3 has shown to follow a first order kinetic reaction where $\ln C_0/C$ varies linearly with time (Figure 1-B). The constant rate of reaction (K in min^{-1}) for Au/Al_2O_3, Au/ZnO and Au/TiO_2 is 0.0017, 0.0258 and 0.2252 respectively (figure 1-B). Indeed, this result shows clearly faster degradation reaction in the presence of Au/TiO_2. This behavior is due to efficient electron transfer promoted by the highest difference of energy gap between excited electrons of GNPs and CB of TiO_2.

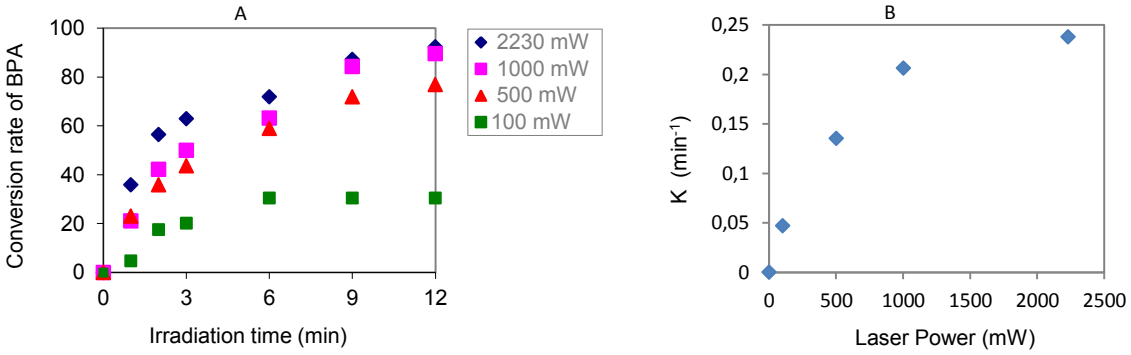

Figure 2**:** A: The conversion of BPA using different laser powers. B: The variation of the reaction rate constant K (min^{-1}) as a function of laser power.

Figure 2 shows the influence of Laser Power (LP) on the catalytic activity of Au/TiO_2. From Figure 2-A, it appears that the conversion rate at a given time is increasing with incident energy, in relation with higher number of transferred electrons. However, the variation of K with LP (Figure –B) seems to reach a plateau after 1000 mW where conversion rate of BPA after 9 min is almost the same, even for 2000 mW. This saturation of K could be attributed to a limited number of transferred electrons in relation with small amount of Gold which is 1 % weight from TiO_2 weight.

Conclusion:

Efficient photocatalytic degradation of BPA under visible light irradiation was demonstrated. The influence of catalyst type was investigated. It turns out that Au/TiO_2 allows the most efficient degradation reaction where almost 100% of BPA is eliminated after 12 min. This result is attributed to efficient electron transfer between excited electrons of GNPs and CB of TiO_2.

References:

(1) Saji Thomas Kochuveedu, et al., (2013) A Study for the interaction of ligh with noble –metal oxide semiconductor nanostructures for various photophysical applications, RSC publishing, Chem soc Rev.

(2) Matthew E. Stewart, et al., (2008) Nanostructured plasmonic sensors, Chem. Rev, 108, 494.

(3) Changsheng Guo, et al., (2010) Direct synthesis of Mesoporous TiO_2 Microspheres: Catalysts and their photocatalyis for Bisphenol A Degradation, Environ. Sci. Technol, 44, 419–425.

(4) Parvaneh Sangpour, et al., (2010) Photoenhanced Degradation of Methylene Blue on Cosputtered M: TiO2 (M) Au, Ag, Cu), J. Phys. Chem..C, 114, 13955–13961.

(5) Miguel Pelaeza, et al., (2012) A review on the visible light active titanium dioxide photocatalysts for environmental applications, Applied Catalysis B: Environmental, 125, 331-349.

Synthesis and characterization of iron oxide nanoparticles

Maïssa DARDOURI[a], João BORGES[b], Amel DAKHLAOUI OMRANI[a*]

a) Laboratory of Physical Chemistry of Mineral Materials and their Applications, National Center of Research in Material Sciences, CNRSM, Technologic Park of Borj-Cedria B.P. 73, 8020 Soliman, Tunisia
b) CENIMAT/I3N, Departamento de Ciência dos Materiais, Faculdade de Ciências e Tecnologia, FCT, Universidade Nova de Lisboa, Portugal

ABSTRACT

Magnetic iron oxide nanoparticles (NPs) were elaborated according to a simple hydrothermal approach at 160°C using water as solvent. The structure and the microstructure of the as-elaborated products were investigated by X-ray diffraction (XRD), scanning electron microscopy (SEM) and transmission electron microscopy (TEM). The XRD technique confirmed the formation of magnetite Fe_3O_4 nanostructures with high purity and good crystallinity. Their SEM and TEM micrographs show NPs with various sizes and morphologies (spherical and hexagonal prisms) depending on the synthesis conditions.

***Keywords**: Magnetic Iron oxide nanoparticles, magnetite, hydrothermal method,*

INTRODUCTION

For the past three decades, iron oxide nanoparticles (NPs), especially magnetite Fe_3O_4 and maghemite γFe_2O_3, have been established as a promising platform because of their numerous biomedical applications such as, targeted drug delivery, hyperthermia, magnetic scaffolds for bone defect repair, magnetic resonance imaging (MRI),…**[1-3]**. Many of these applications are directly related to the biocompatibility and the magnetic properties of these NPs. However, these latest properties highly depend on the structure and the microstructure (surface quality, the shape and the size, etc.) of the elaborated NPs which were influenced by the synthesis conditions.

This paper, reports on the synthesis of magnetite Fe_3O_4 NPs with various sizes and morphologies using eco-friendly combined co-precipitation and hydrothermal approaches. The effect of synthesis conditions on the size and the morphology of the as-elaborated NPs were investigated. The X-Ray Diffraction (XRD) permits to confirm the purity and the good crystallinity of the as-elaborated powders identified as pure magnetite (Fe_3O_4) nanostructures. The electron

[*]Corresponding author phone: +21699404772/+216; fax: +21679325314
e-mail: dakhlaoui_amel@yahoo.fr; amelomrani73@gmail.com

microscopes (SEM and TEM) of these magnetic NPs allow to confirm the effect of the synthesis process on the microstructure of the as-elaborated powders.

2. EXPERIMENTAL DETAILS

2.1 Synthesis of iron oxide nanoparticles

Iron oxide NPs were prepared according to the following process: 9.37 mmol of Ferric chloride hexahydrate ($FeCl_3.6H_2O$, 97%) and 9.37 mmol of Ferrous sulfate heptahydrate ($FeSO_4.7H_2O$, ≥99%) were firstly dissolved in ultra-pure water. Thereafter, different amounts of NaOH were added to this solution under magnetic stirring at room temperature. The color of the solution moves from dark orange to black after few minutes, indicating the co-precipitation of Fe_3O_4 NPs. The black precipitate was then transferred into a Teflon-lined stainless steel autoclave to be heated at 160°C. After cooling to room temperature the resultant black precipitate was isolated by applying a permanent magnet (Fig.1). This procedure was repeated four to five times to remove excess ions and sodium chloride salt in the suspension. Finally the precipitate was dried in an oven at 50°C for 3h.

Figure 1: magnetic separation of the black precipitate

2.2 Characterization

The as-synthesized products were characterized using different techniques. Their crystal structure was obtained by X-ray diffraction employing a « PanalyticalX'Pert PRO MPD» diffractometer equipped with a copper anticathode ($\lambda_{Cuk\alpha}$= 1.5418 Å). The average crystallites size was calculated using the Scherrer's relation $L = \frac{0.9\lambda}{\beta \cos\theta}$, where: λ is the wavelength of the X-ray radiation, θ is the Bragg angle of the corresponding peak, $\beta = \sqrt{\beta_M^2 - \beta_S^2}$ is the full width at half-height (FWHM) of the sample, β_M, corrected for the instrumental broadening, β_S, inferred from the standard Si sample.

SEM observations were carried out using a Carl Zeiss AURIGA Cross Beam (FIB-SEM) workstation instrument. A carbon support was used as a conductive substrate, upon which the samples' powders were deposited.

High-resolution transmission electron microscopic (HRTEM) observations were carried out on a Hitachi H-8100 II with thermionic emission LaB6. A diluted suspension was placed in a Kevlar 25 mesh grid for analysis.

3. RESULTS AND DISCUSSION

Several synthesis parameters such as the basic ratio ($b= n_{OH^-}/(n_{Fe^{2+}}+n_{Fe^{3+}})$), the duration of the hydrothermal treatment and the precursor's mixing process have been varied in this study resulting in particles with different microstructural characteristics (table 1).

Figure2 reports the XRD patterns of the as-elaborated powders. All diffractograms show six peaks characteristic of well-crystallized and pure magnetite (Fe_3O_4) with inverse spinel structure (space group (Fd-3m); JCPDS file, No 01-089-3854, 01-088-0315, 01-075-0033). The crystallite sizes, estimated from the FWHM of the (311) diffraction peak show an increase of the crystal size as the alkaline ratio increases (samples $MFe_{1, 2, 3}$) (table 1) probably related to the increases of the pH of the aqueous solution which is in good agreement with results reported by *M. Mahdavi et al* **[2]**. Furthermore, the crystallite size increases by extending the duration of the hydrothermal treatment: The XRD pattern of the black precipitate obtained before hydrothermal treatment corresponds to pure Fe_3O_4 (Fig. 2d). The diffraction peaks are too large confirming the small size of crystallites (12.2 nm) constituting its particles. Furthermore, the crystallite size increases considerably when extending the duration of the hydrothermal treatment of this black precipitate (Table 1). This confirms that the particle's growth occurs here via an aggregation process rather than Ostwald ripening one.

Table 1: The most attractive results obtained as a function of the alkaline ratio and duration of hydrothermal treatment.

Samples	alkaline ratio (b)	Duration of the hydrothermal treatment	Crystallite size d_{XRD} (nm)
MFe_1	2.46	1	21.7
MFe_2	2.76	1	24.4
MFe_3	3	1	65.2
MFe_4	2.76	0	12.16
MFe_5	2.76	12	32.6
MFe_6	2.76	30	78

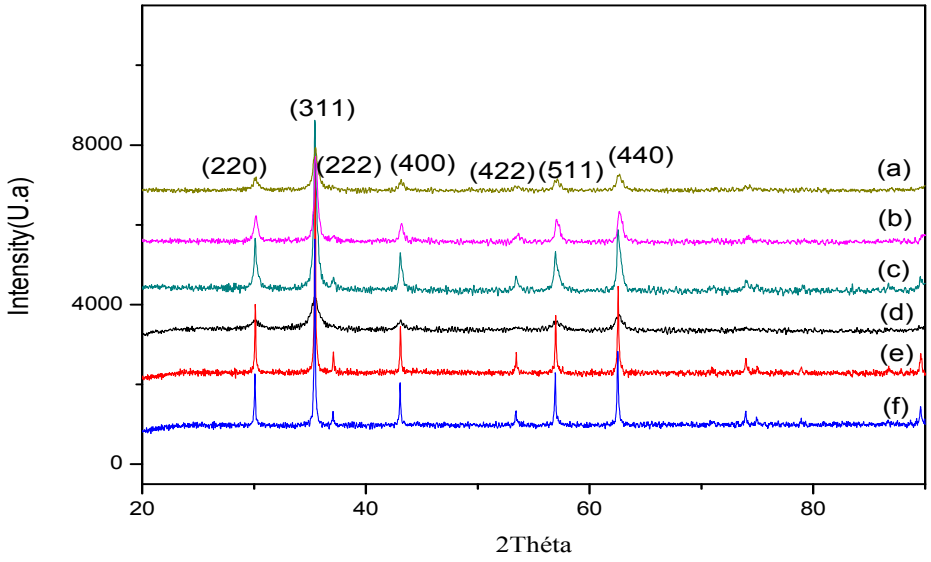

Figure 2: XRD patterns of iron oxide nanoparticles synthesized at different alkaline ratios (a) MFe_1, (b) MFe_2, (c) MFe_3 and different duration of the hydrothermal Treatment (d) MFe_4,(e) MFe_5, (f) MFe_6

The TEM micrograph of the sample MFe_2 obtained at an alkaline ratio of 2.76 shows spherical nanoparticles with diameter in the range 22 - 40 nm (Fig.3a). The particles'size is larger than the crystallites size calculated on the basis of the XRD pattern which further implied that one particle is constituted of several crystallites. Thus, most particles are polydomain and their growth occurred via an aggregation process of initial crystallites which strongly support our previous hypothesis.

When changing the adding process of NaOH to the ferrous precursor solution, NaOH is now added as aqueous solution not as pellet, a drastic change in the particles' morphology from spherical (sample MFe_2) to hexagonal prismatic, for the sample MFe_7 (Fig.3b), was observed. Moreover, the NPs of the sample MFe_7 are not monodisperse and their diameter's range from 10 to 70 nm. The effect of the precursor mixing process on the structural and microstructural characteristic of the elaborated NPs will be further investigated in our future studies.

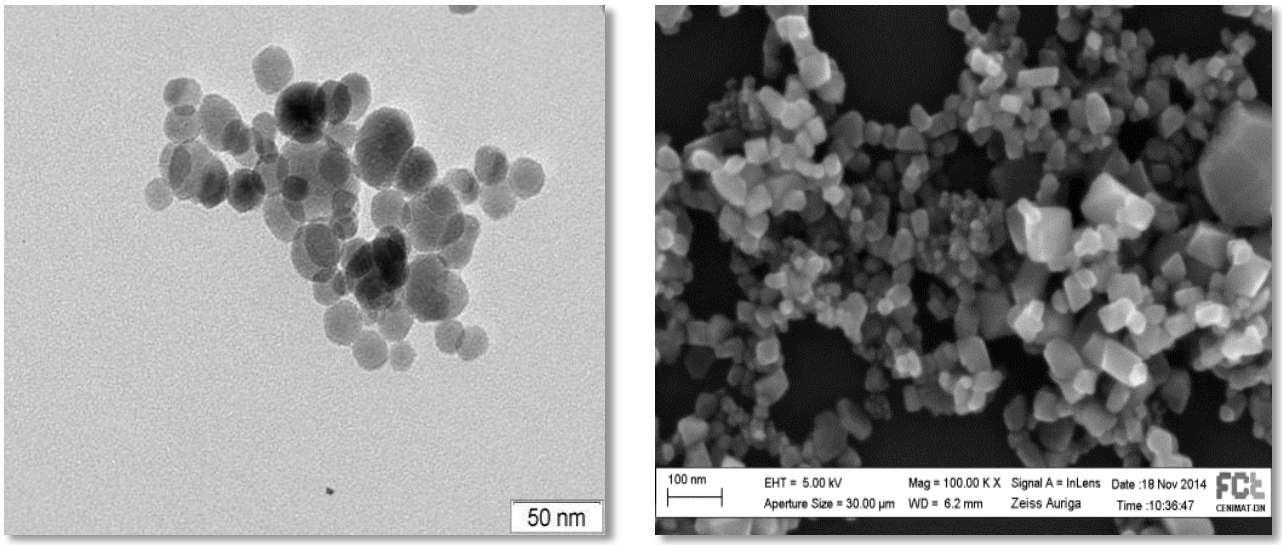

(a) (b)

Figure 3: a) TEM micrograph of the sample MFe_4 and b) SEM micrograph of the sample MFe_7

Acknowledgments:

We greatly appreciate the financial support from the Ministry of Higher Education and Scientific Research of Tunisia.

This work was partly funded by FEDER funds through the COMPETE 2020 Programme and National Funds throught FCT - Portuguese Foundation for Science and Technology under the project UID/CTM/50025/2013.

REFERENCES

[1] Ch. Chen, X. Jiang, Y. V. Kaneti, A.Yu, *Powder Technology*, 236, (2013), pp. 157–163.
[2] M. Mahdavi, M. Bin Ahmad, M. J. Haron, F. Namvar, B. Nadi, M. Z. AbRahman, J. Amin, *Molecules*, 18, (2013)**,** pp. 7533-7548.
[3] N. Bock, A. Riminucci, C. Dionigi, A. Russo, A. Tampieri, E. Landi, V.A. Goranov, M. Marcacci, V. Dediu, *ActaBiomaterialia 6,* (2010), pp.786–796.
[4] Ph .H. Tran, Th.T.Tran, T.V. Vo, B.J. Lee, *ArchPharm Res,* 35, 12, (2012), pp. 2045-2061.

Multi-Walled Carbon Nanotubes-incorporated Biopolymers as Extraction Tools for Selected Drugs in Aqueous Matrices

Mohd Marsin Sanagi[1,2 *], Wan Nazihah Wan Ibrahim[1,3], Nor Suhaila Mohamad Hanapi[1,3], Wan Aini Wan Ibrahim[1]

[1]Department of Chemistry, Faculty of Science, Universiti Teknologi Malaysia, 81310 Johor Bahru, Johor, Malaysia

[2]Ibnu Sina Institute for Scientific and Industrial Research, Universiti Teknologi Malaysia, 81310 Johor Bahru, Johor, Malaysia

[3]Faculty of Applied Science, Universiti Teknologi MARA, 40450 Shah Alam, Selangor, Malaysia

marsin@kimia.fs.utm.my

ABSTRACT

This work investigates the use of biopolymer adsorbents of blended agarose/chitosan incorporated with multi-walled carbon nanotubes (Agr-Ch-MWCNT) as micro-solid phase extraction tool for the determination non-steroidal anti-inflammatory drugs (NSAIDs) in aqueous matrices. The Agr-Ch-MWCNT adsorbent demonstrated high affinity for NSAIDs in tap water, well water and river water with excellent relative recoveries and good reproducibility.

Keywords: biopolymers blended, incorporation of MWCNTs, NSAIDs and adsorption.

1. INTRODUCTION

Rapid industrialization increased the environmental pollution, impacting adversely upon the living organism. These include the pharmaceutical residue where they are found in effluents of conventional sewage treatment plants (STPs) as well as in surface water, ground water and drinking water [1]. Non-steroidal anti-inflammatory drugs (NSAIDs) is one of the most consumed pharmaceuticals that are frequently used in human and veterinary medicine for suppressing inflammatory process, treating allergies and reducing pain without side effects of sedation, respiratory depression or addiction. Due to their hydrophilicity and stability in water, NSAIDs can be retained in the aqueous phase for a very long time [2].

Microextraction has been known as a new emerging technique towards simplification, miniaturization and minimization of organic solvents and materials used in sample preparation [3]. Adsorption methods are the most preferable and widely employed in the isolation and preconcentration of analytes in environmental samples. These include silica-based sorbents [4], synthetic polymer [5], nanofibers [6] and carbon nanotubes [7]. Each of them possesses great physical and chemical properties that give advantages in adsorbent-adsorbate interactions but high production cost and non-biodegradable materials raised the industrial issue.

Biopolymers such as chitosan and agarose are promising materials to overcome these drawbacks. Chitosan is endowed with high content of primary amino groups for an excellent adsorption capacity but is pH-sensitive [7]. Meanwhile agarose offers molecular flexibility with high pH-resistance but lack of native ligands [9]. Therefore, blending of biopolymers is a simple, convenient and effective method to improve their chemical properties and mechanical strength rather than tedious and complex procedure of chemical modifications [10].

Multi-walled carbon nanotubes (MWCNTs) are polymers of pure carbon with multiple layers in tubular shape. Incorporation of highly interconnected pores of the MWCNTs in the biopolymer matrix is expected to contribute to the increase in the hydrophobic sites, surface area and porosity of the materials and thus enhancing the extraction efficiency [11].

2. EXPERIMENTAL

2.1 Composite Film Microextraction (CFME)

Preparation of Agr-Ch-MWCNT composite film is based on previous work in our laboratory [12] with some modifications.

Composite film microextractions of NSAIDs were carried out as described by Loh, *et al.*, 2013 [13]. HPLC separations were carried out on a Zorbax Eclipes Plus C_{18} column (3.5 μm × 2.1 mm I.D. × 100 mm) and analytes were detected at wavelength of 230 nm and recorded on a Powerchrom data recording system (eDAQ, Australia). The eluent was acetonitrile-acetate buffer (pH 3.2; 25 mM) (60:40) (v/v) at flow rate 0.2 mL/min.

3. RESULTS AND DISCUSSION

3.1. Characterization of Agr-Ch-MWCNT

The composite film of Agr-Ch-MWCNT obtained was in black in color and it possessed a rough surface. The FESEM micrograph of Agr-Ch-MWCNT (Fig. 1) shows MWCNT obtained high compatibility within the matrix of Agr-Ch film with no sign of aggregation [14]. This corresponds to very good dispersion and adhesion of MWCNT in the matrix. The specific surface area from BET analysis was found to be 40.258 m^2/g indicating that the incorporation of MWCNT in composite film contributed to larger surface area

compared to origin polysaccharides [6]. A cumulative pore volume is 0.0415 cm^3/g while total pore area is 4.050 m^2/g.

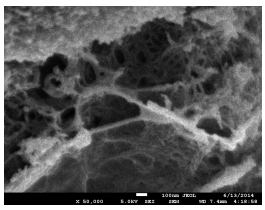

Fig. 1: Cross section micrograph of Agr-Ch-MWCNT

3.2. Optimization of CFME Performance

The addition of salt leads to a higher ionic strength and decrease the solubility of NSAIDs analytes in aqueous samples. As shown in Fig. 2a, the extraction efficiency of analytes increased until an optimum condition was achieved at 2% (w/v). Further addition of salt resulted in decreasing efficiency. This might be due to electrostatic interaction between the adsorbents and salt in the solution [5].

Most of the NSAIDs have low pK_a values where they mostly exist in neutral forms at low pH and protonated at higher pH. Therefore, sample pH was expected to influence efficiency of extraction. In this work, extraction recovery significantly improved when sample pH was increased from 1 to 2. These might be attributed to the considerable hydrophobic interactions of MWCNTs in the composite film and also the blended Agr-Ch that existed in protonated forms that contributed to ionic interactions towards analytes [15].

In order to investigate the effect of adsorbent loading amount (% w/v) on actual extraction performance, different MWCNT concentrations in the range 0 - 0.5 % w/v were applied on the Agr-Ch film. Fig. 2b shows that the extraction recovery of NSAIDs was <10% when only Agr-Ch film was used as extraction medium. However, the extraction performance increased proportionally with incorporation of MWCNT from 0 to 0.4% w/v. It showed that hydrophobic and π-π interactions between MWCNT and analytes were more dominant than ionic interactions within Agr-Ch film under pH 2 conditions.

(a)

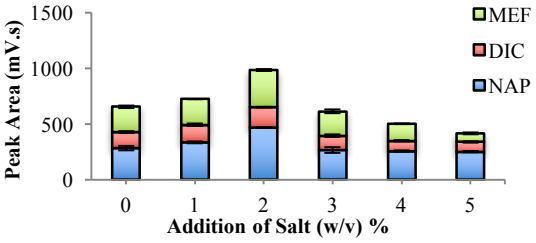

(b)

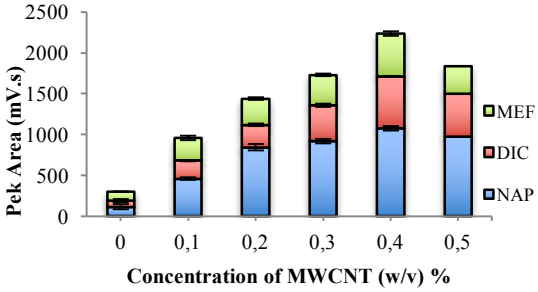

Fig. 2: (a) salting out effect on extraction of NSAIDs from aqueous samples. (b) effect of concentration of MWCNT on extraction of NSAIDs from aqueous samples.

3.3 Validation Data of CFME of NSAIDs from Spiked Tap Water, River Water and Well Water

Experiments were carried out to validate the applicability of the CFME technique under the optimized conditions. Calibration curves were plotted using least-squares methods plotting the peak area as response versus concentration. It was found that the calibration curve were linear in the range of 1-200 µg/L (NAP) and 10-500 µg/L (DIC and MEF) for the water samples. Good linearity (Table 1) was obtained in the specific concentration ranges. The limits of detection were in the range of 0.89-8.05 µg/L. Relative recovery studies showed excellent relative recoveries in the range of 94.30 - 109.74% and good reproducibility with relative standard deviations (RSDs) of < 5.16%.

4. CONCLUSION

Biopolymers adsorbents with multi-walled carbon nanotube reinforced blended agarose/chitosan composite film (Agr-Ch-MWCNT) has been successfully prepared. Incorporation of MWCNT increased the surface area and offer additional active sites for adsorbent-adsorbate interactions. The efficiency of synthesized biopolymer adsorbent has been evaluated in composite film microextraction (CFME) of selected NSAIDs with HPLC-UV detection. The proposed method showed low LODs value and excellent relative recoveries and provided rapid, simple step extraction and also reduction in organic solvent consumption.

Table 1: Validation data of CFME of NSAIDs from spiked tap water, well water and river water samples

Sample	Analyte	Linearity range, µg/L	r^2	LOD, µg/L
Tap water	NAP	1-200	0.9981	0.89
	DIC	10-500	0.9995	7.62
	MEF	10-500	0.9994	7.64
Well water	NAP	1-200	0.9988	0.89
	DIC	10-500	0.9973	4.89
	MEF	10-500	0.9983	7.12
River water	NAP	1-200	0.9991	0.97
	DIC	10-500	0.9977	6.15
	MEF	10-500	0.9982	8.05

ACKNOWLEDGMENT

Thanks to Universiti Teknologi Malaysia for facilitations and the Ministry of Science, Technology and Innovation (MOSTI) for financial supports through Research Grant Vote No. [R.J130000.7909.4S069] and for studentship for Wan Nazihah Wan Ibrahim.

REFERENCES

1. Saleh, A., Larsson, E., Yamini, Y. and Jönsson, J. Å. (2011). J. Chromatogr. A. 1218, 1331-1339.
2. Lin, A.Y-C., Yu, T-H. and Lateef, S. K. (2009) J. Haz. Mater. 167, 1163-1169.
3. Vas, G. and Vékey, K. (2004). J. Mass Spec. 39, 233-254.
4. Jiménez, J. J. (2013). Talanta. 116, 678-687.
5. Silva, A.R.M., Portugal, F.C.M. and Noguirea, J.F.M. (2008). J. Chromatogr. A. 1209, 10-16.
6. Lewitus, D.Y., Landers, J., Branch, J., Smith, K.L., Callegari, G., Kohn, J. and Neimark, A.V. (2011). Adv. Func. Materials. 21(14), 2624-2632.
7. Dahane, S., Gil García, M.D., Martínez Bueno, M.J., Uclés Moreno, A., Martínez Galera, M. and Derdour, A. (2013). J. Chromatogr. A. 1297, 17-28.
8. Sharififard, H., Ashtiani, F.Z. and Soleimani, M. (2013) J. Chem. Eng. 8,84-395.
9. Firouzabadi, H., Iranpoor, N., Kazemi, F. and Gholinejad, M. (2012) J. Mol. Catal. A: Chem., 357, 154-161.
10. Nitayaphat, W. (2014) Chiang Mai J. Sci., 41(1), 174-183.
11. Olivas-Armendariz, I., Martel-Estrada, S.A., Mendoza-Duarte, M.E., Jiménez-Vega, F., García-Casillas, P., Martínez-Pérez, C.A. (2013) J. Biomat. Nanobiotech. 4, 204-211
12. El-Hefian, E.A., Nasef, M.M., and Yahaya, A.H. (2012) E-J. Chem. 9(3), 1431-1439.
13. Loh, S. H., Sanagi, M. M., Wan Ibrahim, W. A., and Hassan, M. N. (2013) Talanta. 105, 200-205.
14. Mustafa, A., Kusworo, T.D., Busairi, A., Ismail, A.F., Budiyono. (2012) Int. J. of Waste Res. 2(1), 22-24.
15. Wu, C.S. (2005) Polymer. 46, 147-155.
16. See, H.H., Sanagi, M.M, Wan Ibrahim, W.A., Naim, A.A. (2010) J. Chromatogr. A. 1217, 1767-1772.

Temperature and cross-linking degree effects on the swelling of poly(acrylamide/1,6-hexanedioldiacrylate):Optimization by central composite designs

S Hamri [1,2], D Lerari [1], B Dali Youcef [2], T Bouchaour [2] and K Bachari [1]

[1]Research Center in Analytical Chemistry and Physics (CRAPC), Tipaza, Algeria.
[2]Research Laboratory on Macromolecules (LRM), deppartemnt of physics, University of Abou Bekr Belkaid, Tlemcen, Algeria.
E-mail: salah_hamri@yahoo.fr

Abstract. The aim of this study was to apply central composite design (CCD) to model the effects of temperature (X1) and degree of cross-linking (X2) on the equilibrium swelling ratio (Y) of polyacrylamide hydrogel. Samples were prepared photo-chemically using a system composed of eosin/triethanolamine as photo-initiator and 1,6-hexanedioldiacrylate (HDDA) as crosslinker. The mathematical relationship of swelling ratio on the two factors can be approximated by a second-order quadratic model. Response surface modelling (RSM) was used to describe the individual and interactive effects of two variables at five levels. Predicted values were found to be in good agreement with experimental values. The model optimization prediction showed that the cross-linking degree has the higher effect and the swelling ratio presented the maximal result about 1290% at the optimal condition of 2% of cross-linker at 70°C.

1. Introduction

Polyacrylamide (PAM) is an atoxic, stable and high swell-ability in water. It commonly used as colon specific drug delivery devices and in wastewater treatment application [1,2]. Such materials are often prepared via a photopolymerization mechanism. Organic dyes are less toxic, less expensive and can be used for dye sensitization process [3]. Several organic dyes such as eosin Y, rose bengal and methylene blue [4,5] in the presence of electron donors such as tertiary amines, have been described as efficient photo-initiators for the free radical polymerization of acrylate monomers in aqueous solutions. [6–9] The tertiary amine is used as oxidizing species whereas the dye acts as reducing agent [10]. The swelling of this polymeric network is influenced by many parameters such as polymer composition, temperature and the nature of swelling media. The optimization of these parameters required high number of experiments. To reduce this number, thereby, save significant experimental time, material used for analysis and personal cost. Researchers are focused on using an experimental design that considered as efficient procedure for planning experiments so that the data obtained can be analyzed to yield valid and objective conclusions [11].

In this investigation, hydrophilic three-dimensional polymer network were elaborated made up of polyacrylamide. A photo-initiator system composed of eosin and triethanolamine in aqueous medium was applied for UV-radiation exposure. 1,6-Hexanedioldiacrylate (HDDA) was used as cross-linker. The central composite design (CCD) was used as an experimental strategy for seeking the optimum conditions for effect of temperature and degree of cross-linking on the equilibrium swelling ratio (ESR) of this polymeric material.

2. Experimental

2.1. Materials

Acrylamide (AM), (97%). Eosin (98%) (All products from Sigma-Aldrich) were used as received, without further purification.

2.2. Sample preparation

A reagent solution was prepared included acrylamide and eosin in aqueous medium, this solution was stirred for 24h.

2.3. Ultraviolet/Visible Spectroscopy

The absorption spectra of all solutions were obtained from a Varian Cary 100 UV visible double-beam spectrophotometer.

2.4. Real-Time Infrared spectroscopy

Uniform samples were prepared by casting the photo-curable formulation between a NaCl plate and a Polyethyleneterephthalate (PET) film. The samples, which were analyzed by infrared spectroscopy (Agilent Technologies Cary 600 Series FTIR Spectrometer, transmission mode, spectral resolution 4cm^{-1}), were simultaneously exposed to the visible light source mentioned above, at T=20°C. The spectrophotometer was provided with a Fourier transformed algorithm.

3. Central composite design approach (CCD)

Central composite design (CCD) was used to study the swelling behavior of the two factors towards one response. This method can reduce the number of experimental trials required to evaluate main effect of each parameter and their interactions. In general, CCD is characterized by three operations namely: 2n axial runs, 2^n factorial runs and n_c central runs as shown equation (1):

$$N = 2n + 2^n + n_c \qquad (1)$$

Where N is the total number of experiments required, n is the number of factors in the CCD [12]. The CCD in present research, with two factors, is composed of 11 experiments, reported in Table 1.

Table 1. CCD with 11 experiments.

Points	n=2
Factorial points 2^n	4
Star points 2n	4
Center points n_c (varies)	3
Total	11

Alpha (α) approximately shows the distance of the axial from center point, which is rotatable and strongly depends on the number of factorial points and can be calculated from following equation [13]:

$$\alpha\ (axial\ distance) = (2^n)^{\frac{1}{4}} \qquad (2)$$

In the present case n= 2 and α=1.414.
The factors in this experiment were degree of cross-linking (X_1) and temperature (X_2) represented on figure 1.

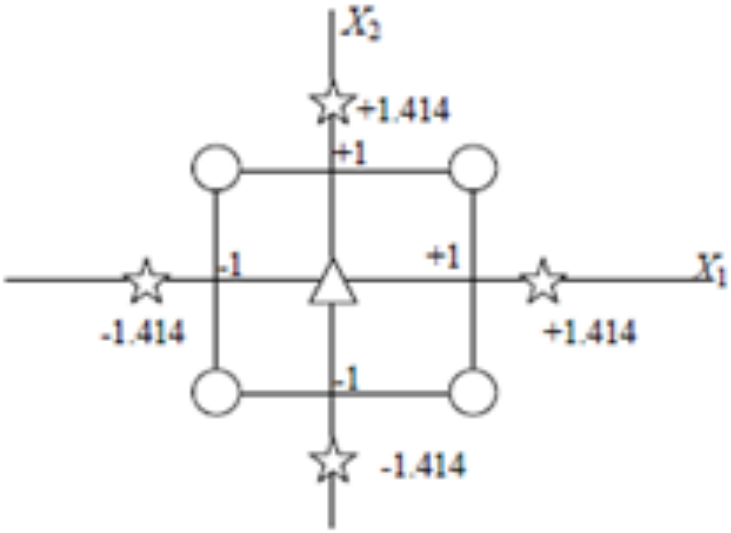

Figure 1. Central composite design for two factors X_1 and X_2.

The relation between the coded and the natural scales is given as follows:

$$U_i = X_i\left(\frac{U_{max} - U_{min}}{2}\right) + \left(\frac{U_{max} + U_{min}}{2}\right) \qquad (3)$$

Where U_i is a continuous quantitative factor and X_i is the coded value, U_{min} and U_{max} represent the limits of the factor as specified by the user [14].

A second-order polynomial Equation (4) that includes two squared terms, two linear terms and one interaction term was used to calculate the predicted response:

$$y = b_0 + b_1X_1 + b_2X_2 + b_{11}X_1^2 + b_{22}X_2^2 + b_{12}X_1X_2 \qquad (4)$$

Where y is swelling ratio, b_0 is the average of the results of the replicated center point; b_1 and b_2 are the main half-effects of the coded variables X_1 and X_2, respectively; b_{11}, and b_{22} are the squared effects; b_{12} : factor interaction half-effects [15].

Coefficients of the effect to each factor noted *b* were determined by matrix algebra according to the following relation:

$$b = (X^tX)^{-1}X^ty \qquad (5)$$

Where X is the experiment matrix in coded variables, X^t is the transposed experiment matrix and $(X^tX)^{-1}$ is the reverse of the matrix product of (X^tX) [16]. The coefficient of the effect of each Factor, were calculated using trial software Modde 9.1.

4. Results and discussion

4.1. UV-visible of eosin

The UV-visible absorption spectrum of an aqueous solution of eosin at pH = 6, has four bands, a major band with a characteristic absorption maximum at 516 nm and three lowest absorption band located at 485 nm, 341 nm and 300nm respectively. UV band is due to the $\pi \rightarrow \pi^*$ transition and the visible band which is more intense due to the transition $n \rightarrow \pi^*$ (λ_{max}= 516 nm). The latter is responsible for the red colour that characterizes eosin at this pH (see figure 2).

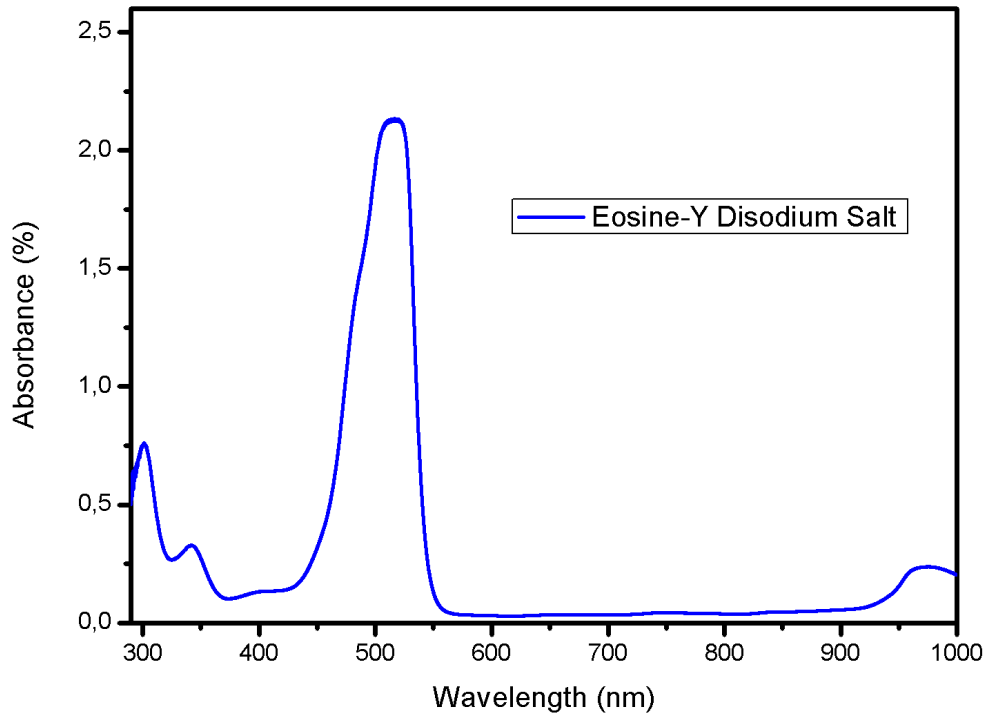

Figure 2. UV-visible absorption spectra of eosin dye in distilled water at T=20°C.

4.2. Kinetic of polymerization by UV-visible spectrophotometer

The visible photo-polymerization of the formulation consisting of the system (eosin and acrylamide), was studied by means of a UV-Visible spectrophotometer.
Figure 3 presents the decrease of the absorption peak of the eosin molecule at 516nm with irradiation time. The photo-induced electron transfer from the dye to the amine leads to the formation of a radical produced from the carbonyl compound (ketyl type radical), and another radical derived from the hydrogen donor.
The eosin molecule changes its absorbance maximum during the polymerization reaction, at t = 0min, the maximum of absorbance is observed at the wavelength (λ= 522nm), after 8 minutes under visible light, the maximum of absorbance became at λ = 516 nm which is very close to the maximum absorbance of eosin in distilled water (λ = 516nm). We can say that the amount of un-reacted eosin is negligible (it remains in the water at the end of the reaction as shown in the visible spectrum at 8 minutes).

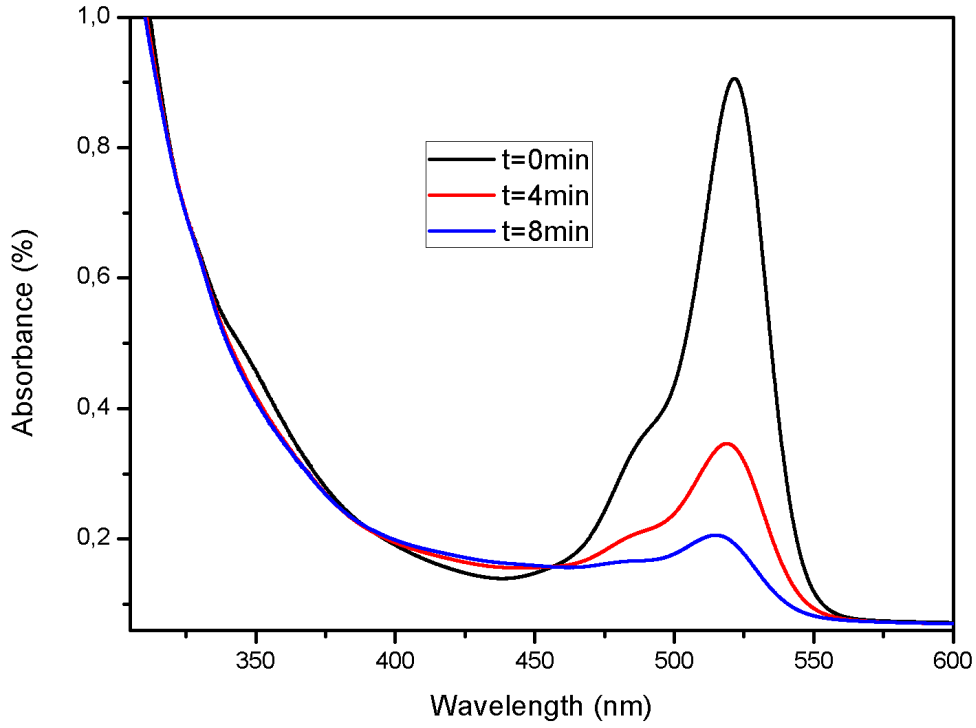

Figure 3. Spectral changes of eosin in the reagent solution based on acrylamide monomer in aqueous medium. Irradiation was performed at visible light under air atmosphere at T=20°C.

When a solution of eosin is irradiated at visible light, the gradual fading of the solution is observed, which is reflected by the decrease in the intensity of the absorption band centered on 516 nm which confirms that the dye molecule has a significant impact in the reaction of polymerization (figure 4).

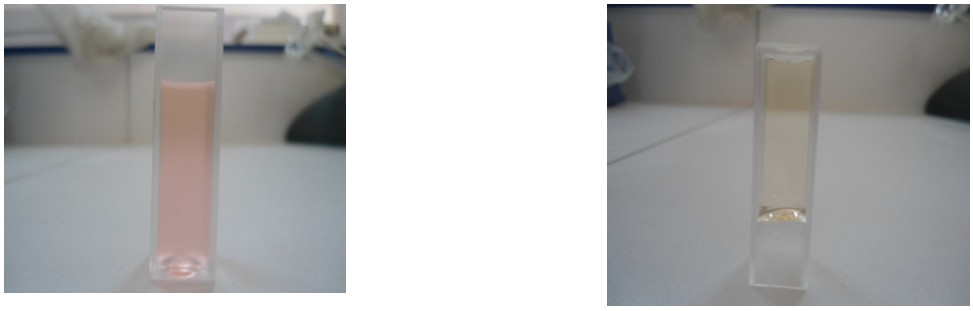

t=0min t=8min

Figure 4. Discoloration of eosin after photopolymerization of polyacrylamide under visible light (a) at t=0min, (b) at t=8min.

Figure 5 represents the corresponding reaction scheme. The photo-polymerization of vinyl monomers is typically initiated by radicals produced from the hydrogen donor (TEOA). The ketyl radicals are generally not reactive toward vinyl monomers due to steric hindrance, but are involved in the termination reaction of the macromolecular chains.

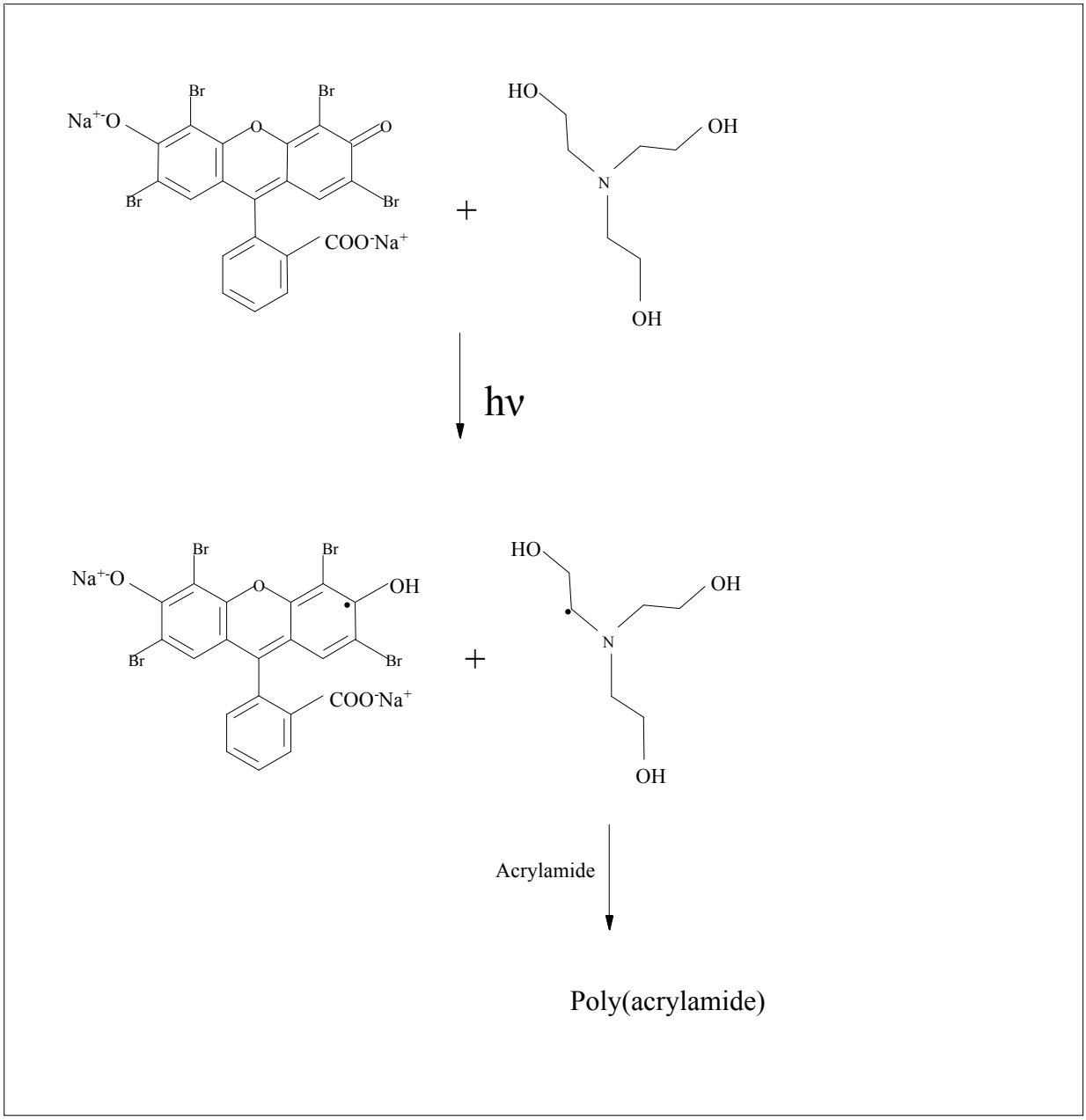

Figure 5. Reaction scheme of the photo-initiated radical polymerization by eosin.

4.3. FTIR characterization

Figure 6 represents the polymerization kinetics of the same mixture as discussed above, obtained by FTIR analysis. Changes could be observed in the intensities of the stretching frequencies of the C=C double bond by exposing the sample to visible light.
Conversion rate of 90% was obtained corresponding to the band at 812cm^{-1}. Only trace amounts of remaining monomers and oligomers were observed at an irradiation time of 8 min.

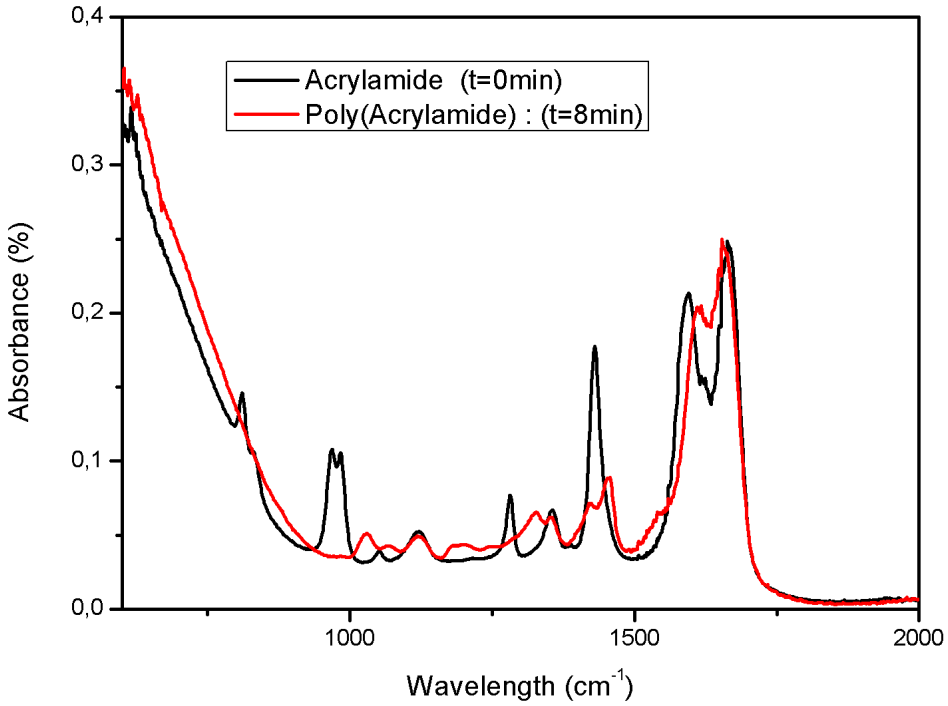

Figure 6. Infrared spectra changes of the C=C double bond absorptions of acrylamide in aqueous medium. Irradiation was performed at visible light under air atmosphere at T=20°C.

4.4. Model validation

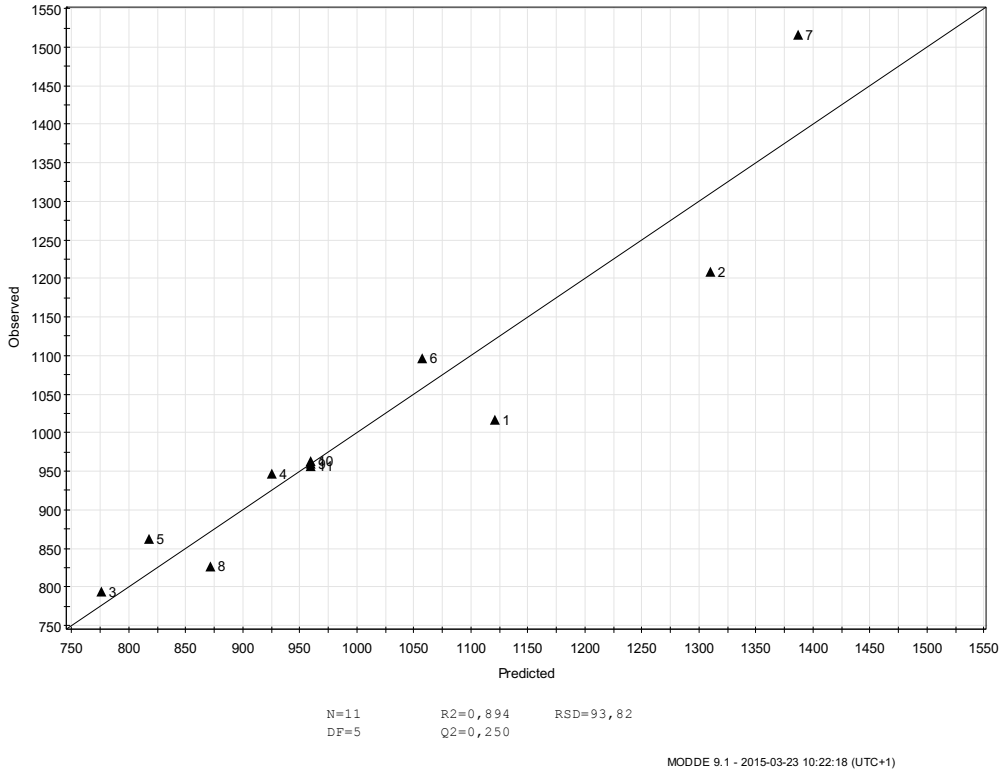

Figure 7. Relation between experimental and predicted ESR using eq (4).

Experimental results and the predicted values obtained using model (Eq. (4)) are given in Fig. 7 As can be seen; the predicted values match the experimental values reasonably well with R-Sq of 90%

and R-Sq (adj) of 80% for response y. In result, the central composite design could efficiently be applied for the modeling of ESR of cross-linked polyacrylamide.

5. Conclusion

Swelling of cross-linked polyacrylamide in distilled water was studied. The central composite design was applied to design an experimental program to provide data to model the effects of degree of cross-linking (X_1) and temperature (X_2) on swelling ratio. The parameters used in the design were; degree of cross-linking and temperature. The predicted values match the experimental values reasonably well, with R-Sq of 90 % and R-Sq (adj) of 80 % for response *y*. The result of optimization predicted model presented the maximal of swelling result with 1290% at the optimal condition of degree of cross-linking 2 % and temperature 70°C. This study has shown that central composite design could efficiently be applied for the modeling of equilibrium swelling ratio ESR of cross-linked polyacrylamide in distilled water, and it is an economical way of obtaining the maximum amount of information with the fewest number of experiments.

References

[1] Singh B, Chauhan N, Kumar S, Bala R 2008, *Int. J. Pharm.* **352** 74.
[2] Yongrui P, Zheng Z, Bao M, Li Y, Zhou Y, Sang G, 2015 *Chem. Eng. J.* **273** 1.
[3] Jeffrey C, Chuan-Pei L, Dhirendra K, Ping-Wei C, Lu-Yin L 2013, Journal of Power Sources **240** 779.
[4] Pellosi D S, Estevao B M, Semensato J, Severino D, Baptista M S, Politi M J, Hioka N, Caetano W 2012, J. Photochem. Photobiol. A, **277** 8.
[5] Ritchie E E, Princz J I, Robidoux P Y, Scroggins R P 2013, Chemosphere, **90** 2129.
[6] Gerasimova M A, Sizykh A G, Slyusareva E A 2009, J. Photochem. Photobiol. B, **97** 117.
[7] Popielarz R, Vogt O 2008, J. Polym. Sci. Part A Polym. Chem. **46** 3519.
[8] Kim D, Scranton A B, Stansbury J W 2009, J. Polym. Sci. Part A Polym. Chem. **47** 1429.
[9] Fouassier J P, Allonas X, Burget D 2003, Prog. Org. Coatings. **47** 16.
[10] Encinas M V, Rufs A M, Bertolotti S G, Previtali 2009, C M, Polymer, **50** 2762.
[11] Kincl M, Turk S, Vrecer F 2005 *Int. J. Pharm.* **291** 39.
[12] Xu H, Paxton J, Lim J, Li Y, Wu Z 2014 *J. Pharmaceut. Biomed. Anal.* **98** 371.
[13] Ghaedi M, Mazaheri H, Khodadoust S, Hajati S, Purkait M K 2015 *Spectroc. Acta A* **135** 479.
[14] K. Khoder, doctoral thesis, Limoges university, 2011.
[15] Ivana M S, Ivan M S, Stanisa T S, Dragoljub G G 2014 *Energy* **77** 66.
[16] B. Dali Youcef, doctoral thesis, Tlemcen university, 2009.

Age Modulates Fe_3O_4 Nanoparticles Liver Toxicity

Y. Baratli,[1,2,*] M. Tlili,[1] H. Ben Miled,[1] Z. Ben Barka,[1] L. Ben Taher,[3] H. Abdelmelek,[1] O. Tebourbi,[1] B. Geny[2]

[1] Université de Carthage, Laboratoire de physiologie intégrée, Faculté des Sciences de Bizerte, Tunisie
[2] Université de Strasbourg, Laboratoire Mitochondries, Stress Oxydant et Protection Musculaire, Strasbourg, France
[3] Université de Carthage, Laboratoire de Synthèse et Structures de Nanomatériaux, Faculté des Sciences de Bizerte, Tunisie

ABSTRACT

We examined the effects of iron oxide nanoparticles (ION) on mitochondrial respiratory chain complexes activities in young (3 months) and middle-aged (18 months) rat liver, organ largely involved in body iron detoxification. Isolated liver mitochondria were extracted using differential centrifugations. Maximal oxidative capacities (Vmax, complexes I, III, and IV activities), Vsucc (complexes II, III, and IV activities), and Vtmpd, (complex IV activity) were determined in controls conditions and after exposure to 250, 300, and 350 μg/ml Fe_3O_4 in young and middle-aged rats. In young liver mitochondria, exposure to ION did not alter mitochondrial function. In contrast, ION dose-dependently impaired all complexes of the mitochondrial respiratory chain in middle-aged rat liver: Vmax (from 30 ± 1.6 to 17.9 ± 1.5; $P < 0.001$), Vsucc (from33.9 ± 1.7 to 24.3 ± 1.0; $P < 0.01$), Vtmpd (from 43.0 ± 1.6 to 26.3 ± 2.2 μmol O_2/min/g protein; $P < 0.001$) using Fe_3O_4 350 μg/ml. Interestingly, 350 μg/ml Fe_3O_4 in the form of Fe^{3+} solution did not impair liver mitochondrial function in middle-aged rats. Thus, ION showed a specific toxicity in middle-aged rats suggesting caution when using it in old age.

Keywords

Nanoparticles, Iron oxide, Mitochondrial respiratory chain, Middle-aged liver, Young liver.

1. INTRODUCTION

Iron oxide nanoparticles hold immense potential in a vast variety of biomedical applications such as magnetic resonance imaging (MRI), targeted delivery of drugs or genes, tissue engineering, targeted destruction of tumor tissue through hyperthermia, magnetic transfections, iron detection, chelation therapy, and tissue engineering [1]. Reports demonstrate that ION have the ability to assess focal hepatic lesions [2] and to label human hepatocytes [3]. However, nanoparticles pose a high health risk because of their ability to reach every part of the organs and tissues and their interaction with cellular functions. Concerning NP clearance, it is known that they are primarily phagocytozed by macrophages in the liver (Kupffer cells) [4]. Thus, the largest detoxification organ of human beings, the liver, is reached by the highest amount of nanoparticles, over all the other tissues [5]. Furthermore, mitochondria are considered a major cell compartment relevant to possible nanoparticle toxicity [6]. Impairment of mitochondria might be a key problem since mitochondrial dysfunction may result in reduced cellular ATP delivery, increased reactive oxygen species production, and triggering of apoptosis pathways. Accordingly, mitochondrial

dysfunctions occur early in many acute or chronic diseases such as peripheral arterial or pulmonary diseases [7]. Mitochondrial involvement in ION toxicity remains controversial and either no deleterious effects [8] or mitochondrial impairments have been observed [9]. Since, to date, no study investigated the potential effects of iron oxide nanoparticles on middle-aged mitochondria and since the liver is a key organ in iron and NPs detoxification, we investigated and compared for the first time the effects of three different concentrations of Fe_3O_4 nanoparticles (250, 300, and 350μg/mL) on young and middle-aged liver mitochondrial respiratory chain complexes activities.

2. EXPERIMENTS

2.1. Animals.

Young (n = 6, age 3 months) and middleaged (n = 6, age 18 months) Wistar male rats were housed in a thermoneutral environment (22 ± 2◦C), on a 12 : 12 h photoperiod, and were provided food and water *ad libitum*. This investigation was carried out in accordance with the Guide for the Care and Use of Laboratory published by the US National Institute of Health and approved by the institutional animal care committee (NIH publication number 85-23, revised 1996). Rats were submitted to general anesthesia with 3% isoflurane and oxygen (1 L/min) in an induction chamber (Minerve, Esternay, France). Anesthesia was maintained with 1.5% isoflurane and 1 L/min oxygen at under spontaneous ventilation. A midline laparotomy was performed and the liver was excised, cleaned, and then immediately used for the study of respiratory parameters. Similarly, three additional Wistar rats aged 18 months were studied, in order to investigate the potential effect of iron oxide *per se*.

2.2. Exposure of Mitochondria to Nanoparticles or to Iron Oxide.

The iron oxide nanoparticles were mixed with a solution of NaCl 9%.Themixture was then stirred vigorously and sonicated for 60min to break up aggregates. Particle suspensions were vortexed immediately before each use. Before measurement, 3mL of solutionMcontaining 100mM KCL, 50mM mops, 1mM EGTA, 5mM Kpi, and 1mg/mL bovine serum albumin (BSA) was added to the oxygraph chambers for 10min.Then, 0.50mg of mitochondrial protein was placed in the oxygraph chambers with 10mM glutamate and 2.50mM malate as substrates. The temperature was maintained at +25◦C. Isolated liver mitochondria were incubated with different concentrations of Fe_3O_4 (0, 250, 300, and 350 μg/mL) during 30 min at +25◦C. To discriminate if the results obtained might be due to the size or to a general response pattern in front of iron oxide exposure, we submitted middle-aged liver mitochondria to a Fe^{3+} solution with concentration of 350 μg/mL Fe_3O_4. To obtain free Fe^{3+} ions a precise mass of Fe_3O_4 nanoparticles was dissolved in a small volume of concentrated HCl under gentle heating [10]. Two experiments were conducted *per* animal, and thus number of data was six.

3. RESULTS and discussions

3.1. Effects of ION on young liver mitochondrial respiratory chain complexes activities

Complexes I, III, and IV Activities. The Vmax in the group treated with increasing doses of ION (250, 300, and 350 μg/mL) was not modified as compared to the control group (27.2 ± 4.5; 29.7 ± 4.1; 29.0 ± 3.1 versus 29.8 ± 5.6 μmol O2/min/g protein) (Figure 1(A)).

Complexes II, III, and IVActivities.*V*succ was unchanged whatever the dose of ION (27.5 ± 4.2, 30.9 ± 4.2, and 30.1 ± 3.3 for Fe_3O_4 250, 300, and 350, respectively, as compared to control values 35.0 ± 3.7 μmol O2/min/g protein) (Figure 1(B)).

Complex IVActivity.*V*tmpd, reflecting complex IVactivity, was notmodified after ION treatment as compared with control group (46.3 ± 4.5, 49.7 ± 4.9, and 50.0 ± 3.8 for Fe_3O_4 250, 300, and 350, respectively, versus 50.0 ± 6.2 μmol O2/min/g protein) (Figure 1(C)).

Taken together, these data support that Fe_3O_4 nanoparticles, whatever the doses used, failed to alter any of the liver mitochondrial respiratory chain complexes activities in young rats.

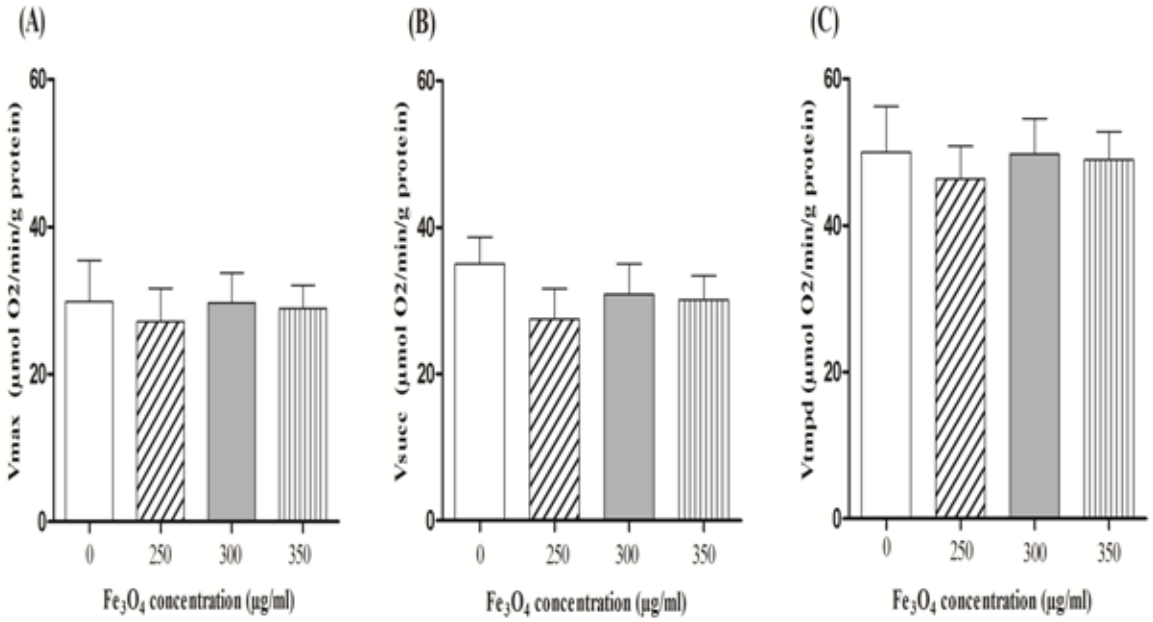

Figure 1: Effects of iron oxide nanoparticles (Fe_3O_4) on young liver mitochondrial respiratory chain complexes activities. (A) *V*max reflects complexes I, III, and IV activities and is measured using glutamate and malate. (B) *V*succ reflects complexes II, III, and IV activities and is measured using succinate. (C) *V*tmpd reflects complex IV activity and is measured using TMPD and ascorbate as mitochondrial substrates. Data are means ± SEM

3.2. Effects of ION on Middle-Aged Liver Mitochondrial Respiratory Chain Complexes Activities.

When the middle aged liver rats were exposed to different concentrations of ION, the *V*max, *V*succ, and *V*tmpd decreased significantly.

Complexes I, III, and IV Activities. The maximal oxidative capacities,max, reflecting I, III, and IV activities significantly decreased whatever the dose of IONPs. At 250 μg/mL, *V*max was decreased as compared to the control group (24.4 ± 1.4 versus 30 ± 1.6 μmolO2/min/g protein; $P < 0.05$). *V*max at 300 and 350 μg/mL were also decreased as compared to control values (23.8 ± 1.0 and 17.9 ± 1.5 for Fe_3O_4 300 and Fe_3O_4 350 μg/mL, respectively, versus CON: 30 ± 1.6 μmolO2/min/g protein; $P < 0.001$). The *V*max decrease was greater when

using higher ION concentration. Thus *V*max was significantly lower after Fe_3O_4 350 μg/mL as compared to 300 and 250 μg/mL (Figure 2(A)).

Complexes II, III, and IV Activities. At 250 μg/mL, *V*succ, reflecting complexes II, III, and IV activities, tended to decrease as compared to the control group (27.0 ± 2.3 versus 33.9 ± 1.7 μmolO2/min/g protein).The statistical significance was reached at 300 μg/mL and 350 μg/mL (Fe_3O_4 300 μg/mL: 25.8 ± 1.0 versus CON: 33.9 ± 1.7 μmol O2/min/g protein; $P < 0.05$) and Fe3O4 350 μg/mL (24.3 ± 1.0 versus 33.9 ± 1.7 μmol O2/min/g protein; $P < 0.01$) (Figure 2(B)).

Complex IV Activity. *V*tmpd, reflecting complex IV activity, decreased significantly after exposure to Fe_3O_4 250 μg/mL as compared to the control group (33.0 ± 2.9 versus 43.0 ± 1.6 μmol O2/min/g protein; $P < 0.05$). Similarly, *V*tmpd, decreased when exposed to 300 μg/mL of Fe3O4 (32.9 ± 1.9 versus 43.0 ± 1.6 μmol O2/min/g protein; $P < 0.05$) and to 350 μg/mL (26.3 ± 2.2 versus 43.0 ± 1.6 μmol O2/min/g protein; $P < 0.001$) (Figure 2(C)).

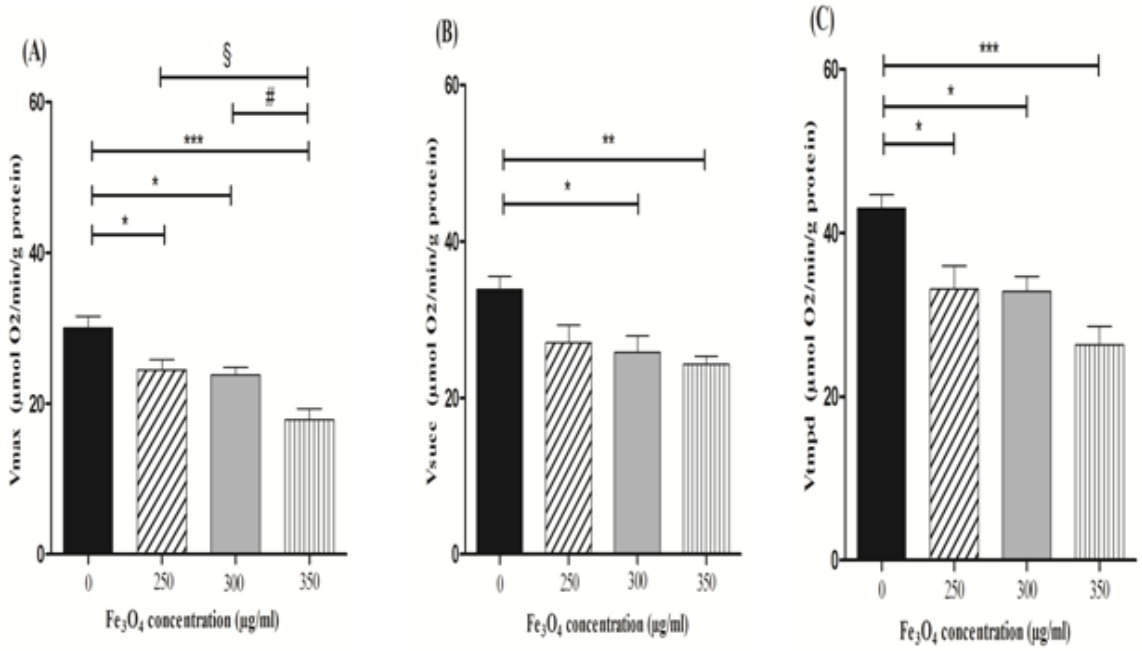

Figure 2: Effects of iron oxide nanoparticles (Fe_3O_4) on middle-aged liver mitochondrial respiratory chain complexes activities. (A) *V*max reflects complexes I, III, and IV activities and is measured using glutamate and malate. (B) *V*succ reflects complexes II, III, and IV activities and is measured using succinate. (C) *V*tmpd reflects complex IV activity and is measured using TMPD and ascorbate as mitochondrial substrates. Data are means ± SEM(one-way ANOVA followed by Tukey). *$P < 0.05$; **$P < 0.01$; ***$P < 0.001$ compared to control. #$P < 0.05$ 350 μg/mL compared to 300 μg/mL. §$P < 0.05$ 350 μg/mL compared to 250 μg/mL.

3.3. Effects of Iron Oxide Not in Its Particulate form on Middle-Aged Liver Mitochondrial Respiratory Chain Complexes Activities

When the middle-aged liver rats were exposed to 350 μg/mL Fe_3O_4, Vmax (41.90 ± 3.93 versus 38.08 ± 3.77 μmol O2/min/g protein), Vsucc (44.23 ± 3.443 versus 41.42 ± 3.303 μmol O2/min/g protein), Vtmpd (84.90 ± 5.75 versus 70.08 ± 4.71 μmol O2/min/g protein) (Figure3).

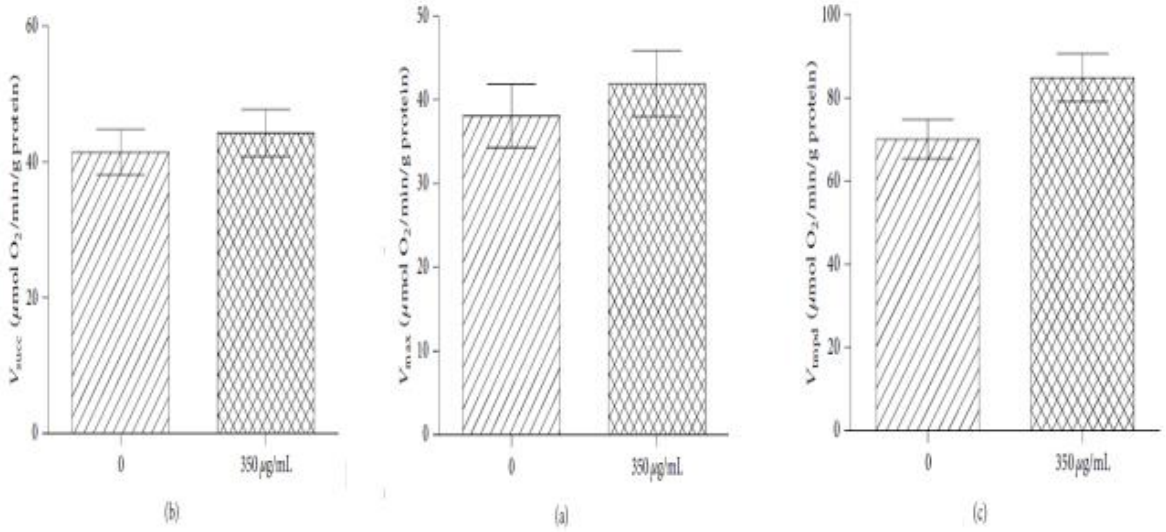

Figure 3: Effects of 350 μg/mL of Fe_3O_4 but not in its particulate form on middle-aged liver mitochondrial respiration. (a) Vmax reflects complexes I, III, and IV activities and is measured using glutamate and malate. (b) Vsucc reflects complexes II, III, and IV activities and is measured using succinate. (c) Vtmpd reflects complex IV activity and is measured using N, N, N', N'-tetramethyl-pphenylenediaminedihydrochloride (TMPD) and ascorbate as mitochondrial substrates. Data are means ± SEM.

The main results of this study are to demonstrate that, unlike young animals, middle-aged rats are sensitive to iron oxide nanoparticles (ION). Indeed, liver mitochondrial respiration chain complexes I, II, III, and IV activities are altered whatever the concentration of Fe_3O_4used. Such impairment is not observed when using 350 μg/mL of Fe_3O_4but not in its particulate form.

To the best of our knowledge, no data are available concerning potential related effects of high levels of iron oxide nanoparticles and age on mitochondria. This is particularly interesting since the liver is a major iron storage organ [11]. Very interestingly, the data were different when middle-aged liver rats were exposed to the same ION concentrations than the young ones. In middle-aged liver rats, ION at 250, 300, and 350 μg/mL significantly decreased Vmax, Vsucc, and Vtmpd corresponding together to complexes I, II, III, and IV activities of the mitochondrial respiratory chain.

Several mechanisms might explain these results like increased fragility of older mitochondria and iron accumulation. First, the fragility of mitochondria seems to increase in function of age. Thus, studies reported that mitochondria isolated from the organs of aged animals are

also aged in terms of cytosolic and mitochondrial oxidative stress and losses of enzymatic activities [12]. Accordingly, studies demonstrated that aging induces the loss of mitochondrial function in liver of rodents and monkeys [13]. Similarly studies investigated the effects of iron accumulation on mitochondrial integrity and function with age [14]. Investigating the pharmacokinetics of ION in rats, Schnorr et al. [15] demonstrated that the half-life and the resulting signal changes in blood and liver vary significantly with age. Thus, iron accumulation which is considered a feature of the aging process [16] might be associated with a mitochondrial iron increase. In particular under conditions of cellular stress, this may be a potential causative factor of age-related mitochondrial dysfunction [17]. Taken together, these data confirm that age likely modulates Fe_3O_4 nanoparticles liver toxicity and one might propose that a threshold of toxicity might play a key role.

4. CONCLUSION

In summary, we demonstrate for the first time that old rats are more susceptible to ION nanoparticle exposure in terms of liver mitochondrial respiration. These age-related changes in liver mitochondrial respiratory chain activity should perhaps be taken into consideration in preclinical and clinical studies of particulate contrast agents.

5. REFERENCES

[1] C.-L.Chen, H. Zhang, Q. Ye et al., "Anewnano-sized Iron oxide particle with high sensitivity for cellular magnetic resonance imaging,"*Molecular Imaging and Biology*, vol. 13, no. 5, pp. 825– 839, 2011.

[2] C. Corot, P. Robert, J.-M. Id´ee, and M. Port, "Recent advances in Iron oxide nanocrystal technology for medical imaging,"*Advanced Drug Delivery Reviews*, vol. 58, no. 14, pp. 1471–1504, 2006.

[3] J. Puppi, R. R. Mitry, M. Modo, A. Dhawan, K. Raja, and R. D. Hughes, "Use of a clinically approved Iron oxide MRI contrast agent to label human hepatocytes," *Cell Transplantation*, vol. 20, no. 6, pp. 963–975, 2011.

[4] E. Sadauskas, H. Wallin, M. Stoltenberg et al., "Kupffer cells are central in the removal of nanoparticles from the organism,"*Particle and Fibre Toxicology*, vol. 4, article 10, 2007.

[5] D. Olmedo, M. B. Guglielmotti, and R. L. Cabrini, "An experimental study of the dissemination of titanium and zirconium in the body," *Journal ofMaterials Science:Materials inMedicine*, vol. 13, no. 8, pp. 793–796, 2002.

[6] K.Unfried, C. Albrecht, L.-O. Klotz, A. VonMikecz, S. Grether-Beck, and R. P. F. Schins, "Cellular responses to nanoparticles: target structures and mechanisms," *Nanotoxicology*, vol. 1, no. 1, pp. 52–71, 2007.

[7] F. Thaveau, J. Zoll, O. Rouyer et al., "Ischemic preconditioning specifically restores complexes I and II activities of the mitochondrial respiratory chain in ischemic skeletalmuscle," *Journal of Vascular Surgery*, vol. 46, no. 3, pp. 541–547, 2007.

[8] H. A. Jeng and J. Swanson, "Toxicity of metal oxide nanoparticles in mammalian cells," *Journal of Environmental Science and Health, A: Toxic/Hazardous Substances and Environmental Engineering*, vol. 41, no. 12, pp. 2699–2711, 2006.

[9] M.-T. Zhu, B. Wang, Y. Wang et al., "Endothelial dysfunction and inflammation induced by Iron oxide nanoparticle exposure: risk factors for early atherosclerosis," *Toxicology Letters*, vol. 203, no. 2, pp. 162–171, 2011.

[10] R. M. Cornell and U. Schwertmann, *The Iron Oxides Structure, Properties, Reactions, Occurrence and Uses*, Wiley-VCH, Weinheim, Germany, 1996.

[11] J. C. Wood, "Diagnosis and management of transfusion Iron overload: the role of imaging," *American Journal of Hematology*, vol. 82, no. 12, supplement, pp. 1132–1135, 2007.

[12] A. Navarro and A. Boveris, "Rat brain and liver mitochondria develop oxidative stress and lose enzymatic activities on aging," *American Journal of Physiology—Regulatory Integrative and Comparative Physiology*, vol. 287, no. 5, pp. R1244–R1249, 2004.

[13] M.D. R. Castro, E. Suarez, E. Kraiselburd et al., "Aging increases mitochondrial DNA damage and oxidative stress in liver of rhesus monkeys," *Experimental Gerontology*, vol. 47, no. 1, pp. 29–37, 2012.

[14] J.Xu, M. D. Knutson, C. S. Carter, and C. Leeuwenburgh, "Iron accumulation with age, oxidative stress and functional decline," *PLoS ONE*, vol. 3, no. 8,Article ID e2865, 2008.

[15] J. Schnorr, M. Taupitz, S. Wagner, H. Pilgrimm, J. Hansel, and B. Hamm, "Age-related blood half-life of particulate contrast material: experimental results with a USPIO in rats," *Journal of Magnetic Resonance Imaging*, vol. 12, no. 5, pp. 740–744, 2000.

[16] S. H. Jung, L. R. DeRuisseau, A. N. Kavazis, and K. C. DeRuisseau, "Plantaris muscle of aged rats demonstrates Iron accumulation and altered expression of Iron regulation proteins," *Experimental Physiology*, vol. 93, no. 3, pp. 407–414, 2008.

[17] J. Xu, E. Marzetti, A. Y. Seo, J.-S. Kim, T. A. Prolla, and C. Leeuwenburgh, "The emerging role of Iron dyshomeostasis in the mitochondrial decay of aging," *Mechanisms of Ageing and Development*, vol. 131, no. 7-8, pp. 487–493, 2010.

Surface Potential Decay and Potential Return of Corona Charged Biomedical Polymer: Simulation and Experimental

N. Hitoum[1], S. Sahli[1], Z. Ziari[1], A. Bellel[2]
[1]University of Constantine, Microsystems and Instrumentation Laboratory (LMI), Constantine, Algeria
[2]University of Constantine, Laboratory of Electronic Material Study for Medical applications, Constantine,Algeria

Abstract: Surface potential measurements have been implemented for many years for analyzing charging/polarization phenomena in dielectrics (polymers) (A. Dolatabadi; 2003). In this work, we have measured the surface potential of a medical polymers charged with corona discharge for different initial voltages. A numerical model, previously developed to reproduce the space charge behavior in polymeric materials, has been then used to simulate the behavior of the surface potential in this biomedical polymer after its charging by a negative corona discharge. The model is one-dimensional, and considers only electrons. It features electron transport using a constant effective mobility, trapping and detrapping in a single deep trapping level and extraction of charge at the ground electrode. Electrons from the discharge are considered as being deposited in the first micrometers inside the polymer. Charges move under the field that they induce in the polymer. The simulated results concern the potential decay and the potential return in the polymer as a function of time. Simulation results show a 'normal' dependence of the potential decay with the different parameters of the model. The results of the decay and the return potential surface obtained through our simulation model are similar to those found experimentally by generating electrostatic charges due to the application of corona discharge on the surface of the dielectric material. Our model is one-dimensional, according to the thickness of the dielectric one, and described the transport of charge in a material after a corona discharge. The trapping, the detrapping and the recombination are taken into account. The charge (electrons and holes) can be mobile or trapped. Like agreed, a mobile electron in the band of conduction (hole in the valence band) has a constant effective mobility, lower than the mobility of band, and which takes account of the trapping and detrapping charge in not very deep traps (G. Chen; 2010). There exists only one level of major trapping for the electrons and the holes, with a maximum density of traps for each type of charge. These trapped loads can be detrapped thanks to a thermo active mechanism. Lastly, the recombination is taken into account for each type of charge, mobile or is trapped.

Keywords: Surface potential, Potential decay, Return potential, Charge injection, Medical polymers.

1. Introduction

The study of the surface potential kinetics *V(t)* has proved to be a powerful tool in investigating the charge carrier transport processes. During the last two decades, many theories were developed to formulate the kinetics of surface potential decay on initially charged highly resistive solids in terms of surface conduction, charge injection, trapping and polarization processes. This method enables a convenient determination of the electrical properties of an insulating material especially if it is assumed like in most of the published results that the surface potential decay is only due to the bulk effects: bulk polarization or injection and transport through the dielectric (H.J. Wintle; 1972)(V. Pouilles, T. Lebey; 1996). Interpretation of surface potential kinetics in polymers by a trapping model has been treated by Chudleigh (P.W. Chudleigh; 1977) and Von Berlepsch (H. Von Berlepsch; 1986). More recently, potential decay measurement in polypropylene films has been studied by Molinie (P. Molinie; 1999). The present work concerns the isothermal potential decay after negative charge deposition on polyforme films. The first part of this paper presents the results of surface potential decay measurements on polyforme films charged by corona effect with different charging levels. The potential measurements were made in open-circuit configuration at room temperature.

The second part deals with the interpretation of surface potential kinetics in polyforme, where charge transport is assumed to occur by hopping of injected carrier between localized trapping centers, and is characterized by four parameters: the coefficient of trapping, the barrier of detrapping, the maximum Density of traps and the recombination coefficient.

In the third part, we are interested in the simulation of the surface potential return according to time, like according to the time of neutralization.

Following Chudleigh's procedure (P.W. Chudleigh; 1977), the transport equations derived from a mathematical model were solved numerically using the finite difference method to obtain the distribution of free and trapped charge densities, the electric field strength and the voltage across the sample at various decay times. By fitting the theoretical curves to the experimental data, the transport parameters will be determined, and their estimated values compared with the data published in the literature.

2. Experimental procedure

The usual arrangement for studying the potential decay using corona charged samples is shown in Figure 1. Polyforme films of thickness L close to 3 mm with one surface held firmly onto an earthed metal plate electrode and the other free have been used. A *DC* voltage was applied to the point situated approximately 15 mm above the polymer free surface, so that a reasonable uniform field may be generated in the gap between the grid and the polymer surface. By selecting appropriate corona point and grid potential *Vp* and *Vg*, respectively, it is possible to charge the polymer surface with ions of either sign and to a potential value limited by the grid potential *Vg* (J.A. Giacometti; 1992). After charging, the sample on its substrate is quickly transferred under a Monroe vibrating probe, of which the case is maintained by feedback at the potential of the surface being studied (D.M. Taylor; 2001). This causes minimum disturbance. The probe is connected to an electrostatic voltmeter (Monroe 244A-2 model), which transmits data to the computer through a Keithley electrometer model 5140.

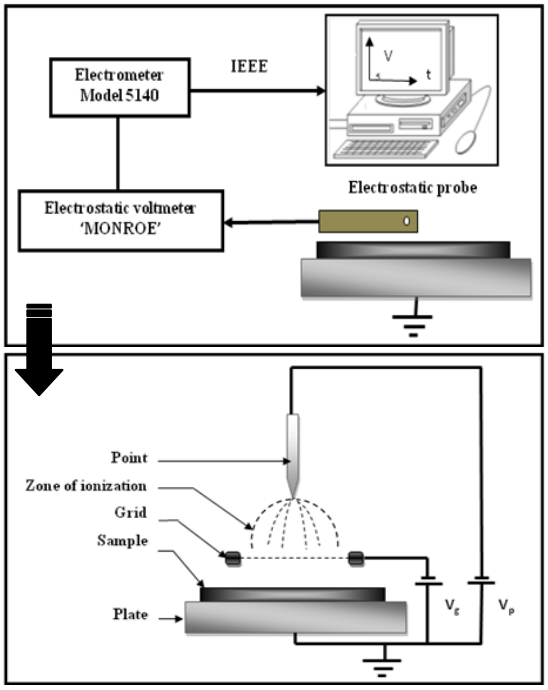

Figure 1. Experimental setup used for the dc corona charging and surface potential measurement.

The surface potential was then measured and continuously recorded. Since it is well known that potential decay depends sharply on the experimental charging conditions such as temperature, the relative humidity and charging duration, all experiments were carried out in an enclosure in which humidity and temperature are controlled. All measurements were carried out in laboratory air at about 300K, and 50% relative humidity. The charging duration was 20 s.

3. Experimental results

In Figure 2, a characteristic family of *V(t)* curves obtained on polyforme films after negative corona charging is reported. For high field strength $E_0 = \frac{V_0}{L}$ values, a fast initial decay followed by a high quasi-plateau value was observed. This initial fast decay may be attributed to the partial injection of the deposited charge into the polymer bulk under the electrical field generated by the charge themselves (T.J. Sonnonstine; 1975) (E.A. Baum; 1977), and this trend was enhanced by raising *V0* .Once injected into the polymer bulk, the electrons may be expected to drift towards the back electrode under the influence of this field (E.A. Baum; 1977).

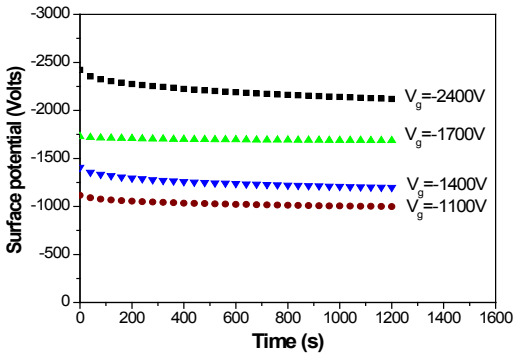

Figure 2. Surface potential decay for various initial potential for polyforme films 3 mm thick.

For low initial potential values (below -1400 V), the decay was very slow. This behavior may be attributed to the possibility that charges are deposited in the surface do not have sufficient energy to be freed and injected into the polymer bulk. Indeed, some surface traps in polyforme are known to be deeper than bulk traps (T. Mizutani; 1981).

Furthermore, one observes the absence of cross-over phenomena, this absence due to the weak electric field (8×10^5 Vm^{-1} for *Vg*= -2400 V). Generally, cross-over phenomena has been observed for a field of about (5×10^7 Vm^{-1}) .This has also been observed by other workers (E.A. Baum; 1977) (M. Ieda, G. Sawa; 1967) (P. Molinie; 1996) and it was attributed to the fact that the partial injection of the deposited charge into the bulk depends on the charging level (T.J. Sonnonstine; 1975).

4. Theoretical model

4.1. Presentation of theoretical model

In our study, we are interested in simulation of transport of charge in the sample after the discharge, in order to see the behavior of the potential of surface according to the relaxation time. For that, we worked

out a model which makes it possible to simulate the decay of surface potential, figure 3 shows boundary conditions of simulation takings into account for our model and the spatial distribution of the electrostatic charges simulated by COMSOL on polyforme. In order to simulate the impact of the discharge on the dielectric one, one injects a density of the charge (electrons or holes according to the sign of the potential of discharge) in the first cell dx of the sample, and one follows then their distribution in the volume of the dielectric one. L: thickness of the sample.

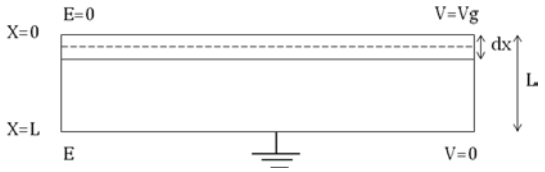

Figure 3. Boundary conditions considered in simulation

We simulated a sample thickness L, where dx is the thickness of the first cell. On the surface (x=0), the electric field is null whereas the surface potential is maximum because of the presence of the charge injected during the corona discharge. With the mass (x=L), the potential is null on the other hand the electric field is not no one. The variation of the charge distribution of space in the dielectric one is at the origin of the variation of the electric potential on the surface of the sample.

Our model is one-dimensional, according to the thickness of the dielectric one, and described the transport of charge in a material after a corona discharge. The trapping, the detrapping and the recombination are taken into account. The charge (electrons and holes) can be mobile or trapped. Like agreed, a mobile electron in the band of conduction (hole in the valence band) has a constant effective mobility, lower than the mobility of band, and which takes account of the trapping and detrapping charge in not very deep traps. There exists only one level of major trapping for the electrons and the holes, with a maximum density of traps for each type of charge. These trapped loads can be detrapped thanks to a thermo active mechanism. Lastly, the recombination is taken into account for each type of charge, mobile or is trapped.

4.3. Results of surface potential decay

The figure 4 presented the variation of experimental surface potential carried out on a film of polyforme, and surface potential decay obtained thanks to our model according to time.

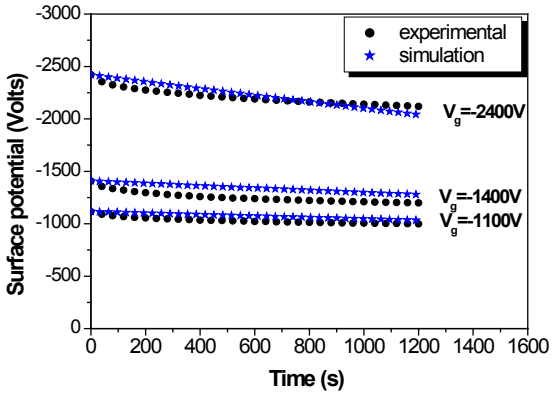

Figure 4. Comparison between experimental surface potential decay curves and calculated for various initial potential.

The shape (general form) of the curve of variation of the surface potential decay obtained thanks to our model of simulation is similar to that which published in the literature (Z. Ziari; 2008) (P. Molinié; 1999) on the one hand, on the other hand with that which found in experiments thanks to the generation of the electrostatic charge due to the application of corona discharge on the surface of a polyforme.

4.4. Return of surface potential

The return of potential consists in neutralizing the charge previously deposited by corona discharge, practically by rubbing the surface of the sample with a piece of cotton soaked with alcohol (E. Osorio; 2009). The surface potential is thus temporarily cancelled, and one follows then the variation of the surface potential after neutralization. Generally, this neutralization is made a few seconds at a few minutes after the stop of the discharge.

In order to take into account this neutralization in the model, we add a density of positive loads (motionless) on the first cell, which cancels the surface potential (density function of the density of charge already present in the dielectric one and of their position compared to the interface air - dielectric); the deposit of this density of positive charge will disturb the internal electric field. For the calculation of the density of the negative charge present in volume, one uses the following relation (Z. Ziari; 2008):

$$\frac{1}{\varepsilon_0 \varepsilon_r} \int_0^L \rho_{(-)} (L - X(i)) dX = V_g \qquad (1)$$

Where *Vg* is the floating potential, $\rho_{(-)}$ is the density of the negative charge in volume of dielectric (electrons), L indicates the thickness of the sample and X(i) is the distance from loads compared to surface. For the calculation of density of the positive charge deposited, one uses the relation according to (E. Osorio; 2009):

$$\rho_{(+)} = \varepsilon_0 \varepsilon_r V_f \frac{L}{dx} \qquad (2)$$

$\rho_{(+)}$: is the density of the positive charge deposited (holes)

The return of potential consists in neutralizing the charge previously deposited by corona discharge, practically by rubbing the surface of the sample with a piece of cotton soaked with alcohol (J. Kindersberger; 2008). The surface potential is thus temporarily cancelled, and one follows then the variation of the surface potential after neutralization. Generally, this neutralization is made a few seconds at a few minutes after the stop of the discharge. The figure 5 presented the variation of experimental surface potential return out on a film of polyforme and return obtained thanks to our model according to time.

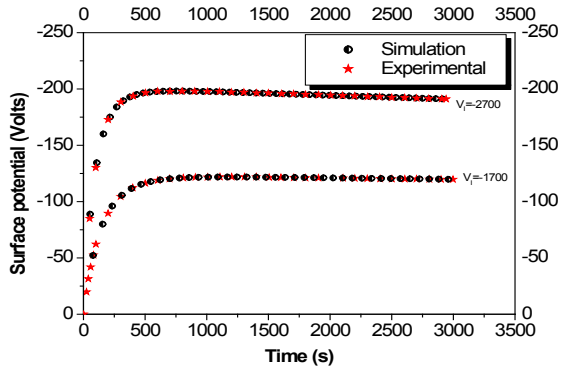

Figure 5: Comparison between experimental surface potential return and calculated for various initial potential.

The maximum value of the potential return is dependent on the neutralization time value and the initial corona discharge. Voltage (for an initial potential discharge of -2700V, the return potential represents about 7%, of the initial potential~ -190 V)(P. Molinié; 2005). Surface potential return behavior obtained with our bipolar model is similar to that found in experiments and also with that published in the literature for ceramic material.

Conclusions

The study of surface potential on corona charged polyforme films 3 mm thick has revealed that the initial decay rate and the injection coefficient increase with increasing charging level. Model of the potential decay has been constructed via a system of partial differential equations for the space and time dependencies of the field across the sample and the transport parameters contained in this model has been determined by fitting procedure.

The model, accounting for the above times, yields a good agreement even for higher charge levels, and this confirms the influence of these times on decay. For weak times of potential return, the model shows a reaugmentation of the surface potential, of the same sign than the initial potential. The maximum value of potential return strongly depends on the density of charge present in the dielectric one but especially of its position (maximum impact when the load penetrated with moist of the sample.

References:

A. Dolatabadi,J. Mosatghimi, V. Pershin (2003) *IEEE,*0-7695-1947-4/03.

G. Chen. (2010), *J. Phys. D: Appl. Phys.* 43 (2010) 055405 (7pp)

J. Kindersberger, C. Lederle. (2008), *IEEE Transactions on Dielectrics and Electrical Insulation* Vol.15,No. 4*; August 2008*.

H.J. Wintle, J. Appl. Phys. 43 (1972) 2927–2930.

V. Pouilles, T. Lebey, P. Castelan, J. Appl. Phys. 79 (11) (1996) 8620–8628.

P.W. Chudleigh, J. Appl. Phys. 48 (1977) 4591–4596.

H. Von Berlepsch, J. Phys. D 18 (1985) 1155–1170.

J.A. Giacometti, O.N. Oliveira Jr., IEEE Trans. EI. 27 (1992) 924–943.

T.J. Sonnonstine, M.M. Perlman, J. Appl. Phys. 46 (1975) 3975–3981.

D.M. Taylor, J. Electrostat. 51 and 52 (2001) 502–508.

E.A. Baum, T.J. Lewis, R. Toomer, J. Phys. D 10 (1977) 487–497.

T. Mizutani, T. Oomura, M. Ieda, Japan J. Appl. Phys. 20 (1981) 855–859.

M. Ieda, G. Sawa, U. Shinohara, J. Appl. Phys. 6 (1967) 793–794.

P. Molinie, Conference Report on Seventh International Conference on DMMA, Bath, 1996,pp. 50–55.

Z. Ziari thèse de doctorat Université de Constantine mentouri 10-TS. (2008).

P. Molinié, J. Electrostatics, Vol. 45, pp. 265-273, (1999).

E. Osorio, M. Toledano, B. Silveira, R. Osorio, Elsevier, (2009).

P. Molinié**,** IEEE Transactions on Dielectrics and Electrical Insulation Vol. 12, No. 5; October 2005.

Correlation between coating hardness and abrasion resistance of coated nanoscale structure surfaces

Said Lakel[1,2,*], Miloud Ibrir[3], K. ALMI[1]

[1]Laboratoire de physique des Matériaux - Université de LAGHOUAT BP 37G, Laghouat, Algeria.
[2]Laboratoire de Matériaux Semi Conducteurset Métalliques, Université de Biskra, Algeria.
[3]Laboratory of Physics of Materials and its Applications, University of M'sila, Algeria.

*Corresponding author E-mail: s.lakel@yahoo.fr

Abstract. One of the most commonly used tribological thin-film coatings is Chromium Nitride (CrN), typically deposited by PVD process. Examples of current applications of this coating include cutting and forming tools: ICE piston ring, hydrodynamic pumps, etc. In selecting coating for tribological applications, one of the critical parameter is the specific wear rate $\varkappa_c$ of the coating. Micro-scale abrasion testing has been used to evaluate the specific wear rate $\varkappa_c$ of chromium-nitride (CrNx) with nanoscale structure coatings on identical a DIN 1.4301 steel substrates. Two different abrasives, SiC and diamond were used. The hardness of the films was found to be in the range of 8-38GPa. The aim of this paper is to evaluate the abrasion resistance of hard coatings, and high abrasive wear resistance $\Omega_c = (1/\varkappa_c)$ of these coatings are compared. The results were compared to those of a chromium nitride reference coating. The results obtained show an excellent correlation between coating hardness and abrasion resistance. The micro-abrasion testing employed offers a simple and inexpensive method for pre-selecting and ranking of coating materials for tribological applications.

1. Introduction

Modern high speed machining and molding industries pose great challenges to protective coatings [1,2]. Hard coatings with good tribological performance are required to meet wide range of engineering applications. Under extreme conditions, such as elevated temperatures with high ambient moisture, conventional solid lubricants like DLC, MoS_2, and h-BN often fail during their lubrication application. CrN coatings are considered one of the most promising candidates for tribological hard coatings due to their good oxidation resistance, anticorrosive and anti-adhesive properties [1,2]. However, the low hardness and inadequate tribological performance have hindered their applications. To improve these properties, the use of nanoscale structure coatings, which have higher hardness and wear resistance [1,2,3,4]. Information of the wear resistance proprieties of coatings is urgently required by suppliers and users to provide confidence in the performance of engineering coatings. In this investigation a coating of chromium-nitride (CrNx) with nanoscale structure, which was previously optimized in dependence of the nitrogen content, was deposited on identical a DIN 1.4301 steel substrates using a PVD technique.

Numerous applications where surface engineering has been applied successfully like cutting or forming processes require enhanced wear resistance [5]. Out of the main wear mechanisms identified to determine lifetime of tools, a considerable amount of abrasive wear takes place when particles,

which are harder than the tool material, are involved. These particles can typically be carbides or oxides (e.g. when cutting steel) or highly strain-hardened fragments (e.g. wear debris generated during deep-drawing). Typically, abrasion resistance is evaluated using wear tests where the bulk mass loss or dimensional changes are monitored [6]. However, for the characterization of the abrasion resistance of surface engineered tool materials on a laboratory scale, a test method where very small samples can be used is highly attractive [7,8]. The best known tribological application of a Calowear method is a micro-scale abrasion test [8–9] and commercial tribometers based on this method are available (e.g. CSEM Calowear and Plint TE-66 micro-scale abrasion tester). Initially, the ball cratering method has been developed for measurements of coating thickness and in this capacity it is still used as a standard test in many industrial laboratories [8,10,12]. Subsequently its use has been extended to measurements of abrasive wear resistance of thin coatings or surface layers and the technique developed is known as a micro-scale abrasion test [8–9]. The name micro-abrasion originates from the very small wear depths and volumes generated in the wear sample by the rotating ball covered with fine abrasive particles. This allows for conducting wear measurements on surface films of several microns in thickness [8–11]. Micro-scale abrasion tests use abrasive slurries or pastes containing fine abrasive particles of micron, or even sub-micron, size [8,10,13]. This small size of abrasive grits is deliberately chosen to obtain good quality optical images of wear craters for accurate determination of a coating thickness or wear volume [13,14]. Wear volume is calculated by measuring the diameter or depth of the wear crater and applying simple geometrical equations [8–10,15]. For coated surfaces the wear coefficients of both the coating and substrate can be determined from a single test [8–10]. Micro-scale abrasion test has also been increasingly used for testing the abrasive wear resistance of bulk materials such as non-ferrous metals and their alloys [8,18], tool steels [8,15,17], plain carbon steel [10],In this work, the hardness and micro-scale abrasion testing was applied to a set of CrNx, nanomaterials coatings deposited by PVD, on identical a DIN 1.4301 steel substrates.

2. Experimental details

2.1 Coating deposition

All coatings investigated have been deposited using an unbalanced magnetron sputtering plant. Cr-N coatings were grown by reactive sputtering in Ar/N_2 atmospheres using a Cr target. Different N/Cr atomic ratios as characterized by wavelength-dispersive electron probe microanalysis have been adjusted by the N2 flow rate resulting in the phase compositions (characterized by X-ray diffraction) given in table 1. As substrates, ground and polished austenitic stainless steel (DIN 1.4301, hardness 200 HV) samples with dimensions Ø 25 - 5 mm and 20 mm- 20 mm-5 mm were used.

Coating hardness was determined from the load vs. displacement data measured using a computer controlled micro hardness tester (Fischerscope H100).

2.2 Abrasive wear characterisations

The abrasion resistance was evaluated using a small-scale abrasive wear test (CaloWear) Fig.1. There, a steel sphere (DIN 1.2067, diameter, 25.4 mm) is rotating against the coated sample in the presence of an aqueous suspension of abrasive particles. In this work, aqueous suspensions of SiC (average grain size, 3.5 μm) and diamond (average grain size, 1 μm) have been used. The sphere was rotated against the sample with a velocity of 0.2 m/s.

Optical micrographs of typical wear craters in coated samples are shown in Fig. 2. The diameter of the resulting wear crater was determined as a function of the sliding distance by means of a calibrated optical microscope, SEM and Talysurfprofilometry to determine the dominating wear mechanisms and the extent of wear damage.The wear crater was measured at intervals corresponding to increments in the sliding distance of about 16 m after removing the steel sphere. After each measurement, the sphere was relocated to the identical position and the typical total sliding distance was about 80 m. The normal force FN on the specimen is determined by the weight of the sphere and the lateral position of the drive sharft (8). To optimize test conditions for this work, FN was varied between 0.18 and 0.45 N, measured by a sensitive load cell.

As can be seen from the total sliding distance of 80 m and the increments of 16 m that five individual data points for all plots of crater volume versus sliding distance have been obtained. The deviation of these five values was typically below ± 7 %.

3. Results and discussion

The aim of a first test series was to optimize test conditions for the abrasive wear test.

The abrasive wear rates of both coating and substrate material is derived from the increasing wear volume depending on sliding distance and normal force during the testing process using the equation described in (18):

$$S.F_N = \frac{V_c}{k_c} + \frac{V_s}{k_s} = \Omega_c V_c + \Omega_s V_s \quad (1)$$

S is the sliding distance and FN is the applied load. V_c and $\varkappa_c$ are the wear volume and load specific wear rate of the coating. V_s and $\varkappa_s$are the corresponding parameters for the substrate. Ω_c and Ω_s are the wear resistance of coating and substrate (Usually the wear resistance, which is the inverse of the wear rate). Knowing the substrate wear resistance and the coating thickness, the coating wear rate could easily be calculated from the measured wear volume.

Thus the abrasive wear rate of the Coating and substrate are calculated by a modification of the equation (1):

$$\frac{s.F_N}{d_a^4} = \left(\frac{k_s - k_c}{k_s.k_c}\right).\left(\frac{\pi.t}{4.d_a^2} - \frac{\pi.R.t^2}{d_a^4}\right) + \left(\frac{4}{k_s}\right).\left(\frac{\pi}{64.R}\right) \quad (2)$$

There, s is the distance slid by the sphere, da is the external diameter of the wear crater, t is the coating thickness and R is the radius of the sphere. A plot of$\left(\frac{s.F_N}{d_a^4}\right)$against$\left(\frac{\pi.t}{4.d_a^2} - \frac{\pi.R.t^2}{d_a^4}\right)$ is thus linear with the intercept and gradient determined by the values of $\varkappa_s$and $\varkappa_c$(see Fig. 3). $\varkappa_s$ can be determined directly from the intercept, and this value is then used together with the gradient to provide $\varkappa_c$.

Fig. 4 shows the abrasive wear rate of coating and substrate determined for a coating of chemical composition CrN1.0 deposited onto an austenitic stainless steel substrate as a function of the normal force applied on the sample. The standard deviation of $\varkappa_c$for the loads investigated is well below 5 %. However, to minimize the error in determining $\varkappa_s$, the normal load for all further investigations was adjusted in the range between 0.3 and 0.4 N.

The abrasion coefficients of Cr-N coatings determined using SiC abrasive slurry and optimized test parameters is illustrated in Fig. 5 as a function of their chemical composition. There, the phase composition as characterized by X-ray diffraction .The abrasion resistance for the Cr coating is about 188.5 Nm/mm^3. For the dual-phase coating consisting of a Cr (N) solid solution and Cr_2N and for the Cr_2N coating, Ω c increase to about 500 Nm/mm^3. Coating close to the composition of stoichiometric CrN yield an abrasion resistance of about 1200 Nm/mm^3.

The abrasive wear behavior of the coatings is shown in Fig. 6, which plots the abrasive wear resistance of Cr-N coatings as a function of their hardness. There is evidently a clear correlation between hardness and abrasive wear, which agrees with the results found in literature ball-on-disk system [8,19].

The data point given in Fig.6 has been obtained for diamond slurry, where the standard deviation yields a value of about 4 %. Although the coating investigated show a wide range of hardness values, Fig. 6 shows an excellent correlation between the coating abrasive wear rate and the hardness.

4. Conclusions

Within this work, several sputtered coating from Cr through Cr_2N and dual-phase coatings consisting of the solid solution Cr (N) and Cr_2N to CrN single phase coatings have been investigated with respect to their abrasion resistance and hardness.

- Both phases are characterized by high hardness, although CrN is more resistant to wear than Cr_2N.
- Repeatable results were obtained for hard coated systems using micro abrasion testing

- The wear resistance of the coating seem to be directly proportional to the hardness
- No significant affect of load on the wear rate is observed.

The results obtained show an excellent correlation between coating hardness and abrasion resistance. Moreover, the micro-abrasion testing employed offers a simple and inexpensive method for pre-selecting and ranking of coating materials for abrasive wear situations.

Figure caption

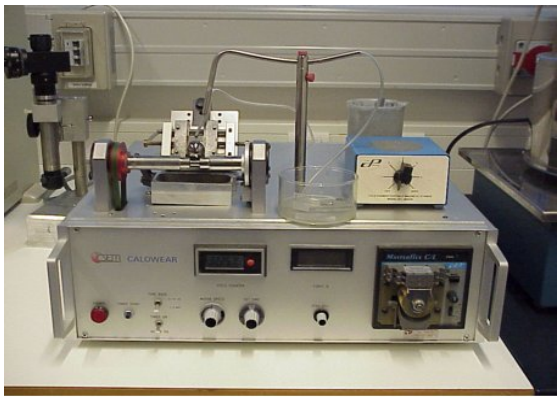

Figure 1.Experimental set-up of the CSM Calowear Tester

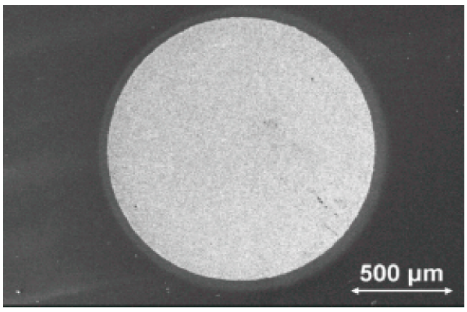

Figure 2. Optical micrographs of the wear crater in a CrN1.0 coating (SiC slurry)

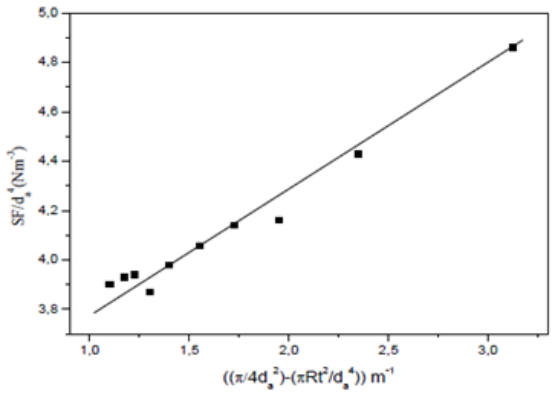

Figure 3. Plot of abrasion wear data obtained for a CrN1.0 coating according to equation (2) using a SiC slurry

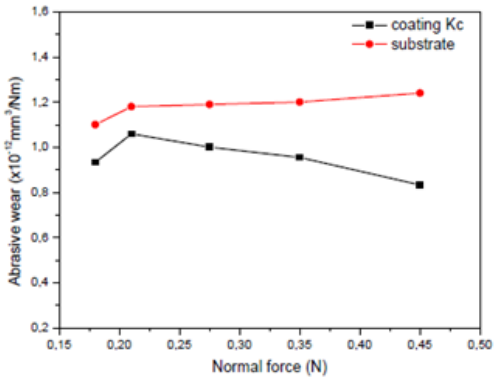

Figure 4. Dependence of the abrasive wear rate of coating

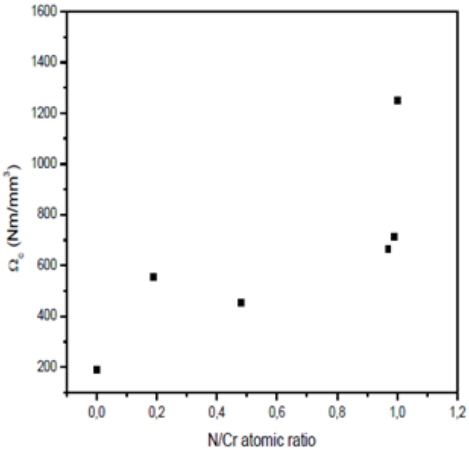

Figure 5. Dependence of the wear resistance of Cr-N coatings on their chemical and phase compositions (see Table 1, Sic slurry)

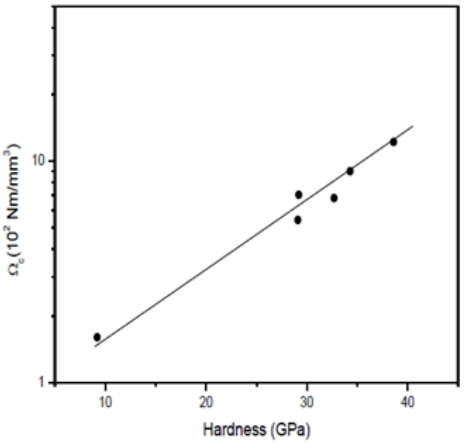

Figure 6. Abrasive wear resistance as a function of hardness (H) of Cr-N coatings

Table 1 table caption

Table 1. Properties of the Coatings

Coating	Chemical composition	Phase composition	Phase composition	Coating thikness(μm)

Cr-N1	Cr	Cr	9.2	5.62
Cr-N2	CrN0.19	Cr(N)-Cr2N	26.8	5.15
Cr-N3	CrN0.48	Cr2N	32.4	4.65
Cr-N4	CrN0.97	CrN	26.3	4.22
Cr-N5	CrN0.99	CrN	33.5	3.92
Cr-N6	CrN1.0	CrN	38.1	3.85

References

1. M. Kathrein, C. Michotte, M. Penoy, P. Polcik and C. Mitterer, Surf. Coat. Technol. 2005; 200: 1867–1871

2. J. Lin et al, International Journal of Refractory Metals and Hard Materials, vol. 28, p. 2-14, 2010.

3. P.H. Mayrhofer,P.Eh. Hovsepian, C. Mitterer, W.-D. Münz, Surf. Coat. Technol.177–178 (2004) 341.

4. B. Podgornik, S. Hogmark, O. Sandberg, Wear 261 (2006) 15.

5. JL Mo, MH Zhu, A Leyland, A Matthews ; Surf. Coat. Technol - Available online 6 November 2012

6. S.J. Bull, R.I. Davidson, E.H. Fisher, A.R. McCabe, A.M. Jones: Surf. Coat. Technol. 130 (2000) 257

7. R. Gahlin, M. Larsson, P. Hedenqvist, S. Jacobson, S. Hogmark: Surf. Coat. Technol. 90 (1997) 107.

8. Rutherford KL, Hutchings IM. Surf Coat Technol. 1996; 79: 231–9.

9. Stack MM, Mathew M. Wear2003; 255:14-22.

10. J. M. Fildes, J. S. Meyers, R Kilaparti, E Schlep ; Wear 2012 ; 274-275:414–422.

11. Allsopp DN, Hutchings IM.. Wear 2001;251:1308–14.

12. Thomson V, Hintermann HE, Chollet L. Surf Technol 1979; 8:421–8

13. Gee MG, Gant A, Hutchings I, Bethke R, Schiffman K, Van Acker K, Poulat S, Gachon Y, von Stebut J. 2003; 255:1–13.

14. A J Gant, M G Gee ; A review of micro-scale abrasion testing J. Phys. D: Appl. Phys. 44 (2011)

15. Adachi K, Hutchings IM. Wear-mode mapping for the micro-scale abrasion tests. Wear 2003; 255:23–9.

16. Imbeni V, Martini C, Prandstraller D, Poli G, Trepanier C, Duerig TW. Preliminary. Wear 2003; 254:1299–306.

[17. Trezona RI, Allsopp DN, Hutchings IM.. Wear 1999;225–229:205–14.

18. Å. Kassman, S. Jacobson, L. Ericson, P. Hedenqvist and M. Olsson, Surf. Coat. Technol., 50 (1991) 75-84.

19. P.H. Mayrhofer, G. Tischler,C. Mitterer; Development of sputtered Cr-N hard coatings from a materials scientist's point of view,Galvanotechnik, 92(3) (2001) 762-771.

Micro-pollutant risk assessments in Tunisian urban water distribution network: Case of Pb, Hg, Cd, F

W Guissouma[1] **and Jamila Tarhouni**[1]
[1]National School of Agronomy of Tunis, Tunisia

E-mail: wiem.guissouma@gmail.com

Abstract. A sampling campaign has been done over 100 Tunisian water consumption points (tap). Laboratory analysis results show that there is no significant quality standards exceeding cases are observed for Cadmium, Lead and Mercury. These laboratory analysis shows that drinking water quality is rather affected by high fluoride levels exceeding 2mg.L-1. Over these samples, 7% of them presents a non-compliant with the Tunisian national standard [1] and the international guidelines [2] The overtake cases are located essentially in southern Tunisian areas, i.e. Medenine, Gabes, Gafsa and Tataouine. However, commonly northern and central Tunisian areas are characterized by low fluoride concentration level below 0.1mg.L-1.These undertake cases doesn't agree with the World Health Organization recommendations [2]. A fluoride health risk characterization approach is established to identify the most sensitive population of adverse effect like tooth decay, dental fluorosis and skeletal fluorosis.

1. Introduction

The Tunisian Ministry of health is devoted to control and monitor the quality of drinking water supplied by the Tunisian National Water Distribution Utility (SONEDE). This good bacteriological drinking water quality has been translated by decreasing diarrheal diseases. However, previous National Authority's work has not supported the drinking water chemical hazards, i.e Fluoride and some heavy metals for the health risks assessment. Moreover, Tunisian National Water Distribution Utility (SONEDE) has not adapted an efficient corrective action to meet the Tunisia drinking water quality requirements. To prevent adverse effects related to high daily exposure, a good water quality management should be established.
A quality assessment of Tunisian drinking tap water (Fluoride, cadmium, lead and mercury levels) is realized; firstly by compliance assessment to national and international standards and secondly by exposure assessment associated to risk via drinking water.

2. Methods

Step 1: A sampling campaign has been done over 100 Tunisian water consumption points (tap). The samples plan is defined by second degree probing with reasoned choice (mass of population served by networks water SONEDE).

Step 2: The laboratory analysis is used to quantitatively describe micro-pollutants (Pb, Cd, Hg, F) levels in drinking tap water samples.

Step 3: Conformity assessment of drinking water quality realized by referring to national and international guidelines presented in the table 1.

Step 4: Risk assessment approach is proceeded with four basic steps [3]:

- Hazard identification
- Selection of toxicity references values (TRV)
- Exposure assessment
- Risk characterization

Table 1 _ Guideline for fluoride in drinking water

	NT 14.09 (2013)	OMS (4th edition, 2011)	European guidelines 98/83/CE	Canadian guidelines	Quebec Standards	American Standards
Fluorure mg/L	1.5	1.5	1.5	1.5	1.5	4

3. Descriptive analysis results

- For lead analysis results: although it is a major constituent of the EPA network; nevertheless it has not been quantified in any sample. The low lead concentrations (less than a quantification limit: 5 $\mu g.L^{-1}$) can be an indicator of the physicochemical properties water (little or no corrosive water).
- For cadmium analysis results: 1% of samples are quantified in Menzel Bourguiba area in Bizerte with value of 0.67 $\mu g.L^{-1}$. The presence of trace cadmium in water is considered as an indicator of water resource contamination that can be related to EL Fouledh company activities or to ancient Joumines mines.
- For mercury analysis results: 4% of samples are quantified in Nabeul and Ben Arous areas. The mercury presence in water is considered as an indicator of an accidental water contamination.

FIG. 1_Maximum fluoride level in drinking water in Tunisia areas

The areas affected by water contamination remain subject to discussion and should be investigated by Health Ministry and by the Tunisian National Water Distribution Utility SONEDE.

- For fluoride analysis results: 98 % of samples are quantified. Figure 1 shows that The fluoride levels in drinking water is highly variable from north to south: less than 0.1 mg.L^{-1} in some northern areas i.e. Beja and Jandouba and exceeding 2 mg.L^{-1} in southen areas, i.e. Medenine, Gabes, Gafsa and Tataouine.

Moreover Figure 2 shows that the drinking water supply in northern Tunisian areas is done from surface water that has generally low contents of fluorine (less than 0.5 mg.L-1). However in southern Tunisia areas the drinking water supply is done from groundwater naturally rich with fluoride.

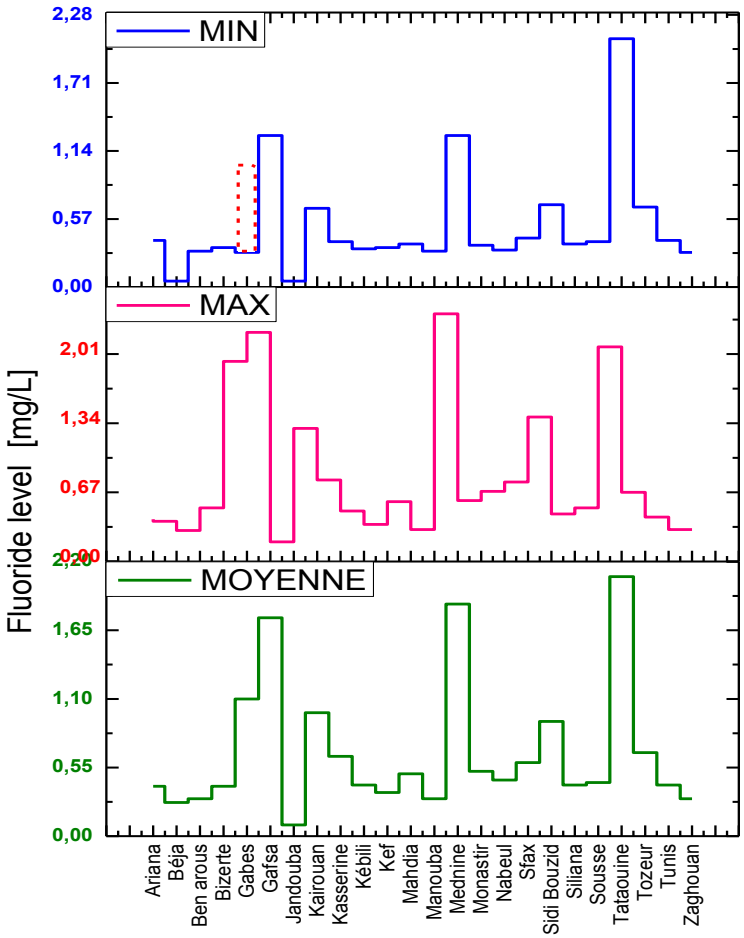

FIG. 2_ Intra-regional variability of fluoride level in tap water

4. Compliance assessment

By referring the Tunisian national standard [1] and the international guidelines presented in the table 1, the following point can be highlighted:

- For fluoride; 7% non-compliant cases are recorded; Figure 3 shows that the overtake cases are defined essentially in southern Tunisian areas, i.e. Medenine, Gabes, Gafsa and Tataouine.
- For mercury 2 % non-compliant cases are recorded

- 100 % compliant cases with standards of cadmium and lead are recorded.

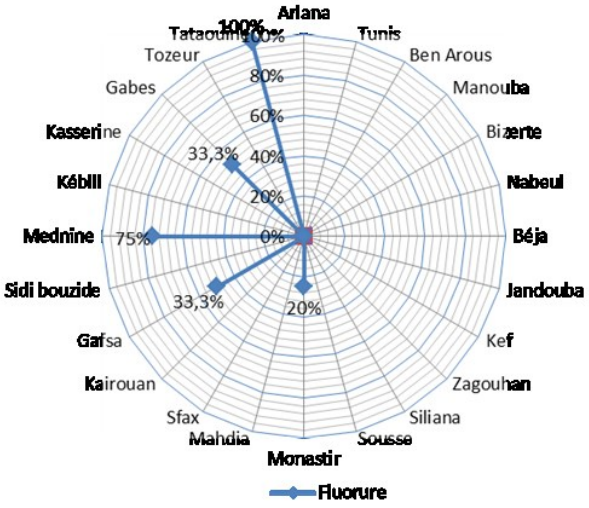

FIG_ 3 : Ratio of non-compliance fluoride levels in tap water

5. Risk assessment

WHO recommends a value of 10% to 20% of the ADI for quantify fluid intake of Cd, Hg, Pb. while for Fluoride WHO recommends a value of 80% of the ADI. So that feed remains the major source to heavy metals exposure however water remains the major source to fluoride exposure by ingestion route. On the other hand the concentrations of Cd, Hg, Pb not have been quantified in 98% of samples. Fact that only fluoride element is taken in risk assessment part.

6. Comparison of fluoride daily exposure and safety limit

The Superior Council of Public Hygiene of France (CSHPF) has set fluoride safety limits. The daily fluoride intake equal to the safety limits for life-time does not cause any health adverse effects.

WHO considers that fluoride concentration in water of 1.5 mg L^{-1} would exceed fluoride safety limit for infants.

A comparative approach is adopted between the daily fluoride exposure and the safety limit established by CSHPF in the aim to define the exceeding cases of safety limit in drinking water presented in figure 4.

This approach is based on:

a) safety limit established by CSHPF:4 mg day^{-1} for adults, 0.7 mg day^{-1} for children and 0.4 mg day^{-1} for infants.

b) Water consumption defined by the WHO: 2 L day^{-1} for adults, 1 L day^{-1} for children and 0.75 L day^{-1} for infants

The percentages of exceeding cases of the safety limit are:

- 33% for infants;
- 20% for children.
- 3% for adults

This analysis pinpoints that infants and children are the most population exposed to fluoride risk.

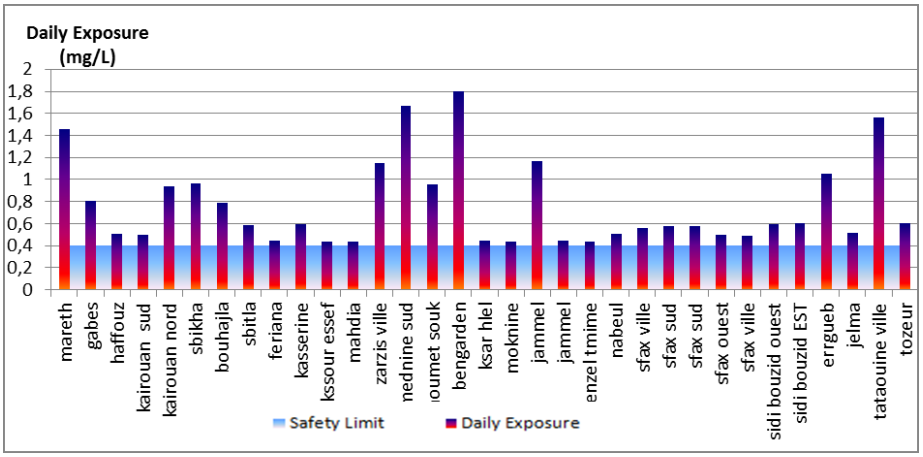

(a)

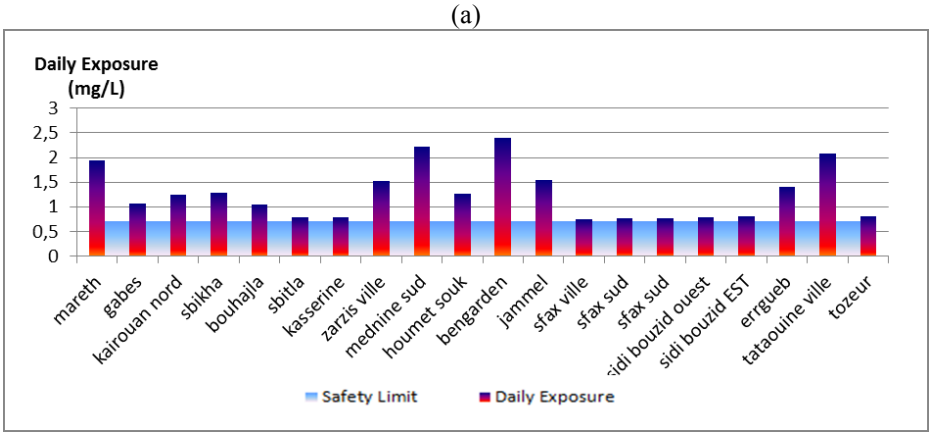

(b)

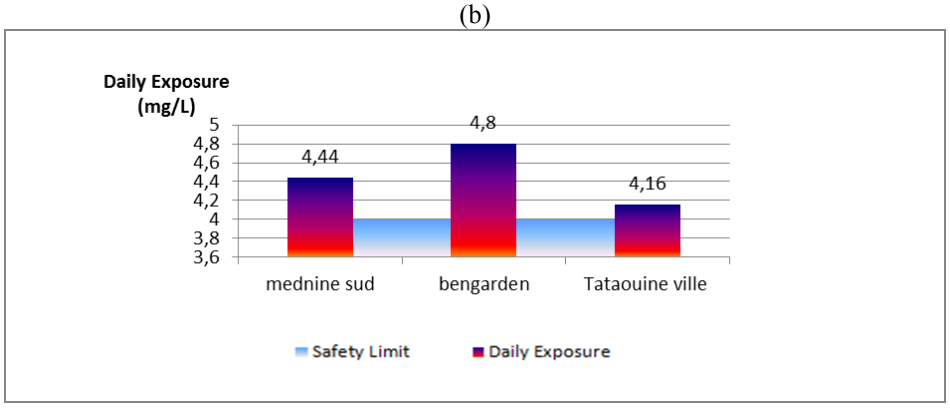

(c)

FIG 4_ Exceeding fluoride safety limit cases for infant (a), children (b) and adult (c)

7. Conclusions

This study was the starting point for locating areas with high sanitary risk attributed to drinking water. No significant quality standards exceeding cases are observed for Cadmium, Lead and Mercury. However the real problem related to drinking water supply in Tunisia is the highly fluoride levels. Hence, fluoride levels needs to be monitored and strictly controlled by Tunisian Ministry of health and Tunisian National Water Distribution Utility (SONEDE).

- 75% of Tunisian areas present dental decay risk through tap water consumption,
- 25% of Tunisian areas present dental fluorosis risk through tap water consumption,

- 20% of Tunisian areas present skeletal fluorosis risk through tap water consumption.

Children and infant are the most population exposed to risk associated to excess and deficiency fluoride levels in water.

References

[1] NT09.14 ; 2013 : Norme Tunisienne relative à la qualité des eaux destinées à la consommation humaine ; 2014.

[2] WHO ; 2003 : Rapport sur la santé dans le monde – façonner l'avenir, n.d.

[3] InVS; 2007 : Estimation de l'impact sanitaire d'une pollution environnementale et évaluation quantitative des risques sanitaires

Reduction of Reflection on Solar Cell by Anti-Reflection Coating to increase Efficiency

Khalid Omar[1*], Khaldun A. Salaman[2], Z. Hassan[3]

[1]Member of National Chair of Materials Science and Metallurgy, University of Nizwa, 616 Nizwa, Oman

[2]Al-Nahrin Nanorenewable Energy Research Center, Solar Cell Research Department, Al-Nahrin University, Baghdad, Iraq

[3]School of Physics, University of Science Malaysia, 11800 Penang, Malaysia

[*]Corresponding author email: khalidomar@unizwa.edu.om

Abstract. The ZnO/n-PS (100) layers were characterized using scanning electron microscopy, which revealed that the ZnO film deposited along the walls partially covered the tiny pores of the n-PS (100) layer during the Radio Frequency sputtering process. The Photoluminescence emission peaks indicated the nanocrystalline characteristic of the n-PS (100) layer and the ZnO film. Raman measurements of the ZnO/PS layers indicated that a high-quality ZnO nanocrystalline film was formed. Thus, ZnO/n-PS (100) layers are excellent anti-reflection layer that exhibit exceptional light trapping at wavelengths ranging from 400 to 1000 nm.

Introduction

The porous semiconductor is a common porous material that has promising optoelectronic applications. In particular, the tunable physical properties, the large surface-to-volume area, and the broadening in band gap are some of its important properties that enhance the development of optoelectronic applications, such as solar cell devices, Cullis et al., (1997) and Sharma et al., (2001). Availability of materials and processing possibilities mainly motivate the original choices, but the increased attention in solar cell devices has triggered a more systematic search for new materials and cell structures that may fulfill the ultimate requirements of efficiency, cost, stability, and environmental effects, Burgelman et al., (2004). The properties of the PS layer, such as band gap broadening and surface roughening, make it a promising material as anti-reflection coating (ARC) for solar cells, Koyama (1992). The PS layer used as ARC serves as a gettering center to reduce the impurity levels of the Si substrate, Tsuo et al., (1996). The solar cell device absorbs more light energy, thus the efficiency has increased. Furthermore, to obtain high efficiency, some studies suggest that pyramidal-shaped microparticle zinc oxide (ZnO) be used as ARC layer (window layer) in the solar cell device to increase light trapping and absorption of light energy, Banik (2009). Solar cells currently lack efficiency due to electrical and optical losses, such as reflection, shadowing, non-absorbed radiation, and recombination. ZnO film is deposited on the PS layer as ARC in the front side of the solar cell device to increase the amount of light directed toward the solar panel, thus its efficiency has enhanced.

Results and discussion:

The ZnO film was deposited on the n-PS (100) layer through RF sputtering. The ZnO film and the PS layer were composed of nanocrystals, and the ZnO thin film was deposited along the walls and partially filled or covered the tiny pores of the n-PS (100) layer during RF sputtering. Thus, the deposition of the ZnO film on the n-PS (100) layer is expected to slightly reduce the roughness of the surface. Figure 1 shows the SEM image of the ZnO/n-PS (100) layers at 20 min etching time.

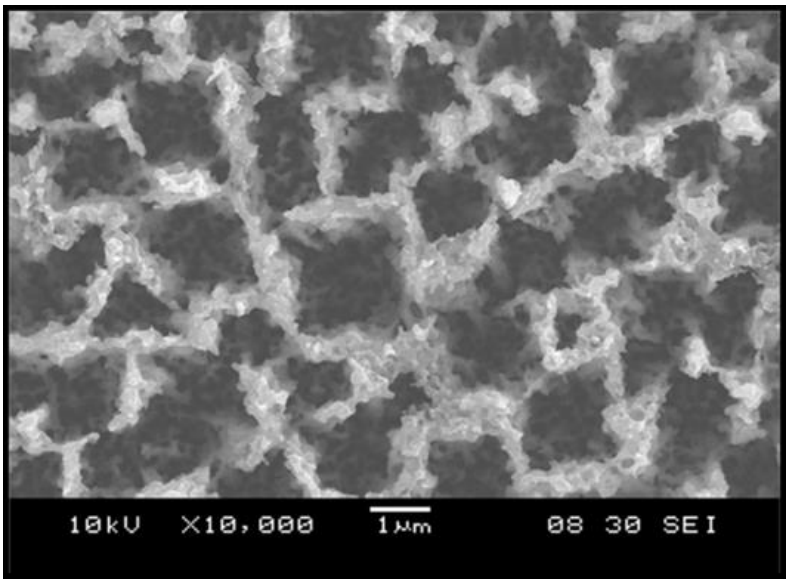

Figure 1: SEM image of ZnO/n-PS (100) layers.

Figure 2 shows that the ZnO nanocrystalline film is expected to be integrated into the nanopores, thereby the surface roughness decreases, Singh et al., (2009). Therefore, the ZnO/n-PS (100) layers are preferrable as an ARC in solar cell devices because their surface texture will reduce light reflection and will change the optical transitions by bouncing the light back and forth within the cell several times. This phenomenon is possible due to the presence of top and bottom sections of the surface layers.

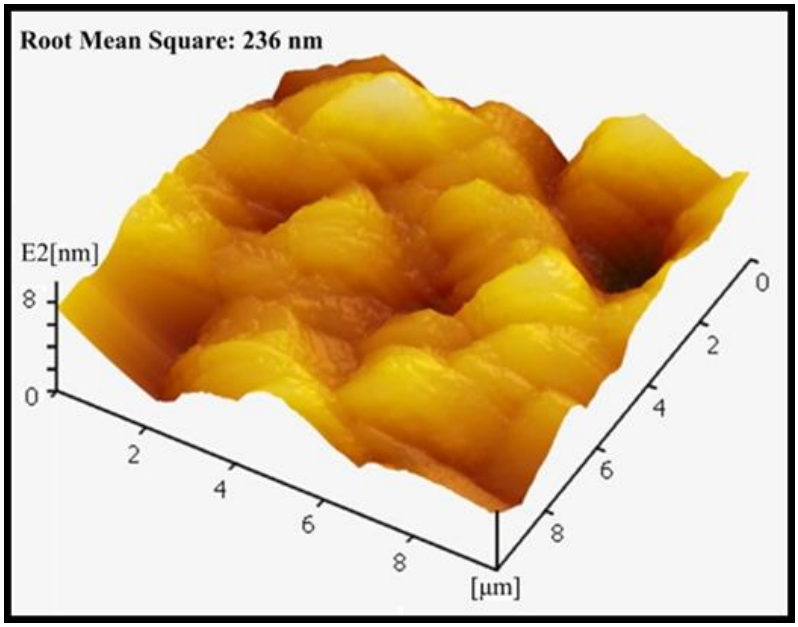

Figure 2: AFM image of the ZnO/n-PS (100) layers

Figure 3 shows the PL spectra of the ZnO/n-PS (100) layers measured by a He-Cd excitation laser source at 325 nm at room temperature. PL peak at 387.5 nm was due to the near band edge emission in the wide band gap of the ZnO, which resulted from the direct recombination of the photogenerated charge carriers, Yu et al., (2009) and Umar et al., (2006) and Samanta et al., (2011). The red shift in the PL peak of ZnO film toward a longer wavelength of 387.5 nm was attributed to Zn vacancies in the ZnO energy band gap, Singh et al., (2007) and Kayahan (2010). It is very possible that the contamination of the ZnO/n-PS (100) layers create defect level state caused the red shift in the PL peak of the ZnO film, Prabakaran et al., (2008).

High-intensity PL peak at 637.5 nm is attributed to the n-PS (100) layer, Liu et al., (2003). The blue shift in the PL peak of the PS layer toward a shorter wavelength of 637.5 nm is attributed to the quantum confinement effect of electrons in nanosized particles in the n-PS (100) layer, Chen at al., (1999) and Hummel et al., (1995). The observed emission at 637.5 nm is related to the surface oxidation through ZnO deposition, Kayahan (2010). The red emission peak for the PS layer containing a shoulder peak at 605 nm is related to the high number of intrinsic structural defects resulting from Zn vacancies, Jayakumar et al., (2010). The probability of recombining electrons and holes in low-dimensional structures will be higher, which will lead to an increase in the optical confinement energy and photo-conversion efficiency, Jayakumar et al., (2010) and Wu et al., (2000).

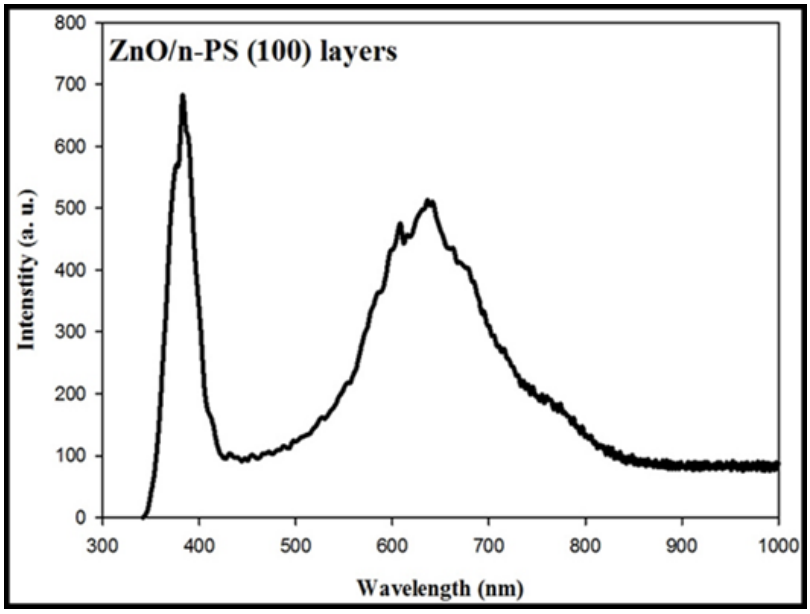

Figure 3: PL spectra of the ZnO/n-PS (100) layers

Figure 4 shows the Raman spectra of the ZnO/n-PS (100) layers compared to the as-grown Si sample, as measured by an argon-ion excitation laser source at 514.5 nm at room temperature. A sharp solid line was produced in the as-grown Si sample spectrum with FWHM of 3.0 cm^{-1} located at 521.4 cm^{-1} due to the scattering of first-order phonon, Liu et al., (2003). The penetration depth of the argon-ion laser is greater than the thickness of the ZnO film; thus, the spectrum of the n-PS (100) layer displayed a very strong Raman intensity peak that shifted to red and became broader at 517 cm^{-1} with FWHM of 8.6 cm^{-1} compared to that of the as-grown Si sample.

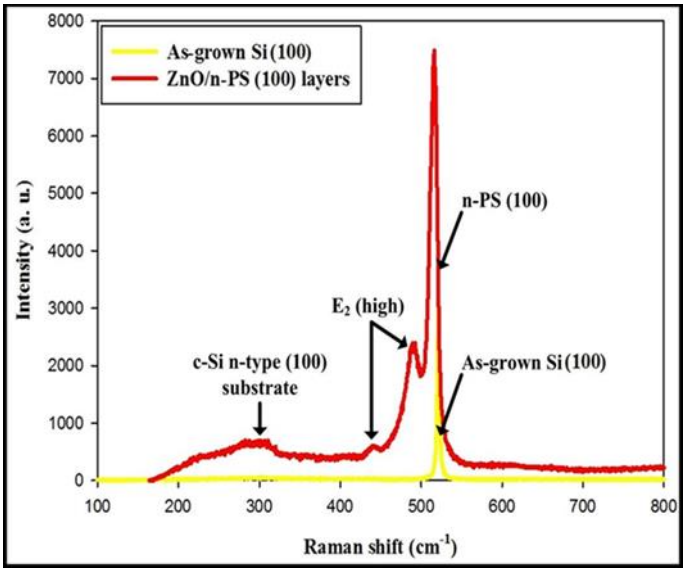

Figure 4: Raman spectra of the ZnO/n-PS (100) layers

The observed phonon frequency at 302 cm-1 was related to the c-Si n-type (100) substrate in the ZnO/n-PS (100) layers, Hassan et al., (2011), which has a broadened FWHM and a low intensity compared to that of the as-grown Si sample. The formation of the n-PS (100) layer led to a peak-shift asymmetry and an increase in the peak intensity. This feature of Si nanocrystals is attributed to the quantum confinement of optical phonons in the electronic wave function of Si nanocrystals, Tsuo et al., (1994). The E2 symmetry is a nonpolar phonon mode with two frequencies, namely, E2(high), which is related to oxygen atoms, and E2(low), which is related to the zinc sub-lattice, Alim et al., (2005) and Martínez-Criado et al., (2010).

Figure 5 shows the reflection spectra of the ZnO/n-PS (100) layers compared to the n-PS (100) layer at 20 min etching time and the as-grown Si sample. The n-PS (100) layer consisted of nanopores. Therefore, the refractive index decreased and became controlled by pores with high porosity, which then led to a decrease in reflection, Aspnes et al., (1979) and Aroutiounian et al., (2004). The n-PS (100) layer reduced light reflection at wavelengths ranging from 400 to 1000 nm compared with the reflectivity of the as-grown Si sample. The lowest effective reflectance was obtained after depositing the ZnO on the n-PS (100) layer, which clearly reduced light reflection and increased light-trapping at wavelengths ranging from 400 to 1000 nm compared to the reflectivity of the n-PS (100) layer and as-grown Si sample.

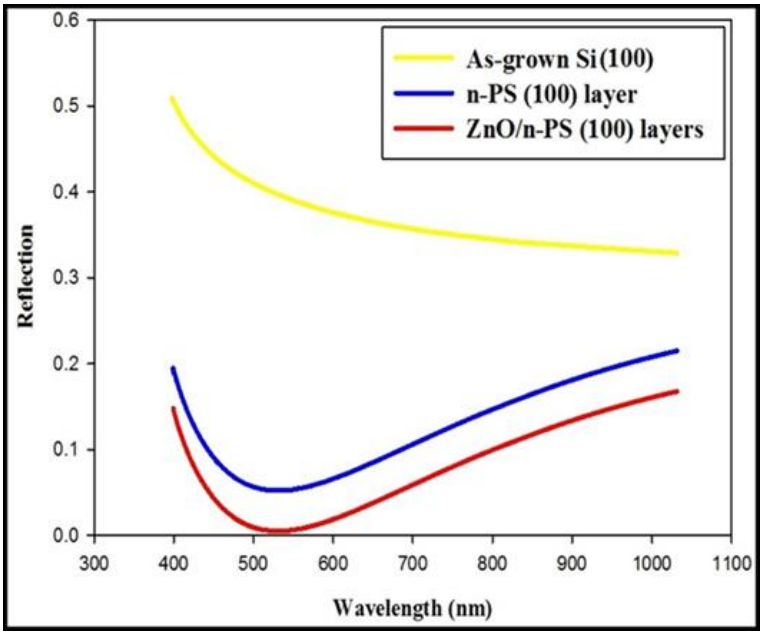

Figure 5: Reflection spectra of the ZnO/n-PS (100) layers compared with those of the n-PS (100) layer and as-grown Si (100) sample.

Reflectance, transmittance, and absorption might also depend on the polarization and geometric distribution of incident radiation. The attenuation of reflectivity was caused by light transmission at the porous region. The incident light hits the ZnO surface and becomes partially reflected when

using the ZnO film as ARC layer in the front side of the solar cell device. This phenomenon should be taken into account in the solar cell where the transmitted light energy in the p-n junction is converted to electrical energy. The reflection is reduced in the ZnO film, with the minimum reflection at ~ 525 to 540 nm. This reduction is due to the deposited 65 nm ZnO film through RF sputtering. The average refractive index of the ZnO film in the visible region was approximately 2, thereby facilitating the refractive index matching between the ZnO film and n-PS (100) layer. A small portion of the incident light will be reflected from the ZnO surface, whereas the remainder of the light will be transmitted and absorbed into the p-n junction.

Conclusion:

ZnO thin film was successfully deposited inside the nanopores of the n-PS (100) layer along the walls and partially filled or covered the nanopores using the RF sputtering system to form ARC layers in the solar cell device. The structural and optical properties of the ZnO/n-PS (100) layers at 20 min etching time were explained. The surface roughness of the ZnO/n-PS (100) layers decreased because the deposition of ZnO partially filled the nanopores of the n-PS (100) layer. The PL emission peaks have proven the nanocrystalline characteristic of the n-PS (100) layer and the ZnO film. Raman measurement of the ZnO/n-PS (100) layers indicated that a high-quality ZnO nanocrystalline film was formed. The lowest effective reflectance was obtained for the ZnO/n-PS (100) layers compared to that of the n-PS (100) layer and as-grown Si sample.

Acknowledgment:

Dr. Omar would like to express his appreciation to University of Nizwa and National Chair of Materials Science and Metallurgy for supporting this work and participating in International Conference of Nanotech Tunisia 2015.

Reference:

Alim K A *et al* 2005 *J. App Phy* **97** 124313

Aroutiounian V M *et al* 2004 *J Phy D; Applied Physics* **37** 25

Aspnes D E *et al* 1979 *Phy Rev B*, **20** 3292

Banik A 2009 *Preparation of pyramidal zinc oxide particle as an antireflective coating for application in solar cell* M.Sc thesis in: University of Texas at Arlington, United States, Texas

Burgelman M *et al* 2004 *Progress in Photovoltaics; Research and Application* **12** 143

Chen C H and Chen Y F 1999 *App Phy Lett* **75** 2560

Cullis A G *et al* 1997 *J App Phy* **82** 909

Hassan J J *et al* 2011 *J Alloys and Compounds* **509** 6711

Hummel R E *et al* 1995, *Solid State Commun* **93** 237

Jayakumar O D *et al* 2010 *Scripta Materialia* **62** 662

Kayahan E 2010 *J Luminescence* **130** 1295

Koshida H Koyama 1992 Visible electro-and photoluminescence from porous silicon and its related optoelectronic properties *Mat Res Soc Symp Proc* **256** 219

Liu Y L *et al* 2003 *J Phy* D*; App Phy* **36** 2705

Martínez-Criado G *et al* 2010 *Acta Physica Polonica* A, **117** 269

Prabakaran R *et al* 2008 *J Non-Cry Solid* **354** 2181

Samanta P K. and Chaudhuri P R 2011 *Sci Adv Mat* **3** 107

Sharma S N *et al* 2001 *App Surf Sci* **182** 333

Singh R G *et al* 2009 Fabrication of zinc silicate from ZnO-porous silicon nanocomposite for broadband emission by chemical route *Int Conf Opt Photo* Chandigarh, India.

Singh R G *et al* 2007 *J Phy* D*; App Phy* **40** 3090

Tsuo Y S *et al* 1996 *Solar Energy Materials and Solar Cell*s **41/42** 41

Tsuo S Y *et al* 1994 *Device applications of porous and nanostructured silicon, in porous silicon* World Scientific Publishing Co Singapore

Umar A *et al* 2006 *Nanotech* **17** 4072

Wu X L *et al* 2000 *Phy Rev* B **62** 7759

Yu C F *et al* 2009 *App Surf Sci* **256** 792

Correlation between structural and optical properties of SiO_2/(Ni:TiO_2) Bragg reflectors processed by dip-coating sol-gel method: The effect of annealing duration and Ni content

H. Sedrati[1,2] , R. Bensaha[2] and P. Miska[3]

[1] Département des Sciences de la Matière, Faculté des Sciences, Université 20 Août 1955, BP 26 El-Hadaïk, Skikda 21000, Algérie

[2]Laboratoire de Céramique, Département de Physique, Université Constantine 1, Route de Aïn El-Bey, Constantine 25000, Algérie

[3]Institut Jean Lamour, CNRS UMR 7198 - Nancy-Université, B.P. 239, 54506 Vandœuvre-lès-Nancy, France

Abstract

The main objective of this paper is the study of the correlation between structural and optical properties of SiO_2/(Ni:TiO_2) Bragg reflectors, under the effect of annealing duration and Ni content, obtained by the dip-coating sol-gel process. The films crystallize in pure anatase phase whatever is the Ni content and the annealing duration. In UV-Vis-NIR analyses, variations of width, position and transmission coefficient of the stop-band were observed. The PL spectra red-shifted with the increase of the annealing duration and the Ni content. As the annealing duration increases, an additional sharp emission peak appears around 867 nm, indicating a reduced number of defects.

Keywords: Bragg reflectors, Nickel doped TiO_2, Photoluminescence, Raman spectroscopy.

1. Introduction

During the two last decades, and Because of their specific optical properties, the Bragg reflectors have been developed and widely exploited in many domain such as vertical cavity surface-emitting lasers [1-3], solar cells [4], photonic crystals [5,6], dielectric nanospheres [7,8], waveguides [9] and spherical microresonators [10,11].

The most important parameters in the fabrication of Bragg reflectors are the refractive index contrast and the number of bilayers. The higher the reflectivity of the stop band, the higher must be both the index contrast and the number of bilayers [12]. Thence, dielectric materials such as SiO_2, Si, TiO_2 and ZrO_2 are often chosen in the fabrication of such reflectors [3, 13-16].

As noticed, the insertion of Ni ions in TiO_2 sol affects the chemical, structural and the optical properties of the films [24]. On one hand, the addition of Ni ions, as dopant, increases the TiO_2 sol viscosity [12]. On the other hand, doping TiO_2 sol with Ni ions decreases the transmission coefficient [25], decreases the electron-hole recombination rate [26] and decreases

the grain size [27]. Moreover, the transmittance and luminescence spectra shift to the longer wavelengths as Ni content increases: this shift can be explained by the localization of trapping level near the valance band or the conduction band [28].

Accordingly, we reported in this study the influence of the Ni doped TiO_2 and the annealing duration on the structural and the optical properties of SiO_2/TiO_2 Bragg reflectors.

2. Experiments

2.1. Solutions preparation

SiO_2 sol was synthesized with tetraethylorthosilicate (TEOS; $Si(OC_2H_5)_4$; 98.0% GC), Fluka-Chemika). TEOS was mixed with ethanol (Et; C_2H_5OH; 96% Reidel-de Haën) as solvent, ultrapure water (H_2O) for hydrolysis and few drops of hydrochloric acid (HCl; 37%) as catalyst. The molar ratios corresponding to TEOS/TEOS:Ethanol/TEOS:Water/TEOS were 1:23:3.2, respectively. The obtained solution is colorless and limpid [29].

Obtaining undoped TiO_2 needs the dissolution of 1 mol of butanol (C_2H_4OH; 99.5%, Reidel-de Haën), 4 mol of acetic acid (CH_3COOH; 99-100%, Biochem Chemopharma), 1 mol of distilled water and 1 mol of tetrabutylorthotitanate (TBOT; $(C_4H_9O)_4Ti$; Fluka-Chemika). The final solution is transparent with a yellowish color [30].

For doping TiO_2, nickel acetate ($Ni(C_2H_3O_2)_2$, $4H_2O$; 99.0% Sigma-Aldrich) was dissolved in few drops of ethanol (Et; C_2H_5OH, 95% Reidel-de Haën) and acetic acid (CH_3COOH; 99-100%, Biochem Chemopharma). The obtained mixture was stirred and heated at 60°C during 2 hours. For doping TiO_2, nickel acetate ($Ni(C_2H_3O_2)_2$, $4H_2O$; 99.0% Sigma-Aldrich) was dissolved in few drops of ethanol (Et; C_2H_5OH, 95% Reidel-de Haën) and acetic acid (CH_3COOH; 99-100%, Biochem Chemopharma). This mixture was stirred and heated at 60°C during 2 hours. Thereafter, the obtained solution was added to TiO_2 sol according to the following contents: 2 at.% Ni and 5 at.% Ni. Finaly, the Ni:TiO_2 sol was stirred at room temperature for 8 hours. The Ni:TiO_2 solution was homogenous with a greenish color [12].

2.2. Procedure of fabrication and annealing

The procedures of fabrication and annealing are presented in Figure 1. SiO_2 sol is deposited on a glass substrate as a bottom layer, followed by the deposition of Ni:TiO_2 sol as a top layer forming one bilayer. The superposition of the bilayers allows obtaining $SiO_2/(Ni:TiO_2)$ Bragg reflectors. In this study, we have realized Bragg reflectors with five bilayers (5/5) at the speed of steeping equals to 4.35 $cm.min^{-1}$. It is interesting to note that each deposited layer was

dried at 100°C for 15 minutes and then treated at 550°C during 30 seconds. At the end of the fabrication process, the obtained samples undergo a final annealing at 550°C for different annealing durations: 10 and 20 minutes.

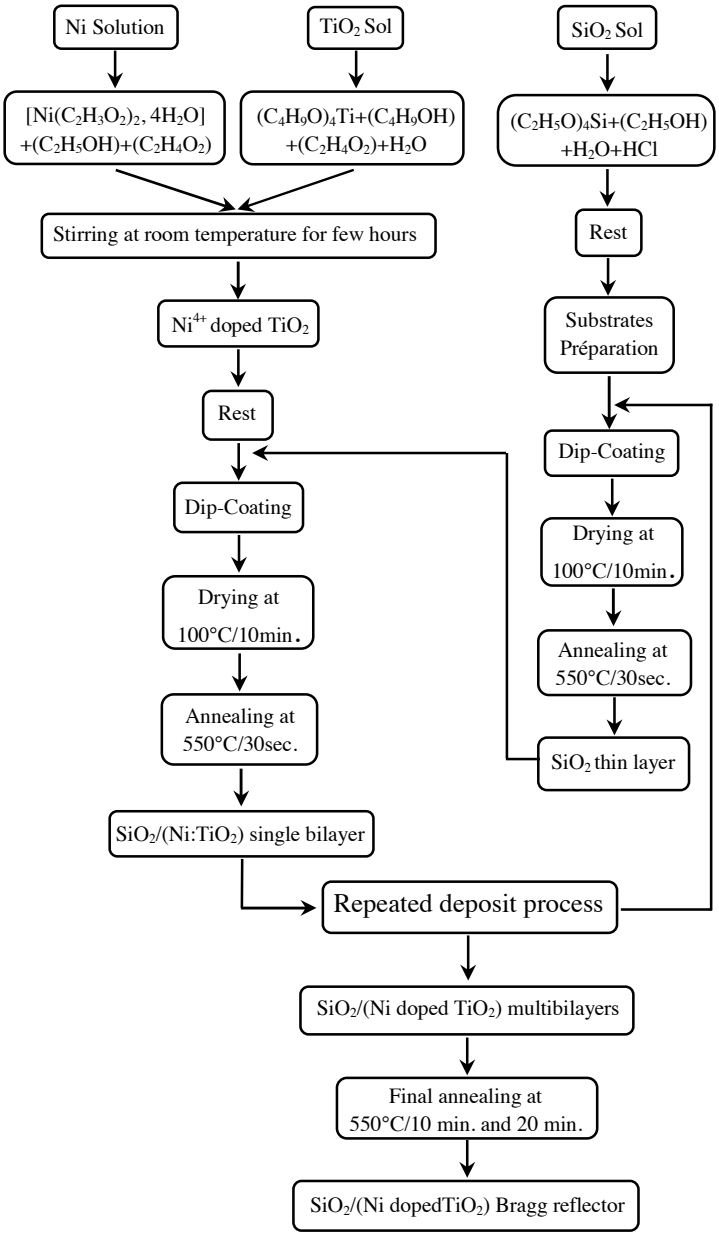

Figure 1. *Process of fabrication of SiO_2/(Ni doped TiO_2) Bragg reflectors*

2.3. Characterization techniques

The obtained samples were investigated by different characterization techniques. X-ray diffraction was performed by "INEL CPS120" diffractometer using CoKα radiation (λ=1.78897 Å) operated at 35 kV and 20 mA. The scans were performed with an incidence angle

of λ_{Co} and the acquisition time for each scan is 15 min. Raman spectra were obtained at room temperature using a LabRam-HR Horiba Jobin-Yvon Raman spectrometer, equipped with a liquid N cooled CCD detector. The laser wavelength was the 532 nm emission line of an Ar^+ laser. The laser irradiance was kept low to avoid any heating effect. UV absorption studies were carried out using UV-Vis double-beam spectrophotometer JASCO V-670ILN-725. The analysis wavelength range was between 190 and 270 nm. The photoluminescence (PL) spectra were obtained by exciting the samples with the 313 nm radiation of Hg lamp and the signal was recorded using TRIAX 190 Jobin-Yvon spectrometer.

3. Results and discussion

3.1. Structural properties

3.1.1. X-ray diffraction

Fig. 2 shows the XRD patterns of the SiO_2/(Ni:TiO_2) Bragg reflectors. The X-ray diffraction patterns of Bragg reflectors with undoped TiO_2, 2 at.% Ni:TiO_2 and 5 at.% Ni:TiO_2 are shown in Fig. 2. All diffraction peaks can be assigned as pure anatase TiO_2 after a heat treatment at 550°C during 10 (Fig. 2(a)) and 20 min (Fig. 2(b-c)), which can be confirmed by the existence of (101), (004), (200), (211), (204), (116), (220), (215) and (224) diffraction peaks.

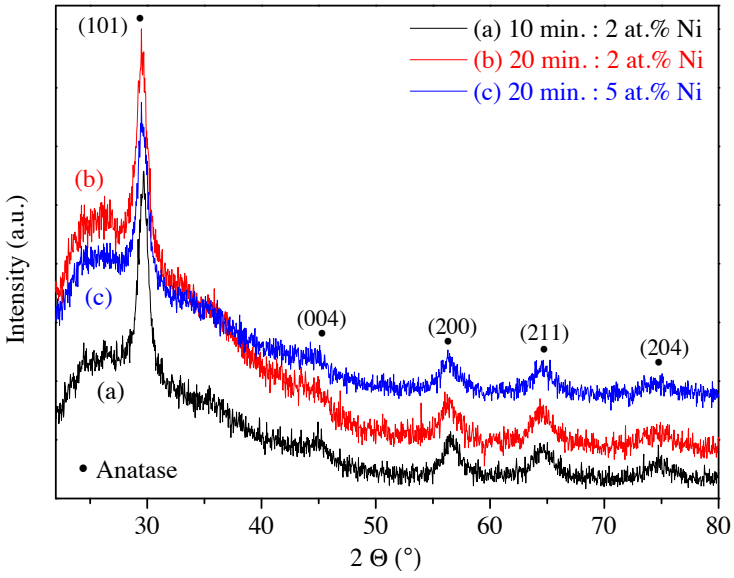

Figure 2. *Evolution of diffraction patterns of (5/5) SiO_2/(Ni:TiO_2) Bragg reflectors annealed at 550°C : (a) during10 min. and doped 2 at.% Ni:TiO_2, (b) during 20 min. and doped 2 at.% Ni:TiO_2, and (c) during 20 min. and doped 5 at.% Ni:TiO_2.*

Moreover, no other distinguished crystalline phase was detected, which indicates that Ni species were highly dispersed in TiO_2 nanoparticles [32]. Since Ti^{4+} and Ni^{2+} have similar ionic radius, the XRD data analysis showed that no significant lattice deformation occurred with increasing Ni content and annealing duration [33].

For samples doped with 2 at.% Ni, the full width at half maximum (β_{XRD}) values of main anatase peak (101) decreased from 1.40° and 1.14° when the annealing duration increases from 10 min. (Fig. 2(a)) to 20 min. (Fig. 2(b)) (see Table 1). By cons, for samples annealed during 20 min., the β_{XRD} increases from 1.14° to 1.18° as soon as the Ni content increases from 2 at.% Ni (Fig. 2(b)) to 5 at.% Ni (Fig. 2(c)) (Table 1). Accordingly, using β_{XRD} values of intense anatase peak (101), the crystallite size "D" of SiO_2/(Ni:TiO_2) Bragg reflectors can be calculated by Scherrer's formula [34]:

$$D = \frac{0.94 \times \lambda}{\beta_{XRD}.\cos\theta}$$

Where λ is the wavelength of the X-ray beam (λ_{Co}= 1.79026 Å), β is the full width at half maximum (β_{XRD}) of (hkl) diffraction peak and θ is the Bragg angle.

The full width at half maximum (β_{XRD}) and strain (ε) can be related according to the following equation [36]:

$$\varepsilon = \frac{\beta_{XRD} \times \cos\theta}{4}$$

The variation of strain with the Ni content, annealing duration and grain size is shown in Table 1. As we can observe, for 2 at.% Ni:TiO_2, a significant decrease in internal strain was caused by increasing the annealing duration from 10 to 20 minutes; which can be explained by the increase of the grain size from 11.76 to 14.45 nm. Conversely, for 20 minutes, the increase of the Ni content from 2 at.% to 5 at.% increases the internal strain. This can be related to the decrease of the grain size from 14.45 to 13.96 nm. In fact, this behavior is closely related to the inverse proportion between strain and grain size.

3.1.2. Raman spectroscopy

The Raman spectra in the range 95-900 cm^{-1} of SiO_2/(Ni:TiO_2) Bragg reflectors, developed on glass substrates, are shown in Fig. 4. For SiO_2/(2 at.% Ni:TiO_2) (Fig. 3(a)), annealed for 10 minutes, the spectra show symmetric vibration modes (A_{1g}+ $2B_{1g}$+$3E_g$) of

anatase phase identified at 144.9 cm^{-1} (E_g), 198.1 cm^{-1} (E_g), 396.6 cm^{-1} (B_{1g}), 515.9 cm^{-1} (A_{1g}+ B_{1g}) and 637.3 cm^{-1} (E_g) [37]. The intense band at ~ 144.9 cm^{-1} is due to O-Ti-O bending vibrations and it corresponds to anatase phase [38]. All the four peaks correspond to the Raman active phonon modes of tetragonal anatase phase of TiO_2 [39]. The observed band positions are in good agreement with the previous reports for anatase phase [40].

Compared to SiO_2/(2 at.% Ni:TiO_2) (Fig. 3(a)), annealed for 10 minutes, the Raman spectrum of SiO_2/(2 at.% Ni:TiO_2) (Fig. 4(b)), annealed for 20 minutes, shows a significant increase in all the bands which may be due to the growth of the grain size. As we can see, we note an intense band is situated at ~ 144.9 cm^{-1} and low intensity bands are situated around 199.9, 397.5, 518.3 and 639.8 cm^{-1}. By cons, for 20 minutes of annealing duration, increasing the Ni content from 2 at.% (Fig. 4(b)) to 5 at.% (Fig. 3(c)) diminishes all bands intensity that are located at ~ 144.9, 397.5, 520.8 and 637.3 cm^{-1}. It is worthy to notice that the elevation of Ni content leads to the disappearance of the band situated at ~ 199.9 cm^{-1}. Thus, the decrease in intensity and the disappearance of bands with Ni content may be attributed to the decrease of the grain size.

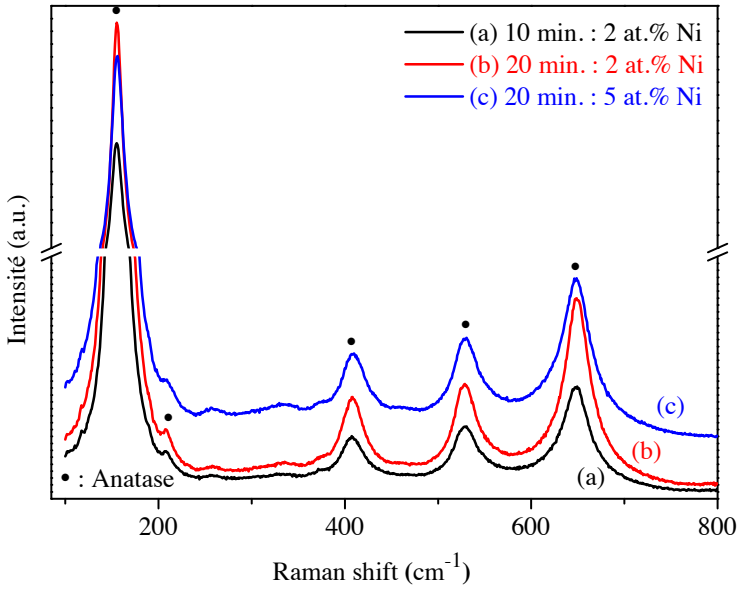

Figure 3. *Raman spectra of (5/5) SiO_2/(Ni:TiO_2) Bragg reflectors annealed at 550°C : (a) during10 min. and doped 2 at.% Ni:TiO_2, (b) during 20 min. and doped 2 at.% Ni:TiO_2, and (c) during 20 min. and doped 5 at.% Ni:TiO_2.*

As mentioned in Table 1, the increase of the annealing duration from 10 to 20 minutes (Fig. 4(a) and (b)) decreases the full width at half maximum (β_{Raman}) of the intense Raman band

from 19.41 to 16.57 cm^{-1}, while it increases from 16.57 to 17.35 cm^{-1} with the increase of the Ni content from 2 at.% to 5 at.% (Fig. 4(b) and (c)).

Table 1. *Variation of XRD, Raman and UV-Vis parameters for different Ni contents and annealing durations.*

Annealing duration (min.)		*10*	*20*	*20*
Ni content (at. %)		*2*	*2*	*5*
XRD	β_{XRD} (°)	*1.40*	*1.14*	*1.18*
	X_{cent} (°)	*29.65*	*29.65*	*29.65*
	D (nm)	*11.76*	*14.45*	*13.96*
	ε ($\times 10^{-2}$)	*33.83*	*27.55*	*28.18*
Raman	β_{Raman} (cm^{-1})	*19.41*	*16.57*	*17.35*
UV-Vis	*T%*	*2.26*	*1.46*	*3.39*
	w (nm)	*172.01*	*185.30*	*145.14*
	λ_{cent}(nm)	*500*	*562*	*494*

In light of the inverse relationship between the grain size and the full width at half maximum we noticed, on one hand, that the increase of the annealing duration decreases β_{Raman} and thus increases the gain size. On the other hand, we observed that increasing Ni content leads to increased β_{Raman} and then decreases the grain size. These results confirm the agreement between the X-ray diffraction and Raman spectroscopy.

4. Optical properties

4.1. UV-Vis-IR analysis

Fig. 4 displays diffused scattering UV-Vis-IR transmittance spectra of and SiO_2/(Ni:TiO_2) Bragg reflectors in the range 300-1500 nm. Fig.5 illustrates three regions characterized by sharp absorption bands below 440 nm, stop bands in the range 400-715 nm and wavy structures above 715 nm. The last, are due to interferences of waves that are not in Bragg condition. As we can see, for 2 at.% Ni:TiO_2, the center of the stop band red-shifts when the annealing duration increases from 10 min. (Fig. 4(a)) to 20 min. (Fig. 4(b)). In addition, the elevation of the last diminishes the transmission coefficient T% of the stop band, while the corresponding width broadens (see Table 1). Inversely, as the Ni content increases from 2 at.% (Fig. 4(b)) to 5 at.% (Fig. 5(d)), for 20 minutes of annealing duration, the center of the stop band blue-shifts, the transmission coefficient (T%) increases and the width of the stop band widens (see Table 1).

It is worthy to mention that the red-shift and the blue-shift of the stop band center can be correlated, respectively, with the increase and the decrease of the grain size.

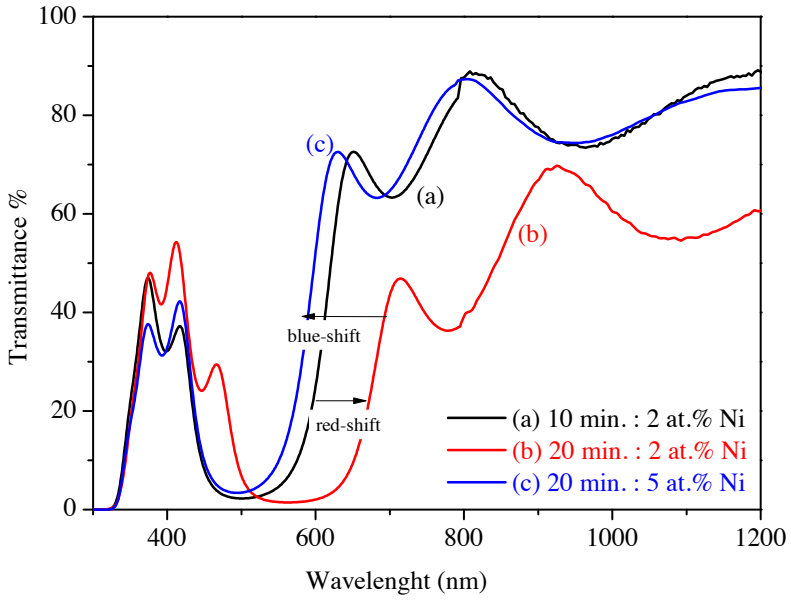

Figure 4. *UV-Vis-IR spectra of (5/5) SiO_2/(Ni:TiO_2) Bragg reflectors annealed at 550°C : (a) during10 min. and doped 2 at.% Ni:TiO_2, (b) during 20 min. and doped 2 at.% Ni:TiO_2, and (c) during 20 min. and doped 2 at.% Ni:TiO_2.*

4.2. Photoluminescence study

The recorded photoluminescence (PL) spectra were obtained by exciting the samples with the 313 nm radiation of Hg lamp. As we can see, for 2 at.% Ni:TiO_2, increasing the annealing duration from 10 minutes (Fig. 5 (a)) to 20 minutes (Fig. 5 (b)) increases the PL emission peak intensity and additional sharp emission peak appears around 867 nm. The increase of the PL intensity may be due to the increase of the recombination rate of electrons-holes and to the growth of the grain size.

Inversely, we notice here that the elevation of the Ni content from 2 at.% Ni (Fig. 5(b)) to 5 at.% Ni (Fig. 5(c)) decreases the PL intensity and causes a red-shift of the emission PL peaks. On one hand, the decrease in PL intensity with Ni content may be due to the introduction of new defect sites that can act as trapping level in the band-tail states [42]. On the other hand, the emission of PL red-shift could be regarded as the recombination of excited electrons and holes in the band gap [25,29]. It is worthy to note that the lowering of the PL intensity of SiO_2/(Ni doped TiO_2) Bragg reflectors could be assigned to the reduction of the recombination rate of the electrons–holes and to the decrease of the grain size [43].

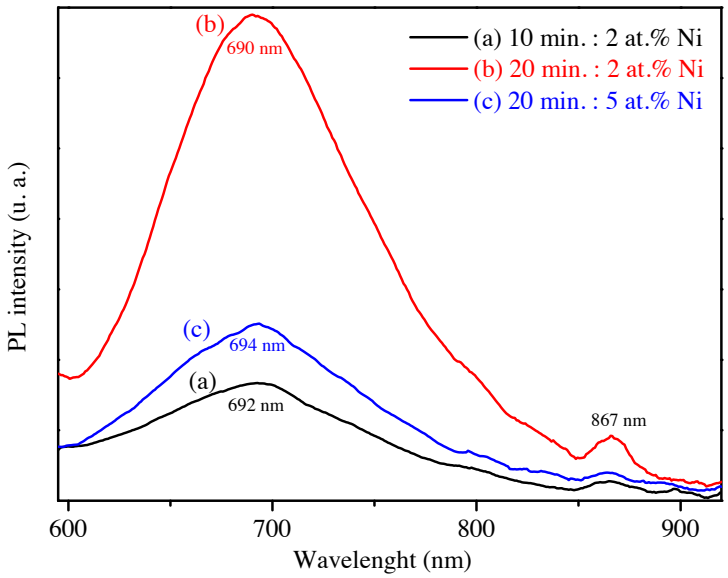

Figure 5. *Photolumiescence spectra of (5/5) SiO_2/(Ni:TiO_2) Bragg reflectors annealed at 550°C : (a) during10 min. and doped 2 at.% Ni:TiO_2, (b) during 20 min. and doped 2 at.% Ni:TiO_2 and (c) during 20 min. and doped 2 at.% Ni:TiO_2.*

5. Conclusion

In summary, the effects of Ni content and annealing duration on SiO_2/(Ni:TiO_2) Bragg reflectors, processed by the sol–gel method, have been investigated. The films crystallize in pure anatase phase whatever is the Ni content and the annealing duration. Compared with 2 at.% Ni, doping with 5 at.% Ni is not interesting because Bragg reflectors doped with this concentration tend to have a narrower stop band and a greater transmission coefficient (3.39%). By cons, raising annealing duration from 10 to 20 min, for doping with 2 at.% Ni, seems very interesting since the stop band broadens and the transmission coefficient decreases from 2.26% to 1.46%. In conclusion, doping TiO_2 with 2 at.% Ni and annealing during 20 minutes improves the structural and optical properties of SiO_2/TiO_2 Bragg reflectors, that can be used in solar cells and optical microcavities.

References

[1] W. W. Chow, K. D. Choquette, M. H. Crawford, K. L. Lear, G.R. Hadley, Int. J. Quantum Chem., 33 (1997) 1810.

[2] D. Weidermann, R. King, C. Fung, R. Jager, R. Michalzik, P. Schnitzer, M. Kicherer, K. J. Ebeling, IEEE J. Select. Topics Quantum Electron., 5 (1999) 503.

[3] S. Rabaste, J. Bellessa, A. Brioude, C. Bovier, J.C. Plenet, R. Brenier, O. Marty, J. Mugnier and J. Dumas, Thin Solid Films, 416 (2002) 242–247.

[4] M. Z. Shvarts, O. I. Chosta, I. V. Kochnev, V. M. Lantratov and V. M. Andreev, Solar Energy Materials & Solar Cells, 68 (2001) 105-122.

[5] A. Chiasera, R. Belli, S. N. B. Bhaktha, A. Chiappini, M. Ferrari, Y. Jestin, E. Moser, G. C. Righini and C. Tosello, Appl. Phys. Lett., 89 (2006) 171910/1.

[6] J. Kalkman, E. de Bres, A. Polman, Y. Jun, D.J. Norris, D. C. 't Hart, J. P. Hoogenboom and A. van Blaaderen, J. Appl. Phys., 95 (2004) 2297.

[7] H. Schniepp and V. Sandoghdar, Phys. Rev. Lett., 89 (2002) 257403-1/4.

[8] A. Chiappini, C. Armellini, A. Chiasera, M. Ferrari, Y. Jestin, M. Mattarelli, M. Montagna, E. Moser, G. Nunzi Conti, S. Pelli, G.C. Righini, M. Clara Gonc_alves and R. M. Almeida, J. Non-Cryst. Solids, 353 (2007) 674.

[9] K. Jiang, A. Zakutayev, J. Stower, M. D. Anderson, J. Tate, D. H. McIntyre, D. C. Johnson and D. A. Keszler, Solid State Sciences, 11 (2009) 1692–1699.

[10] L. Yang, T. Carmon, B. Min, S. M. Spillane and K. J. Vahala, Appl. Phys. Lett., 86 (2005) 091114-1/3.

[11] G. C. Righini, C. Armellini, A. Chiasera, Y. Jestin, M. Ferrari, A. Chiappini, M. Montagna, C. A. Duverger, P. Féron, S. Berneschi, M. Brenci, G. N. Conti, S. Pelli, C. Gonc_alves and R. M. Almeida, Glass Technol. Eur. J. Glass Sci. Technol. Part A, 48 (2007) 200.

[12] T. Sakaguchi, F. Koyama and K. Iga, Electron. Lett., 24(15) (1988) 928.

[13] D. Kundu, P. K. Biswas and D. Ganguli, Journal of Non-Crystal Solids, 110 (1989) 13.

[14] Q. Zhang, X. Li, J. Shen, G. Wu, J. Wang and L. Chen, Materials Letters ,45 (2000) 311.

[15] M. Grün, P. Miska, X. Devaux, H. Rinnert and M. Vergnat, Optical Materials, 33 (2011) 1248–1251.

[16] Y. G. Boucher, A. Chiasera, M. Ferrari and G. C. Righini, Optical Materials, 31 (2009) 1306–1309.

[17] R.M. Almeida and A.S. Rodrigues, Journal of Non-Crystalline Solids, 326&327 (2003) 405–409.

[18] J. Zhang, X. Wang, W. T. Zheng, X. G. Kong, Y. J. Sun and X. Wang, Materials Letters, 61 (2007) 1658–1661.

[19] S. Rabaste, J. Bellessa, C. Bonnand, J. C. Plenet and L. Spanhel, Eur. Phys. J. B, 42 (2004) 47–50.

[20] L. G. Devi, N. Kottam, S. G. Kumar and K. E. Rajashekhar, Cent. Eur. J. Chem., 8(1) (2010) 142–148.

[21] V. Kozhukharov, C. Trapalis, B. Samuneva and E. Kirilova, Journal Materials Science Letter, 11 (1992) 1206.

[22] P. K. Biswas, D. Kundu and D. Ganguli, Journal of Materials Science Letter, 6 (1987) 1481.

[23] R. M. Almeida and Z. Wang, Proceeding SPIE, 4655 (2002) 23-24.

[24] Y. Wang, Thin Solid Films, 349 (1999) 120-125.

[25] W. Choi, A. Termin, and M. R. Hoffmann, The J. of Phys. Chem., 98 (1994) 13669-13679.

[26] F. B. Li, X. Z. Li and M. F. Hou, Applied Catalysis *B:* Environmental, 48 (2004) 185-194.

[27] T. Umebayashi, Journal of Physics and Chemistry of Solids, 63 (2002) 1909-1920.

[28] M. Anpo, Journal of Catalysis, 216 (2003) 505-516.

[29] D. H. Kim, H. S. Park, S. J. Kim and K. S. Lee, Catalysis Letters, 100 (2005) 49-52.

[30] H. Sedrati, R. Bensaha, M. Brahimi, H. Dehdouh, H. Bensouyad, F. Abbas and B. Toubal, Materials Science : A, Indian Journal, 9(3) (2013) 113-118.

[31] R. Mechiakh, F. Meriche, R. Kremer, R. Bensaha, B. Boudine and A. Boudrioua, Optical Material, 30 (2007) 645.

[32] D. Zhang, J. Sol-Gel Sci. Technol. , 58 (2011) 312–318.

[33] T. Umebayashi, T. Yamaki, H. Itoh and K. Asai, J. PhysChem Solids, 63 (2002) 1909.

[34] W. Que, A. Uddin and X. Hu, J. Power Sources, 159 (2006) 353.

[35] S. D. Sharma, D. Singh, K. K. Saini, C. Kant, V. Sharma, S. C. Jain and C.P. Sharma, Appl. Catal. A: General. , 314 (2006) 40.

[36] B. D. Cullity, Elements of X ray Diffraction, Addisson, Wesley Pub (1978).

[37] T. Ohsaka, J. Phys. Soc. Jpn., 48 (1980) 1661.

[38] R. P. Antony, T. Mathews, A. Dasgupta, S. Dash, A. K. Tyagi and B. Raj, J. Solid State Chemistry, 184 (2011) 624-632.

[39] M. Z. Hu, P. Lai, M. S. Bhuiya, C. Tsouris, B. Gu, M. Paranthaman, J. Gabitto and L. Harrison, J. Mater. Sci. , 44 (2009)2820–2827.

[40] T. Ohsaka, F. Izumi and Y. Fujiki, J. Raman Spectrosc. , 7 (1978)321.

[41] N. R. Mathews, Erik R. Morales, M. A. Cortes-Jacome and J. A. Toledo Antonio, Solar Energy, 83 (2009) 1499–1508.

[42] T. Umebayashi, Journal of Physics and Chemistry of Solids, 63(10) (2002) 1909-1920.

[43] R. Ulrich, J. Opt. Soc. Am., 60 (1970) 1337–1350.